

Development of a Magneto Optical Trap for Rubidium

87

by

Huzifa Mohammed Ahamed Mohammed Elnour

*Thesis presented in partial fulfilment of the requirements for the degree
of Master of Science in Physics in the Faculty of Science at Stellenbosch*



University

Department of Physics,
University of Stellenbosch,
Private Bag X1, Matieland 7602, South Africa.

Supervisors:

Dr. Christine M. Steenkamp

Prof. Erich G. Rohwer

December 2013

Declaration

By submitting this thesis electronically, I declare that the entirety of the work contained therein is my own, original work, that I am the sole author thereof (save to the extent explicitly otherwise stated), that reproduction and publication thereof by Stellenbosch University will not infringe any third party rights and that I have not previously in its entirety or in part submitted it for obtaining any qualification.

Date: December 2013

Copyright © 2013 Stellenbosch University
All rights reserved.

Abstract

Development of a Magneto Optical Trap for Rubidium 87

H. Elnour

*Department of Physics,
University of Stellenbosch,
Private Bag X1, Matieland 7602, South Africa.*

Thesis: MSc Physics

December 2013

A Magneto Optical Trap (MOT) is a configuration formed by three orthogonal pairs of counter-propagating circularly polarized laser beams and a magnetic field gradient. A MOT is used to cool, capture and trap large numbers of atoms in vacuum at very low temperature in μK range. In this thesis the development of an experimental setup for realising a MOT of ^{87}Rb atoms is presented. The atomic structure of Rb and the theoretical background of laser cooling and magneto optical trapping was reviewed. The influence of rubidium background pressure in the vacuum system, the laser beam size and the power and frequency on the number of the trapped atoms were studied in literature. The trapping and repumping lasers were characterised experimentally. Six circularly polarised trapping beams with equal power were formed and properly aligned to intersect at the center of the trapping cell. Two optical setups were designed and exploited to investigate and optimise the trapping beam polarisation. The repumping laser beam was successfully aligned and colinearly combined into all the trapping beams. Three different experimental setups for saturated absorption spectroscopy were developed. Saturated absorption spectra showing the hyperfine structure of both ^{85}Rb and ^{87}Rb isotopes were measured and are discussed. Using two saturated absorption spectroscopy setups, the frequencies of both lasers were successfully locked to the trapping and repumping transitions of ^{87}Rb respectively. A rectangular trapping cell was designed and attached to the vacuum system. A pressure of about 10^{-7} mbar was achieved. The magnetic field coils were characterised and affixed on both sides of the cell in an anti-Helmholtz configuration. Setups for imaging and quantification of the ^{87}Rb atoms in the MOT were designed. Finally, the procedures for demonstrating a MOT are

presented. In conclusion, the current status of the project is reported, with recommendations for the future work.

Uittreksel

Ontwikkeling van 'n Magneto Optiese Val vir Rubidium 87

H. Elnour

*Departement Fisika,
Universiteit van Stellenbosch,
Privaatsak X1, Matieland 7602, Suid Afrika.*

Tesis: MSc Fisika

Desember 2013

'n Magneto optiese val (Magneto Optical Trap, MOT) is 'n konfigurasie wat gevorm word deur drie ortogonale laserbundelpare, wat elk uit twee sirkelvormig gepolariseerde bundels met teenoorgestelde voortplantingsrigtings bestaan, en 'n magneetveld gradient. 'n MOT word gebruik om 'n groot aantal atome af te koel, te vang en vas te hou in vakuum by 'n baie lae temperatuur in die μK bereik. In hierdie tesis word die ontwikkeling van 'n eksperimentele optelling vir die realisering van 'n MOT van ^{87}Rb atome voorgelê. Die atoomstruktuur van Rb en die teoretiese agtergrond van laser afkoeling en 'n magneto optiese val is hersien. Die invloed van die rubidium agtergronddruk in die vakuumstelsel, die grootte van die laserbundels en die laser drywing en frekwensie op die aantal gevangde atome is bestudeer uit die literatuur. Die MOT-laser en die optiese pomplaser is eksperimenteel gekarakteriseer. Ses sirkelvormig gepolariseerde MOT-laserbundels met gelyke drywings is gevorm en behoorlik belyn om in die middel van die MOT-sel te kruis. Twee optiese opstellings is ontwerp en gebruik om die polarisasie van die MOT-laserbundels te ondersoek en te optimeer. Die optiese pomplaserbundel is suksesvol belyn en ko-liniêr ekombineer met al die MOT-laserbundels. Drie verskillende eksperimentele opstellings vir versadigde absorpsie spektroskopie is ontwikkel. Versadigde absorpsie spektra wat die hiperfyn struktuur van beide die ^{85}Rb en ^{87}Rb isotope toon is gemeet en bespreek. Deur twee versadigde absorpsie spektroskopie opstellings te gebruik is die frekwensies van beide lasers suksesvol gestabiliseer op die MOT- en optiese pomp-oorgange van ^{87}Rb onderskeidelik. 'n Reghoekige MOT-sel is ontwerp en aangesluit by die vakuumstelsel. 'n Druk van ongeveer 10^{-7} mbar is bereik. Die magneetveld spoel is gekarakteriseer en weerskante van die sel gemonteer in 'n anti-Helmholtz konfigurasie. Ten einde word die prosedures vir die demonstrasie van 'n

MOT voorgelê. In die gevolgtrekking word daar verslag gedoen oor die status van die projek, met aanbevelings vir toekomstige werk.

Acknowledgements

I would like to express my sincere gratitude to the following people and organisations:

My supervisors Dr. Christine M. Steenkamp and Prof. Erich G. Rohwer for their supervision, guidance, support and advice.

Dr. Michael J. Morrissey a post-doc fellow at the University of Kwazulu Natal school of physics department quantum research group (QRG) for the technical assistance and suggestions within our MOT experiment setup.

Academic staff of Laser Research Institute at Stellenbosch University for the discussion and significant suggestions during our LRI meetings.

Technical staff of Laser Research Institute at Stellenbosch University Mr. E. Shields, Mr. J. Germishuizen, Mr. G. Louwrens and Mr. U. Deutschländer for their assistance in experimental work.

Mr. Ashworth and Mr. Botha from the physics department workshop for the assistance with chamber construction.

My wonderful parents Mohammed Elnour and Zainab Abuzaid, brothers, sisters and the whole family for continuously supporting and standing by me throughout my thesis.

Colleagues and friends, for their help and encouragement during my studies.

This material is based upon work supported financially in part by the National Research Foundation. Any opinion, findings and conclusions or recommendations expressed in this material are those of the author(s) and therefore the NRF does not accept any liability in regard thereto.

The CSIR National Laser center through the Rental Pool Programme provided financial support to this Project.

University of Stellenbosch, African Institute for Mathematical Sciences (AIMS), African Laser Center (ALC) for providing this opportunity and financial support for me to do my masters' thesis.

Dedications

To my parents, Zainab Abuzaid and Mohammed Elnour,

Thank you

Contents

Declaration	i
Abstract	ii
Uittreksel	iv
Acknowledgements	vi
Dedications	vii
Contents	viii
List of Figures	xi
List of Tables	xv
1 Introduction	1
1.1 Motivation	1
1.2 Aims	1
2 Literature Review	3
2.1 Atomic structure of rubidium	3
2.1.1 Fine structure	3
2.1.2 Hyperfine structure	4
2.1.3 Interaction with an external magnetic field	5
2.2 Laser cooling	7
2.2.1 Basic equation for the velocity dependent cooling force	12
2.3 Laser trapping of cold atoms	13
2.3.1 Basic equation for position dependent trapping force	15
2.4 Magneto optical trapping of ^{87}Rb	16
2.5 Characterisation of the MOT	17
2.5.1 Techniques for observation of the trapped atoms	17
2.5.2 Determination of the number of trapped atoms	17
2.5.3 Determination of the temperature of trapped atoms	19

2.5.4	Parameters influencing the numbers of trapped atoms in a MOT	20
3	Experimental setup	22
3.1	Overview	22
3.2	Lasers system	22
3.3	Saturated absorption spectroscopy setups	24
3.4	Experimental setup for the MOT	26
3.4.1	Vacuum system and rubidium source	26
3.4.2	Magnetic field coils for the trapping cell	29
3.4.3	Optical setup of MOT experiment	30
3.5	Test setups for optimisation of polarization of trapping beams	32
3.6	MOT Characterisation System	33
4	Results and Discussions	36
4.1	ECDL characteristics	36
4.2	Saturated absorption spectra	37
4.3	Polarization and power control of the trapping beams	46
4.3.1	Power control	46
4.3.2	Circular polarisation of trapping beams	51
4.4	Power and losses in optical setup	55
4.5	Result on the magnetic field gradient	57
4.6	Simulation of the cooling force	58
4.7	Simulation of the trapping force	60
4.8	Procedure to achieve magneto optical trapping	61
4.8.1	How to find the operating current of the dispenser	62
4.8.2	Status of the magneto optical trapping experiment	62
5	Conclusions and future work	64
5.1	Summary and Conclusions	64
5.2	Recommendations for future work	65
6	AppendixA	66
6.1	Derivation of the polarization of the trapping beams from the first principles	66
7	AppendixB	70
7.1	Operation of the Vacuum System	70
8	AppendixC	71
8.1	Jones Matrices of Polariser	71
9	AppendixD	73
10	AppendixE	74

List of References

82

List of Figures

2.1	^{87}Rb hyperfine structure of $5^2\text{S}_{1/2} - 5^2\text{P}_{3/2}$	6
2.2	The splitting of $5^2\text{S}_{1/2}$ $F = 1, 2$ levels of ^{87}Rb in the presence of a weak external magnetic field. The levels are the ground state levels for the D_2 transition	8
	(a) $F = 1$ magnetic sub-levels	8
	(b) $F = 2$ magnetic sub-levels	8
2.3	The splitting of ^{87}Rb $5^2\text{P}_{3/2}$ $F' = 0, 1, 2, 3$ levels. These levels are the upper states of the D_2 transition in the presence of a weak external magnetic field.	9
2.4	Illustration of the frequency change of the cooling transition $5^2\text{S}_{1/2}$ $F = 2 \rightarrow 5^2\text{P}_{3/2}$ $F' = 3$ between the magnetic sub-levels due to the Zeeman effect	10
2.5	Illustration of the photons' scattering rate frequency dependent (hence atomic velocity dependent) with the considering of the Doppler Effect	11
2.6	The schematic shows the orientations of the magnetic field lines result from the anti-Helmholtz coils	13
2.7	Magneto optical trapping of atoms in one-dimension achieved by Zeeman shift of the atomic energy levels and illuminating the atoms by opposite circular polarized counter-propagating laser beams.	15
2.8	Illustration of the trapping and hyperfine pumping transitions between the hyperfine levels in Rb ,which used for cooling and trapping	16
2.9	The cooling transition in ^{87}Rb atom, showing transitions excited by σ^- and σ^+ polarized lasers beams, for magnetic field in the $+z$ direction. Zeeman shift at 20 Gauss are indicated below.	18
3.1	Overview of the experimental MOT setup. Key: OI-optical isolator, BS-beam splitter, SAS-saturated absorption spectroscopy, PBS-polarising beam splitter, NPBS-non-polarising beam splitter, M-mirror, HWP-half-wave plate, QWP-quarter-wave plate.	23
3.2	Schematic of the experimental setups for saturated absorption spectroscopy of Rb. Key: NDF-neutral density filter, 50/50BS, other abbreviations as in Figure 3.1.	25
	(a) Simple SAS setup	25
	(b) PBS SAS setup	25
	(c) 50/50BS SAS setup	25

3.3	Illustration of the vacuum system setup, (a) Side view of the system, which shows the turbo and roughing pumps, the three valves, and the vacuum gauge, six-way cross, and the electrical feedthrough for the getter. (b) Top view which shows the ion pump, the trapping cell, and a window on the flange opposite to the cell.	28
	(a) Side view	28
	(b) Top view	28
3.4	Schematic of the cross section of the magnetic coils configuration, and the current flowing through them in the opposite direction. The cross sections of the coil windings are shaded. The figure is not drawn to the scale.	31
3.5	Schematic of the optical setup for the MOT experiment: the trapping and repump lasers beams, and their path through the optics on the table. Key: L-lens, other abbreviations as in the previous figures.	32
3.6	Schematic of the optical setup of the tests for optimisation of the circular polarisation states of the trapping beams.	34
	(a) Test setup 1	34
	(b) Test setup 2	34
3.7	Illustration of the setup for the measurement of the fluorescence from the trapped atoms.	35
4.1	Trapping laser turn on curve	36
4.2	Repumping Laser turn on curve	37
4.3	Doppler-broadened absorption spectrum of Rb atoms measured with only probe 1 beam unblocked	38
4.4	Horizontal axis calibration of Doppler broadened absorption spectrum of Rb. The relative frequencies of the ground levels are plotted against the pixel position of the peaks as read from the oscilloscope	38
4.5	Doppler-broadened absorption spectrum of Rb atoms with the hyperfine structure	39
4.6	The Doppler-free hyperfine structure of the ^{87}Rb line with $5^2\text{S}_{1/2}$ $F = 2$ as ground state. The structure was obtained by the all three different SAS setups as indicated below each graph.	41
	(a) Simple SAS setup	41
	(b) PBS SAS setup	41
	(c) 50/50BS SAS setup	41
4.7	The Doppler-free hyperfine structure of the ^{87}Rb line with $5^2\text{S}_{1/2}$ $F = 1$ as ground state. The structure was obtained by the all three SAS setups as indicated below each graph.	42
	(a) Simple SAS setup	42
	(b) PBS SAS setup	42
	(c) 50/50BS SAS setup	42
4.8	Calibration of the horizontal axis of the hyperfine structure of the $5^2\text{S}_{1/2}$ $F = 2$ line. The frequency shift of each level is plotted against the pixel positions of the peaks.	43

4.9	The Doppler-free hyperfine structure of the line of ^{85}Rb with $5^2\text{S}_{1/2}$ $F = 3$ as ground state. The structure was obtained by PBS SAS and 50/50BS SAS setups as indicated below each graph.	43
	(a) PBS SAS setup	43
	(b) 50/50BS SAS setup	43
4.10	Doppler-free hyperfine structure of $5^2\text{S}_{1/2}$ $F = 2$ of ^{85}Rb . The structure was obtained by the PBS SAS and 50/50BS SAS setups as indicated below each graph.	44
	(a) PBS SAS setup	44
	(b) 50/50BS SAS setup	44
4.11	Illustration of an atom moving in the plane with velocity $ \vec{v} $, and has equal velocity components along the direction of probe and pump beams $ \vec{v}_{\text{pump}} = \vec{v}_{\text{probe}} $	45
4.12	The fluorescence of the two probes and pump beams passing through the Rb vapor cell, when the laser frequency was locked at the cooling transition.	46
4.13	Optical setup of the circular polarisation for the MOT experiment	47
4.14	Illustration for measurement of angle	48
4.15	powers of the linearly horizontal and vertical polarized light varying the angle θ , which the fast axis of the HWP makes with horizontal axis.	49
4.16	Result of Test 1: The power of the reflected beam by the (PBS) power as a function of the angle of the slow axis of the QWP with respect to the horizontal axis.	52
4.17	Result of Test 2: The power of the reflected beam by the PBS2 as varying the slow axis angle of the QWP1 with respect to the horizontal axis.	54
4.18	Schematic illustration of a cooling and trapping experiment using two symmetric magnetic coils with oppositely directed currents and three pairs of counter-propagating laser beams illuminating the atom from all six directions. See Appendix 6 for the details	54
4.19	Power and losses in the optical setup of the trapping laser	56
4.20	Power and losses in the optical setup of the repumping laser	57
4.21	The magnetic field value between the coils for a current of 0.5 Am	58
4.22	Result in the magnetic field. It has been done by M. Morrissey using Radia Software.	59
4.23	Cooling force versus velocity of atom in one-dimension, choose + direction for v_a . F_- is for \vec{k} in - direction, F_+ is for \vec{k} in + direction. The solid line is the net force \vec{F}	60
	(a) $\Delta = -0.5\Gamma$	60
	(b) $\Delta = -\Gamma$	60
	(c) $\Delta = -1.5\Gamma$	60
	(d) $\Delta = -2\Gamma$	60
4.24	Trapping force versus the detuning of the frequency Δ_z due to Zeeman effect, of atom in one-dimension. F_- is for the coming from the positive z-direction, F_+ is for the beam coming from the negative z-direction. The solid line is the net force \vec{F}	61
	(a) $I_1 \neq I_2$	61
	(b) $I_1 = I_2$	61
4.25	Rubidium fluorescences from the trapping beams.	63

6.1	Illustration of the trapping by circular polarised light and the split of the J level of the excited state in the presence of an external magnetic field.	67
6.2	Illustration of the association of the angular momentum vectors with m_j values. This association is independent from the direction of the external magnetic field.	69
6.3	Illustration of the association of σ^- and σ^+ transitions with the cw and ccw circular polarised light.	69

List of Tables

2.1	Properties of ^{87}Rb D_2 ($5^2S_{1/2} \rightarrow 5^2P_{3/2}$) transition.	4
2.2	The magnetic dipole and the electrical quadrupole constants of the transition D_2 of the hyperfine structure of the ^{87}Rb . h is the Planck constant.	5
2.3	The energy shift of the hyperfine levels of the ground and excited state of the D_2 transition in ^{87}Rb	5
3.1	Trapping and repumping ECDLs specifications	24
3.2	Pressure range of the roughing, turbo-molecular, and ion vacuum pumps	27
3.3	Coils parameters	30
4.1	FWHM of the Doppler-broadened absorption spectrum of Rb peaks	39
4.2	The FWHM of the Doppler-broadened absorption spectral peaks of Rb atoms with hyperfine structure	39
4.3	The FWHM of peaks of the hyperfine structure of $5^2S_{1/2}$ $F = 2$ spectral line of ^{87}Rb	40
4.4	The FWHM of peaks of the hyperfine structure of the $5^2S_{1/2}$ $F = 1$ line of ^{87}Rb	40
4.5	The FWHM of peaks of the hyperfine structure of the $5^2S_{1/2}$ $F = 3$ line of ^{85}Rb	44
4.6	Fitting parameters and ϕ values for different ranges and fixed step size	50
4.7	Fitting parameters and ϕ values for different steps size and fixed range	50
4.8	The power of the trapping beams and their retroreflected beams	56
8.1	Jones transformation matrices of the half and quarter wave plates	71
9.1	The relative frequency of the Doppler-Broadened absorption spectrum peaks of Rb atoms	73
9.2	The energy shift of the hyperfine levels of the ground and excited levels of the D_2 transition in ^{85}Rb	73

Chapter 1

Introduction

1.1 Motivation

Atoms and molecules in a gas at room temperature have high velocity, for example the root mean squared (rms) velocity of the rubidium 87 atoms is 293 m/s. This thermal motion of the atoms and molecules broadens the spectral lines and thus affects the resolution of spectroscopic measurement [1].

Cooling of the gases reduces the rms velocity of these atoms and molecules, since the gas temperature is proportional to the rms velocity of its atoms or molecules. Using the traditional method of refrigerating, a sample with low temperature can be obtained, but the average velocity of the atoms still remains high, for example the rms velocity of the nitrogen molecules is 150 m/s at 77 K, the phase equilibrium temperature of nitrogen at atmospheric pressure, and the rms velocity of the helium atom is 90 m/s at 4 K, the phase equilibrium temperature of helium [1].

Magneto Optical Trapping is a cooling technique based on the radiation pressure force and magnetic field gradient. Using magneto optical trap (MOT), several samples of cooled and trapped atoms were achieved, such as a cloud cesium atoms with a density of 3×10^9 atoms/cm³ with a temperature below 500 μ K [2] and rubidium 87 atoms were trapped and cooled to 75 μ K [3].

A MOT has become a starting point for some other fundamental experiments in physics, such as building an experimental system to obtain Bose-Einstein condensate for some atoms in the quantum information field, study the interaction between the ultra-cold atoms or ions [4].

1.2 Aims

The aim of this project is to study the principles of laser cooling and magneto-optical trapping, study the technical requirements for a MOT setup for ⁸⁷Rb atoms using literature and calcu-

lations, study the influence of the trapping parameters on the number of trapped atoms using literature, complete the development of a MOT experiment, verify by measurements that the technical requirements are met, demonstrate magneto optical trapping of ^{87}Rb and investigate the influence of the trapping parameters experimentally.

Chapter 2

Literature Review

2.1 Atomic structure of rubidium

Rubidium is a metallic alkali element which exists in the first column of the periodic table. Its atomic number is 37 with the following ground state configuration $1s^2; 2s^2; 2p^6; 3s^2; 3p^6; 3d^{10}; 4s^2; 4p^6; 5s^1$. It has a single electron $5s^1$ in its outermost shell, which becomes $5p^1$ for the first excited state. Natural rubidium has two isotopes, the 72% abundant ^{85}Rb where the nuclear spin quantum number is $I=5/2$, and the 28% abundant ^{87}Rb where $I=3/2$ [5; 6].

^{87}Rb is desired for this study because its hyperfine structure lines are spaced more widely, can be resolved more easily in the saturated absorption spectroscopy experiment than that of ^{85}Rb .

The reasons for using of the rubidium atoms or alkali atoms in general in the laser cooling and trapping of the neutral atoms experiments, is that alkali atoms contain a closed-cycle transition which is important for cooling, it is easy to achieve an atomic vapour of the alkali atoms, and there are several available tunable diode lasers that the wavelength of their output beam is in the near infra-red region, which can excite the alkali atoms [7].

2.1.1 Fine structure

Fine structure is as a result of the coupling between the orbital angular momentum \mathbf{L} of the outer electron and its spin angular momentum \mathbf{S} . Then the total electron angular momentum \mathbf{J} formed by the coupling of these two momenta is given as:

$$\mathbf{J} = \mathbf{L} + \mathbf{S}. \quad (2.1.1)$$

The possible values of the quantum number of \mathbf{J} must lie in the range

$$|L - S| \leq J \leq |L + S| \quad (2.1.2)$$

where the magnitude of \mathbf{J} is $\hbar\sqrt{J(J+1)}$. For the ground state in Rb atom $L=0$ and $S=1/2$, thus $J=1/2$. For the first excited state $L=1$ and it follows that J has two values; $J=1/2$, and $J=3/2$. The orbital-spin interaction causes states with different J values to have different energies. For ^{87}Rb the D-lines are: D_1 line is ($5^2S_{1/2} \rightarrow 5^2P_{1/2}$) transition and D_2 line is ($5^2S_{1/2} \rightarrow 5^2P_{3/2}$) transition. These energy levels are labelled according to the Russell Saunders formula, which is: $n^{2S+1}L_J$, where n is the principle quantum number of the outer electron, for S , L and J are respectively spin, orbital, and total angular momentum quantum numbers, with $L=0 \rightarrow S$, $L=1 \rightarrow P$. Our focus is on the D_2 transition which is the cycling transition in laser cooling, therefore some of its optical properties are provided in Table 2.1.

Table 2.1: Properties of ^{87}Rb D_2 ($5^2S_{1/2} \rightarrow 5^2P_{3/2}$) transition.

Property	Symbol	Value	Unit	Source
Mass	m	$1.443\,160 \times 10^{-25}$	kg	[5; 8]
Cooling transition		$5^2S_{1/2} F=2 \rightarrow 5^2P_{3/2} F'=3$		
Repump transitions		$5^2S_{1/2} F=1 \rightarrow 5^2P_{3/2} F'=1$ $5^2S_{1/2} F=1 \rightarrow 5^2P_{3/2} F'=2$		
Frequency		$2\pi \times 384.230$	THz	[5]
Wavelength(Vacuum)	λ_v	780.241209686	nm	[5]
Transition Energy	E	1.589049462	eV	[5]
Natural linewidth	FWHM	$2\pi \times 6.0666(18)$	MHz	[5]
Saturation intensity	I_s	1.6	mW.cm^{-2}	[8]
Life time of the upper state	τ	27	ns	[8]

2.1.2 Hyperfine structure

Hyperfine structure is as a result of the coupling between the total nuclear angular momentum \mathbf{I} with \mathbf{J} . The total atomic angular momentum \mathbf{F} is given by:

$$\mathbf{F} = \mathbf{J} + \mathbf{I}.$$

For the same quantum numbers J and I there are several values of total angular momentum quantum number of the atom F . These values lie in the range:

$$|J - I| \leq F \leq |J + I|$$

For ^{87}Rb $I = 3/2$. In the ground state $J = 1/2$, and we have $F = 1$ or $F = 2$. For the $5^2P_{1/2}$ excited state $J = 1/2$ and $F = 1, 2$. For the $5^2P_{3/2}$ excited state $J = 3/2$, F can take the following values: 0, 1, 2, or 3 [9]. Hyperfine splitting causes states with different F values to have different energies. The hyperfine energy shifts are given by [5]:

$$\Delta E_{\text{hfs}} = \frac{1}{2}A_{\text{hfs}}K + B_{\text{hfs}} \frac{\frac{3}{2}K(K+1) - 2I(I+1)J(J+1)}{4I(2I-1)J(2J-1)} \quad (2.1.3)$$

where

$$K = F(F + 1) - I(I + 1) - J(J + 1)$$

A_{hfs} is the magnetic dipole constant and B_{hfs} is the electrical quadrupole constant. The magnetic dipole constant and the electrical quadrupole constant of the ^{87}Rb D_2 are given in Table 2.2

Table 2.2: The magnetic dipole and the electrical quadrupole constants of the transition D_2 of the hyperfine structure of the ^{87}Rb . h is the Planck constant.

The constant	Value	Unit	Source
Magnetic Dipole Constant $A_{5^2S_{1/2}}$	$h \times 3.417\ 341\ 305\ 452\ 145(45)$	GHz	[5]
Magnetic Dipole Constant $A_{5^2P_{1/2}}$	$h \times 407.24(77)$	MHz	[5]
Magnetic Dipole Constant $A_{5^2P_{3/2}}$	$h \times 84.7185(20)$	MHz	[5]
Electrical Quadrupole Constant $B_{5^2P_{3/2}}$	$h \times 12.4965(37)$	MHz	[5]

Using Equation 2.1.3 and the constants in Table 2.2. The energy shift for each hyperfine level of ^{87}Rb is calculated as shown in Table 2.3. Figure 2.1 shows the fine and hyperfine structures of ^{87}Rb for the ground and first excited states.

Table 2.3: The energy shift of the hyperfine levels of the ground and excited state of the D_2 transition in ^{87}Rb .

Fine level	Hyperfine level	Energy shift /MHz
$5^2S_{1/2}$	$F = 1$	-4271.676632
	$F = 2$	2563.005979
$5^2P_{3/2}$	$F' = 0$	-302.07375
	$F' = 1$	-229.85175
	$F' = 2$	-072.91125
	$F' = 3$	193.74075

2.1.3 Interaction with an external magnetic field

Applying an external magnetic field causes each of the hyperfine F energy levels to split into $2F+1$ sub-levels labelled as m_F . If the magnetic field is relatively weak, the splitting is known as Zeeman effect. The energy shift of each sub-level m_F due to the Zeeman effect is given as [5; 8]

$$E = m_F \mu_B B g_F. \quad (2.1.4)$$

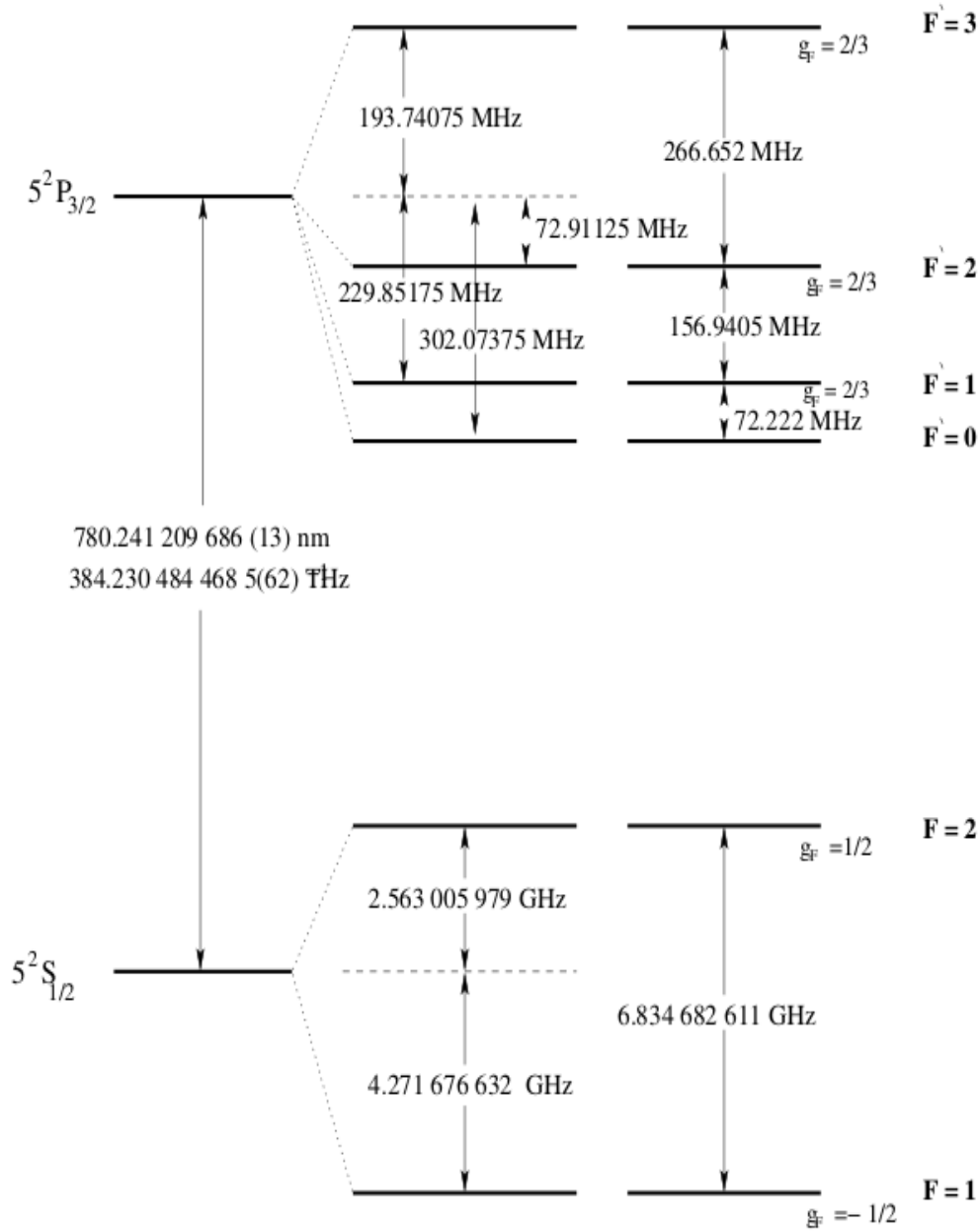


Figure 2.1: ^{87}Rb hyperfine structure of $5^2S_{1/2} - 5^2P_{3/2}$ D_2 transition.

E varies with the magnetic quantum number m_F which is in the range $-F < m_F < +F$. B is the magnetic field strength in Gauss, μ_B is the Bohr magneton and g_F is the Landé-factor. The value of g_F for the hyperfine levels is given as

$$g_F = g_J \cdot \frac{F(F+1) + J(J+1) - I(I+1)}{2F(F+1)} \quad (2.1.5)$$

where g_J is the fine structure g -factor and each fine structure level has the following form

$$g_J = 1 + \frac{J(J+1) + S(S+1) - L(L+1)}{2J(J+1)}. \quad (2.1.6)$$

For the D_2 transition of rubidium, $g_{F=1} = -\frac{1}{2}$ and $g_{F=2} = \frac{1}{2}$ for ground level, and $g_{F'=1} = \frac{2}{3}$, $g_{F'=2} = \frac{2}{3}$, and $g_{F'=3} = \frac{2}{3}$ for the excited level. Therefore we can find the corresponding shift in the frequencies of the hyperfine transitions due to Zeeman effect, which given for example by

$$\delta\nu = \frac{\mu_B}{h} B (g_{F'=3} m_{F'} - g_{F=2} m_F) \quad (2.1.7)$$

for the $5^2S_{1/2} F = 2 \rightarrow 5^2P_{3/2} F' = 3$ transition, where h is the Planck constant.

Figure 2.2 shows splitting of the hyperfine levels $5^2S_{1/2}$ of ^{87}Rb , in the external magnetic field. Figure 2.2(a) shows the splitting of $F = 1$ and 2.2(b) is the splitting of the $F = 2$. These levels are the ground state of the D_2 transition. Figure 2.3 shows the splitting of $5^2P_{3/2}$. These levels are from the upper state of the D_2 transition. The hyperfine levels are grouped according to the value of F in the weak magnetic field Zeeman regime. The splitting of the hyperfine levels in both the ground and the excited state are linearly proportional to the B-field in the Zeeman regime. At the ground state the energy shift between the two hyperfine levels $F = 1$ and $F = 2$ is about 6.8 GHz compared with the energy shift in their magnetic sub-levels which is of the order of several MHz. Hence two figures are provided for the Zeeman splitting of hyperfine levels of the ground state. The splitting of the hyperfine levels of the D_2 transition of ^{87}Rb as calculated and shown here is in agreement with that of Steck [5].

The weak magnetic field Zeeman regime will be applied in the magneto optical trapping experiment. In a strong external field the interaction with the field is described by the Paschen-Back effect and the levels are grouped according to m_j values, but this is not relevant to the current experiment.

Figure 2.4 shows the variation in the frequency of the cooling transitions $5^2S_{1/2} F = 2 \rightarrow 5^2P_{3/2} F' = 3$ in ^{87}Rb atom due to Zeeman effect. As can be seen from the graph the two groups σ^+ and σ^- of the transition. Their frequency shift is linearly proportional to the magnetic field but in the opposite directions.

2.2 Laser cooling

Laser cooling of atoms means the use of the force exerted by the photons of laser light to slow the atoms. The average speed of the atoms is proportional to the square root of the temperature of the gas [1]. The average speed of the rubidium atoms at room temperature is 293 m/s. This idea of light cooling atoms was first suggested by Hänsch and Schawlow in 1975 [10].

The basic mechanism causing the light force on atoms is the conservation of momentum and energy during the absorption and emission of light. Since the absorption or emission of photons leads to transfer of momentum between the photons and the atoms, the atom receives momentum impels which changes its velocity [11].

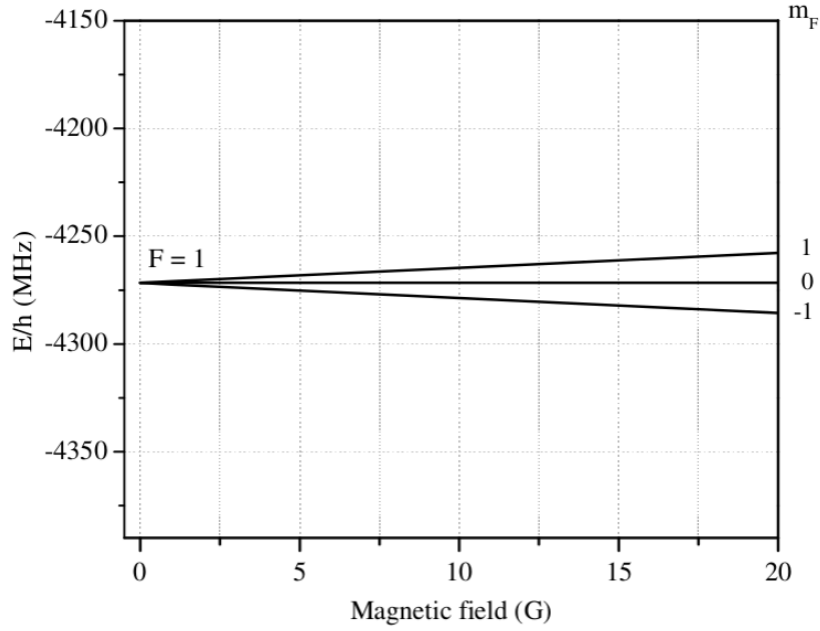
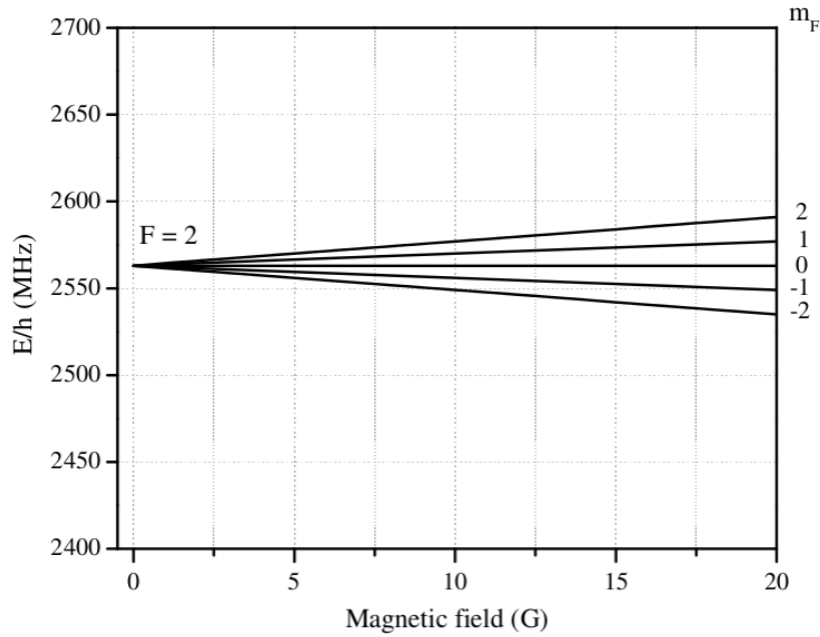

 (a) $F = 1$ magnetic sub-levels

 (b) $F = 2$ magnetic sub-levels

Figure 2.2: The splitting of $5^2S_{1/2}$ $F = 1, 2$ levels of ^{87}Rb in the presence of a weak external magnetic field. The levels are the ground state levels for the D_2 transition

The recoil velocity v_r of any atom is defined as the change in the atomic velocity due to the absorption or emission of a resonance photon, and is given as follow

$$v_r = \frac{\hbar k_1}{m}. \quad (2.2.1)$$

where m is the mass of the atom, and k_1 is the photon's wave-number. For the cooling transition of ^{87}Rb atom $k_1 = 2 \cdot \pi / 780 \text{ nm}^{-1}$, hence $v_r = 0.589 \text{ cm} \cdot \text{s}^{-1}$.

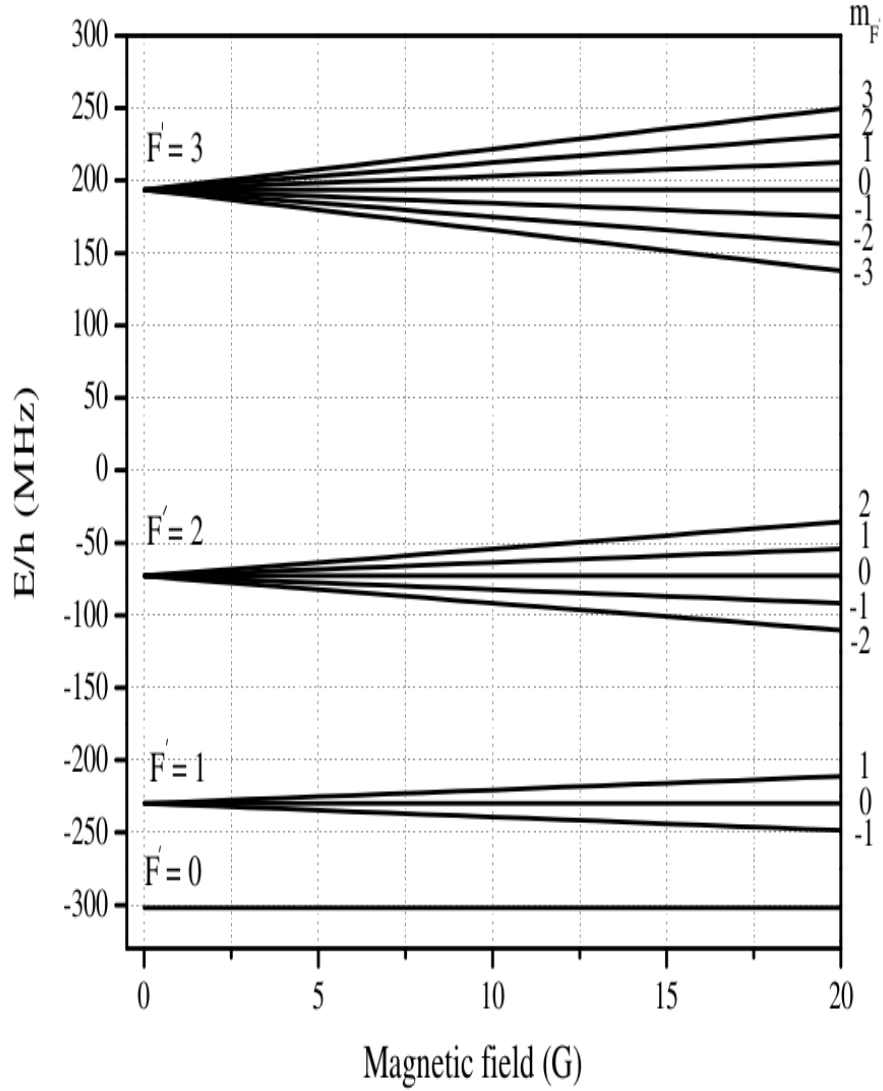


Figure 2.3: The splitting of $^{87}\text{Rb } 5^2\text{P}_{3/2}$ $F' = 0, 1, 2, 3$ levels. These levels are the upper states of the D_2 transition in the presence of a weak external magnetic field.

The kinetic energy when atom moves with the velocity $v = v_r$ is called recoil energy $\hbar\omega_r$ [5] which is expressed as follows:

$$\hbar\omega_r = \frac{\hbar^2 k_l^2}{2m}.$$

For the cooling transition of ^{87}Rb the recoil energy is, $\omega_r = 2\pi \times 3.781 \text{ kHz}$.

The temperature that associated with the photon recoil of an atom is called recoil temperature. This temperature is given by [8]:

$$T_r = \frac{\hbar^2 k_l^2}{m k_B}$$

where k_B is the Boltzmann constant. The recoil temperature of the ^{87}Rb is $T_r = 362.9866 \text{ nK}$.

This resulting light force can be divided into two types.

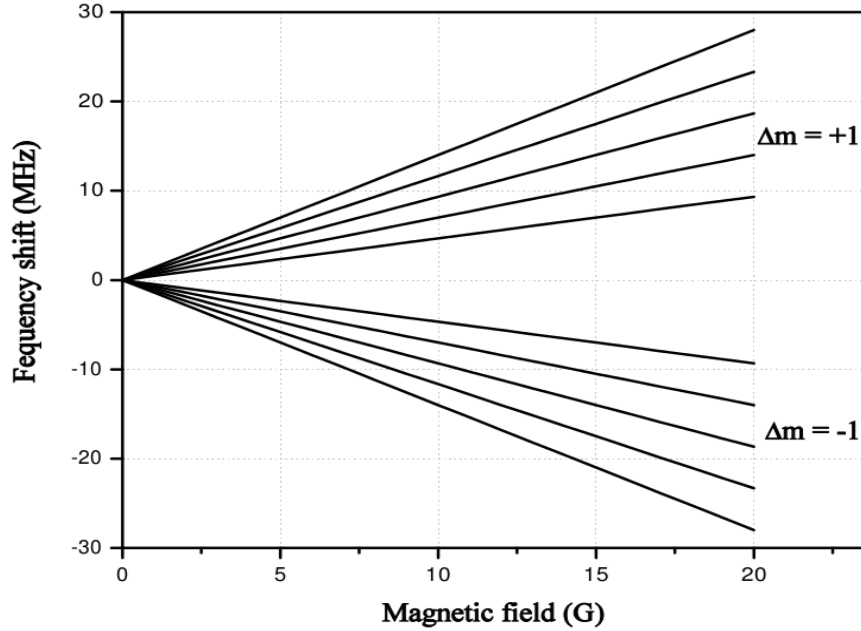


Figure 2.4: Illustration of the frequency change of the cooling transition $5^2S_{1/2} F = 2 \rightarrow 5^2P_{3/2} F' = 3$ between the magnetic sub-levels due to the Zeeman effect

The gradient or dipole force is a result of the cycles of the absorption followed by stimulated emission [12]. This occurs when light has higher intensity. This process does not cool the atoms because the momentum that is transferred to the atoms by stimulated emission process is in the opposite direction to what it was in the absorption [9].

The force that can be exploited to cool atoms is the scattering force. It is due to cycles of absorption and spontaneous emission of light [12]. If an atom is subjected to a large number of photons from laser, where photons have the same momentum, the atom will be excited and return to their ground states by spontaneous decay accompanied by emission of photons in random directions. Hence the average momentum of the spontaneously emitted photons is zero and so the force on the atoms is in the direction of propagation of the laser beam [9; 4]. The scattering force can be used to decelerate atoms in the sample [11].

Achieving atoms at lower temperature is possible, because the scattering rate of the photons is dependent on the atom's velocity due to the Doppler effect. Because of the role of the Doppler effect in the cooling process, it is referred to as Doppler cooling [12]. In Figure 2.5 there are two counter-propagating laser beams impinging on the atom from opposite directions. If the lasers' frequency ν_l is detuned slightly below the atomic resonance frequency ν_o , in the case of the stationary atom, the atom will experience two equal forces of the laser beams, from two opposite directions, therefore their effects cancel each other [13].

If the atom has a velocity v_a that is small compared with c the speed of light, the Doppler shift

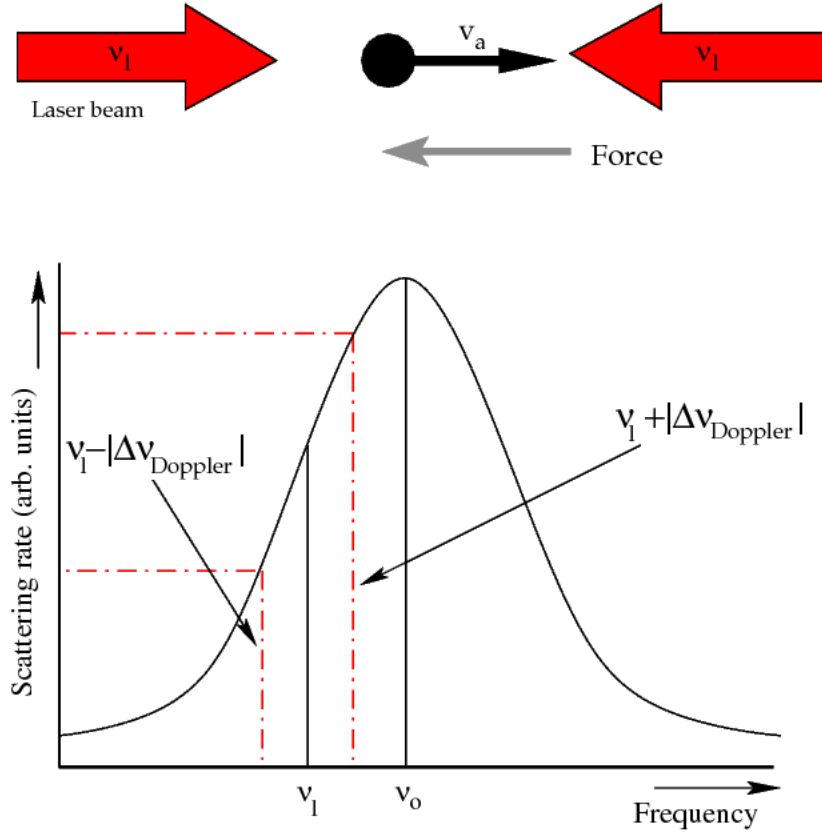


Figure 2.5: Illustration of the photons' scattering rate frequency dependent (hence atomic velocity dependent) with the considering of the Doppler Effect

$\Delta \nu_{\text{Doppler}}$ is given by the following expression:

$$\Delta \nu_{\text{Doppler}} = -\frac{1}{2\pi} \vec{k} \cdot \vec{v}_a$$

therefore

$$|\Delta \nu_{\text{Doppler}}| = \frac{1}{2\pi} \left(\frac{\omega_l}{c}\right) v_a = \frac{v_a}{c} \nu_l$$

where k is the wave vector of the laser light, v_a is the atom's velocity and ν_l is the laser frequency.

In the case of a moving atom, consider that an atom with a velocity component v_a along the two laser beams. The frequency of the photons travelling in the opposite direction are Doppler shifted closer the resonance frequency ν_o ($\vec{k}_l \cdot \vec{v}_a < 0$, ν_{Doppler} positive) and these photons will be scattered at higher rate than photons travelling in the same direction as the atom's velocity. Therefore the radiation force will always be in the opposite direction relative to the atom's velocity and it is velocity dependent according to the Doppler shift. This configuration of the laser beams was first demonstrated by Steven Chu and his colleagues at Stanford University and they named it an Optical Molasses [14]. If the atomic vapour is placed in the intersection region of three pairs of counter-propagation laser beams, then any movement of atoms can be slowed in all six directions.

Although atoms can be cooled down to low temperature due to the presence of cooling force, it is not possible to bring them to rest [15]. This is because of the heating process that arises from the random nature of absorption and spontaneous emission of photons [1]. The minimum temperature that can be reached in the optical molasses, is the temperature due to the balance between the cooling and heating processes. This temperature is called Doppler temperature. It is given by the following form [5]:

$$T_D = \frac{\hbar\Gamma}{2k_B}$$

where Γ is the natural decay rate of the excited states or Einstein coefficient A, k_B is the Boltzmann constant. $T_D = 1.456 \mu\text{K}$ for ^{87}Rb atoms.

2.2.1 Basic equation for the velocity dependent cooling force

The optical force on atoms which results from many cycles of absorption of photons followed by spontaneous fluorescence is called radiation pressure force or scattering force [9; 12; 16]. It is given by the following expression [9]:

$$\vec{F} = \frac{d\vec{p}}{dt} = \hbar\vec{k}\gamma_p \quad (2.2.2)$$

where $\hbar k$ is the momentum transfer from each photon, γ_p is the photon scattering rate. Assume that the profile of the absorption line is a Lorentzian profile. The scattering rate is given as [14]:

$$\gamma_p = \frac{\Gamma}{2} \left(\frac{I/I_s}{1 + I/I_s + [\frac{2\Delta}{\Gamma} + 2\frac{k\vec{v}_a}{\Gamma}]^2} \right) \quad (2.2.3)$$

where Γ is the natural decay rate of the excited state, $\Delta = \omega_o - \omega$ is the amount by which the frequency of the laser is detuned from the resonance (for red detuning it has positive value), $I_s = \frac{\pi\hbar c}{3\lambda^3\tau}$ is the saturation intensity, I is the laser intensity, τ is the excited state lifetime [9], \vec{k} is the wave vector and \vec{v}_a is the atom's velocity.

For a two level atom with ω_o resonance frequency moving with velocity \vec{v}_a and illuminated by a pair of counter-propagating laser beams of frequency ω detuned below ω_o , the damping cooling force on the atom is given by the sum of two opposing forces from the two beams. The forces both vary with the Doppler shift $k \cdot \vec{v}_a$. Using Equations 2.2.2 and 2.2.3 the net force on atom could be written as:

$$F(v) = \frac{\hbar k}{2} \Gamma \left[\frac{I/I_s}{1 + I/I_s + [\frac{2\Delta}{\Gamma} - 2\frac{k\vec{v}_a}{\Gamma}]^2} - \frac{I/I_s}{1 + I/I_s + [\frac{2\Delta}{\Gamma} + 2\frac{k\vec{v}_a}{\Gamma}]^2} \right] \quad (2.2.4)$$

The term with $\frac{2\Delta}{\Gamma} + 2\frac{k\vec{v}_a}{\Gamma}$ corresponds to k and v moving the same directions (red Doppler shift makes Δ bigger), $\frac{2\Delta}{\Gamma} - 2\frac{k\vec{v}_a}{\Gamma}$ corresponds to k and v moving the opposite directions (blue Doppler shift makes Δ smaller), respectively. Since k is constant, the cooling force in equation (2.2.4) is velocity dependent [9; 12; 16]. Calculation using the equation (2.2.4) presented in section 4.6.

2.3 Laser trapping of cold atoms

Optical molasses can only cool atoms, but it cannot confine them into a certain point in the space if there is no position dependent trapping force. In magneto optical cooling and trapping of atoms a position dependent force is achieved by:

- 1- Using circular polarized light for the optical molasses
- 2- Applying an inhomogeneous magnetic field to the beam intersection volume

Circular polarized light is very important in the magneto optical trapping in controlling the transitions of the electron in between the Zeeman sub-levels.

The magnetic field is generated using two symmetric magnetic coils with oppositely directed current, aligned in such way that the x-axis passes through their centers, and the separated distance between them is h . This configuration of the coils is known as anti-Helmholtz coils [17]. To have a linear increase of B with x near $B = 0$ point h must equal $2R$, where R is the radius of the coil. The orientations of the magnetic field lines generated by these coils are shown in Figure 2.6.

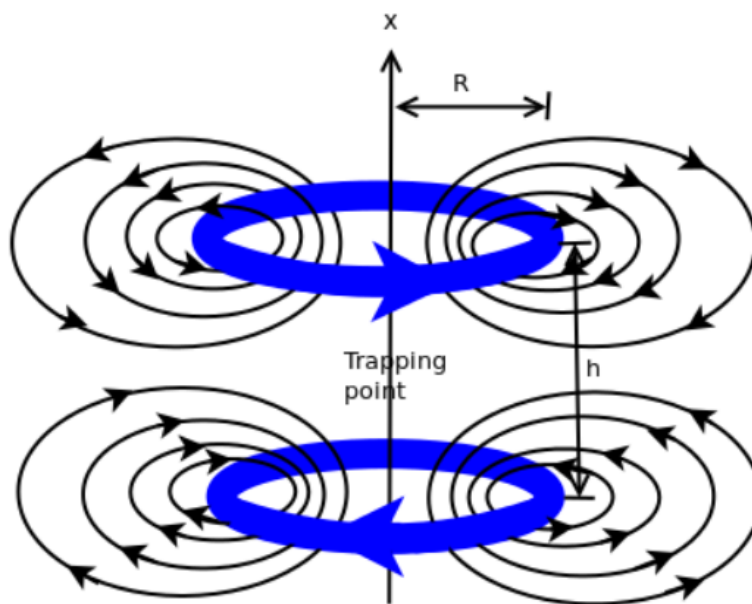


Figure 2.6: The schematic shows the orientations of the magnetic field lines result from the anti-Helmholtz coils

Consider two identical magnetic coils with diameter R . The coils are set in the anti-Helmholtz configuration with separation distance $h = 2R$ [7], as shown in Figure 2.6. When the coils have

thickness in both radial and x-axis directions, the magnetic field value along the x-axis at any point between the coils is given by the following expression:

$$B(x) = \frac{\mu_0 n I R^2}{2\left(\left(\frac{h}{2} - x\right)^2 + R^2\right)^{\frac{3}{2}}} - \frac{\mu_0 n I R^2}{2\left(\left(\frac{h}{2} + x\right)^2 + R^2\right)^{\frac{3}{2}}} \quad (2.3.1)$$

B is the magnetic field in Tesla.

$\mu_0 = 1.257 \times 10^{-6} \text{N}\cdot\text{A}^{-2}$ or $\text{H}\cdot\text{m}^{-1}$, the permeability of the space.

n is the number of turns in the coils, per unit length.

R is the radius of the coils.

I is the current flows in the coils.

h is the distance between the coils.

x is the distance between one of the coils and the point in which the magnetic field is calculated. This equation is used in section 4.5 to calculate the magnetic field gradient.

Once the magnetic field has been applied, the atomic energy levels will split according to the Zeeman effect. The B field magnitude and direction regulate the rate at which the atoms scatter photons from the circular polarised laser beams. Since \vec{B} varies with position, the radiative force becomes position dependent. The atoms will be pushed to the point where $\vec{B} = 0$. [11].

This can be explained further by considering a simple case of cooling and trapping of atoms in one-dimension as illustrated in Figure 2.7. A two level atom with $J = 0$ in the ground state and $J = 1$ in the upper state is considered, where J is the total angular momentum quantum number. The derivation of this figure from the first principles is shown in Appendix 6

As shown in Figure 2.7 the σ^+ polarized laser beam comes from the left hand-side. According to the momentum conservation law, this beam can only excite a transition if the change in the magnetic spin quantum number $\Delta m = +1$, while the σ^- polarized laser beam from the right can excite a transition when $\Delta m = -1$ [17]. The magnetic field B is zero at the (0) point in the origin of z axis and increasing the linearly in the opposite directions along the positive and negative z axis respectively. If we consider that an atom is to be at position to the right of the origin, the magnetic field will perturb the energy levels of it. Since $B > 0$ (meaning that B is in the positive z-direction) the transition with $\Delta m = +1$ will be shifted to a higher frequency, while transition with $\Delta m = -1$ will be shifted below the field-free resonance frequency of the atom. Since both of the laser beams' frequencies are detuned below the atomic resonance frequency, the probability of exciting the transition with $\Delta m = -1$ is higher than if $\Delta m = +1$, thus the scattering rate from the σ^- light at this point is higher than from the σ^+ light beam. This leads to the atom being pushed by the beam from the right toward the origin. On the left of the origin the opposite of this process will occur and the atom will be pushed toward the origin from this side also. The case of the magnetic field in the z-direction is analysed in detail in Appendix 6.

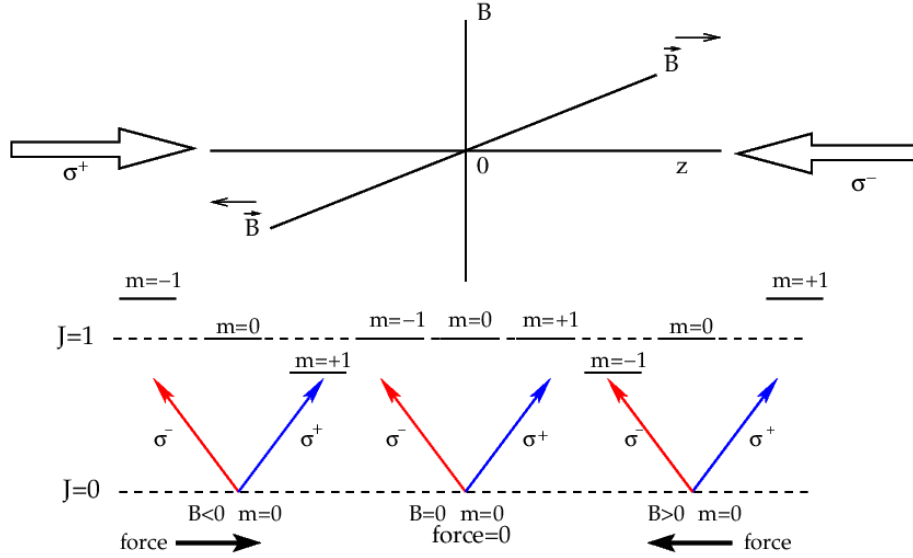


Figure 2.7: Magneto optical trapping of atoms in one-dimension achieved by Zeeman shift of the atomic energy levels and illuminating the atoms by opposite circular polarized counter-propagating laser beams.

The configuration of the magnetic field and the polarized laser beams is called Magneto Optical Trap. The process can be performed experimentally in three dimensions using two symmetric magnetic coils with oppositely directed currents to generate the magnetic field and irradiate the atom from all six directions by circular polarized light [11] as shown in Figure 4.18. The relation between σ^+ / σ^- and clockwise/counter clockwise with the given current direction is derived in Appendix 6.

2.3.1 Basic equation for position dependent trapping force

In a MOT atoms are trapped by the trapping force that depends on the position of the atoms. The force described by equation (2.2.3) is the cooling force only. We have considered only the shift in the frequency due to Doppler effect. But when we consider the shift in the frequency due to Zeeman effect equation 2.2.3 can be written as [18]

$$F(v, z) = \frac{\hbar k}{2} \Gamma \left[\frac{\frac{I_1}{I_s}}{1 + \frac{I_1}{I_s} + \left[\frac{2}{\Gamma} (\Delta + \Delta_z - kv_a) \right]^2} - \frac{\frac{I_2}{I_s}}{1 + \frac{I_2}{I_s} + \left[\frac{2}{\Gamma} (\Delta + \Delta_z + kv_a) \right]^2} \right], \quad (2.3.2)$$

This equation describes the cooling and trapping force as velocity and position dependent. Where Δ_z is the shift in the frequency due to Zeeman effect, and the subscript z is the position of the atoms along the z -axis. I_1 and I_2 are the power of the two counter-propagating trapping beams. This shift depends on magnetic field gradient, which in turn depends on z as illustrated in Figure 4.21. The other parameters are as described previously in equation (2.2.3). This trapping force always brings atoms toward the trapping center. Calculation using the equation (2.3.2) presented in section 4.7.

2.4 Magneto optical trapping of ^{87}Rb

Now we will consider the ^{87}Rb isotope, which has $5S^1$ single electron in the outermost shell. For the first excited state this electron becomes $5P^1$. The D₂ line is the $5^2S_{1/2} F = 2 \rightarrow 5^2P_{3/2} F' = 3$ transition which is the cycling transition, because the excited electrons at $F' = 3$ excited state can only decay to $F = 2$ ground state according to the selection rules of the electronic transitions $\Delta F = 0, \pm 1$. The cycling transition is used for cooling and trapping, which is illustrated in Figure 2.8. Trapping of ^{87}Rb is performed using a laser with its frequency detuned to be below the lowest Zeeman shifted component of $5^2S_{1/2} F = 2 \rightarrow 5^2P_{3/2} F' = 3$ transition frequency at approximately 780 nm.

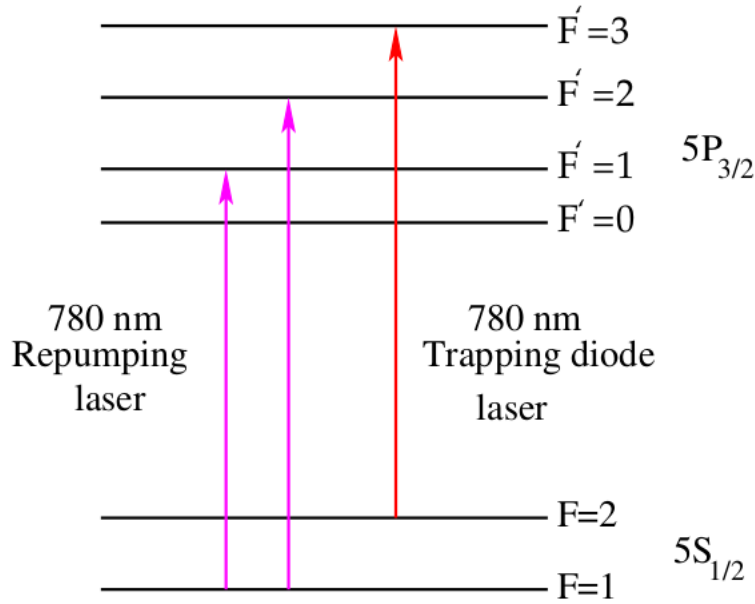


Figure 2.8: Illustration of the trapping and hyperfine pumping transitions between the hyperfine levels in Rb, which used for cooling and trapping

Figure 2.9 shows the Zeeman splitting of the magnetic sub-levels of the $5^2S_{1/2} F = 2$ and $5^2P_{3/2} F' = 3$ levels. Each one of $F = 2$ and $F' = 3$ levels has $2F+1$ magnetic sub-levels for the magnetic field in the $+z$ direction. The electronic transition between the magnetic sub-levels also follows the selection rules $\Delta m_f = 0, \pm 1$. In the laser cooling and trapping we consider the transitions $\Delta m_f = +1$ for the σ^+ transition, and $\Delta m_f = -1$ for the σ^- transition. Where $\Delta m_f = m_{f'} - m_f$ with $m_{f'}$ and m_f as the magnetic quantum numbers of the magnetic sub-levels of the $F' = 3$ excited level, and $F = 2$ ground level, respectively. In Figure 2.9 all the possible σ^+ and σ^- transitions are shown. As one can see there the σ^+ transitions can have higher resonance frequencies, than the σ^- transitions. This depends on the external magnetic field orientation. The hyperfine Landé factors g_F of the excited and ground level are not the same, hence the separation energy between the magnetic sub-levels of the excited state is different from the magnetic sub-levels of

the ground state. Splitting between σ^- and σ^+ transitions is 37.323 MHz at 20 Gauss. And the splitting between every two neighbouring transitions of σ^- (or σ^+ or π) is 4.67 MHz at 20 Gauss. These values were obtained by calculating the difference in the frequency shift between the magnetic sub-levels of the $F' = 3$ excited level and $F = 2$ ground level. The frequency shift was calculated using the equation (2.1.4). The π transitions group occurs when $\Delta m_f = m_{f'} - m_f = 0$, but these are not relevant in our experiment.

One out of a thousand excited ^{87}Rb atoms at $5P_{3/2}$ $F' = 3$ level will decay back to the $5s_{1/2}$ $F = 1$ ground state instead of the $5S_{1/2}$ $F = 2$ [11]. The trapping laser cannot excite atoms out of this $5S_{1/2}$ $F = 1$ state. If we left the atoms in this ground state they are not cooled or trapped any longer and it will reduce the number of the atoms which are trapped. Therefore it is necessary to use another laser called the hyperfine repumping laser operating on the frequency of the $5S_{1/2}$ $F = 1 \rightarrow 5P_{3/2}$ $F' = 1$ or, $5P_{3/2}$ $F' = 2$ transitions. From the $5P_{3/2}$ $F' = 1$ or $5P_{3/2}$ $F' = 2$ states the atoms can decay back to the $5S_{1/2}$ $F=2$ ground state and interact again with the trapping laser beam in the main process [17]. Figure 2.8 shows both of the possible transitions.

2.5 Characterisation of the MOT

2.5.1 Techniques for observation of the trapped atoms

During the trapping process, trapped atoms continuously scatter photons from the trapping beam so that the trapped atoms will appear as a very bright cloud in the center of trapping cell, compared to the fluorescence from the trapping beams. Because of the poor response of the eye to 780 nm, trapped atoms cannot be seen by eye, unless the room is quite dark. However using an infrared sensitive camera and monitor, trapped atoms can be observed [11]. This technique is used to show the image of the trapped atoms.

2.5.2 Determination of the number of trapped atoms

A photodiode with current-to-voltage amplifier can be used to detect the 780 nm fluorescence from the trapped atoms. The photodiode current is directly proportional to the number of trapped atoms.

The fluorescence by trapped atoms in the center of the cell as detected by a photodiode can also be used to determine the number of trapped atoms in MOT.

Although the fluorescence is enough to be detected by using a photodiode, it can also be obscured by the fluorescence from the background Rb vapour or by scattered light from the surface of the cell [11]. Over a large range of pressures the fluorescence from the rubidium background is very small compared with that from trapped atoms. The scattered light from the surface of the

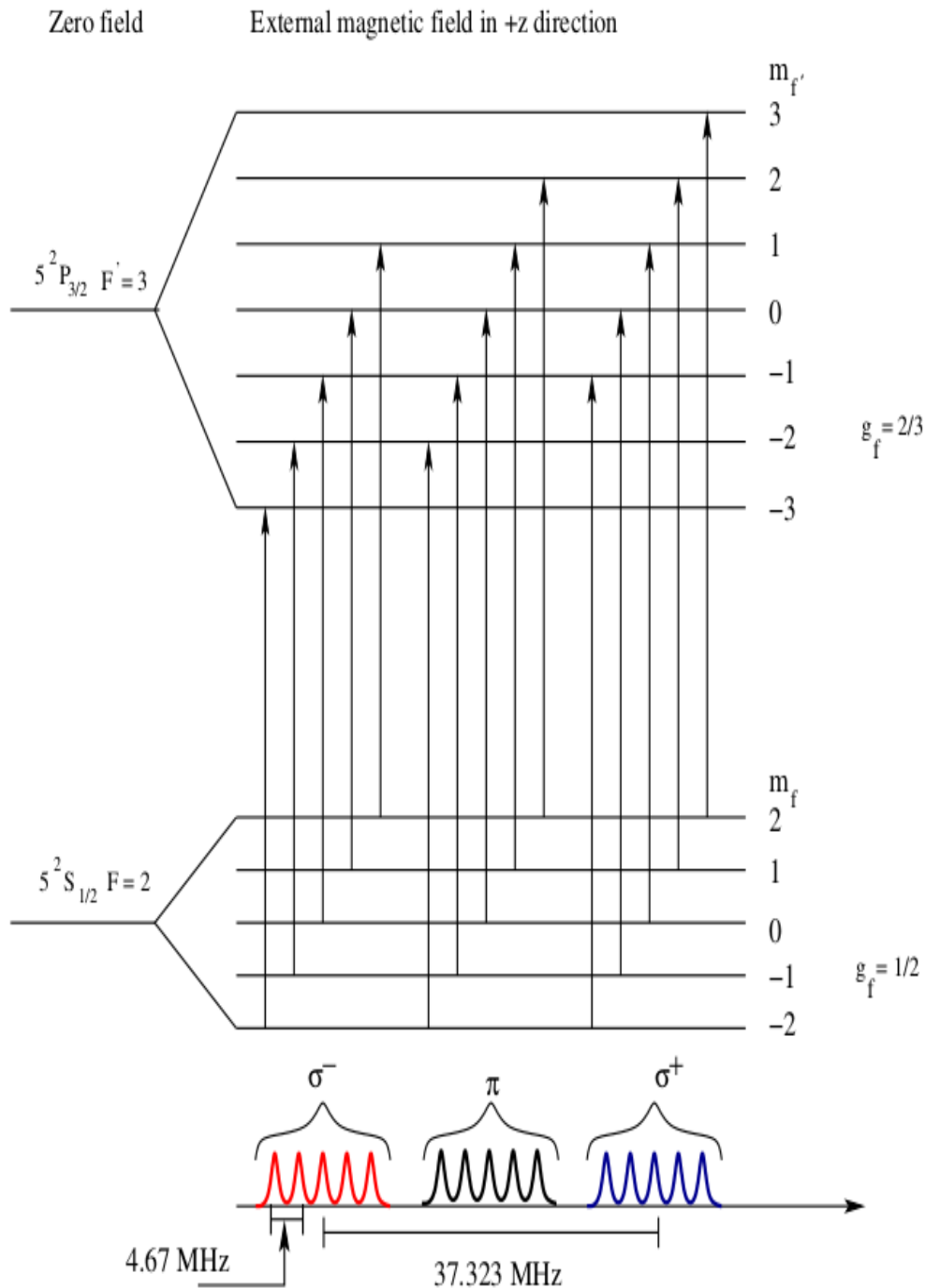


Figure 2.9: The cooling transition in ^{87}Rb atom, showing transitions excited by σ^- and σ^+ polarized lasers beams, for magnetic field in the +z direction. Zeeman shift at 20 Gauss are indicated below.

trapping cell is significant under all conditions [11]. This is because it can hit the photodiode [19], hence care must be taken in order to reduce its effect. This can be done by selecting a convenient position close to the cell to place the photodiode and the collection lens. Then consider the line of the sight from the collection lens through glass wall of the trapping cell to

the center of the MOT fluorescence (cloud) and onto the far glass wall of the cell. The line of the sight should not include any section of the glass wall that is illuminated by the trapping beams. Finally, the all unwanted scattered light can be blocked out by shielding the photodiode with a tube of black paper so that only light transmitted by the collection lens reaches it [19].

Getting some light scattered is unavoidable. To make an accurate measurement of the number of trapped atoms one must separate the fluorescences of the trapped atoms from the scattered light and the fluorescences of the background rubidium vapour. This measurement can be done by comparing the photodiode's signal when the magnetic field is on and off, or reversing the magnetic field by reversing the current that flows through the MOT magnetic coils. To measure the background scattering light the two lasers must be on, but the atoms must not be trapped. This is done by switching only the magnetic field off. But usually the background signal is very small compared with the signal from the trapped atoms [11].

Once one is able to determine the photo-current due to the trapped atoms, the number of the trapped atoms in MOT is given by the following expression [19]:

$$N = \frac{4\pi I_c}{\sigma \rho \varepsilon_p \gamma_p (0.96)^k} \quad (2.5.1)$$

where: I_c is the photodiode current due to the trapped atoms,

σ is the solid angle subtended by the collection lens,

ρ is the responsivity which refers to the current produced for a given power on the photodiode. in Ampere·Watt⁻¹,

ε_p is the energy of a photon in J,

k is the number of uncoated glass surfaces between the trapped atoms and the detector,

γ_p is the photon scattering rate in photons·atoms⁻¹·sec⁻¹, and is given by the following formula [11; 19]:

$$\gamma_p = \frac{\Gamma}{2} \frac{I/I_s}{1 + I/I_s + 4[\frac{\Delta}{\Gamma}]^2} \quad (2.5.2)$$

where I is the intensity of the six trapping beams impinging on the atoms. I_s is the saturation intensity, which is 4.1 mW/cm² for randomly polarized light for Rb. When the laser intensity equal to the saturation intensity, the excited atoms are equally likely to decay by stimulated emission or spontaneous emission [20]. Using the I_s appropriate for random polarization gives the most accurate number of trapped atoms in MOT according to H.J. Lewandowski group [19]. Δ is the detuning from the resonance. Γ is the natural linewidth of the transition and is equal to 6 MHz for Rb. In our setup $I \approx 90$ mW/cm². Hence γ_p is approximately 2.4×10^6 photons·atoms⁻¹·sec⁻¹ at $\Delta = \Gamma$.

2.5.3 Determination of the temperature of trapped atoms

The temperature of a cold atomic sample is an important parameter for characterisation of the MOT. Several methods are used to determine it. They include time-of-flight (TOF) and

release and recapture techniques (R&R). TOF is the one used in most laboratories [21] and is based on the spatial observation of the expansion of the atomic cloud after being released from the trapping forces as a function of time [22]. Through the transient absorption technique, the average velocity of the expansion of the atomic cloud will be determined. This velocity is directly related to the temperature.

2.5.4 Parameters influencing the numbers of trapped atoms in a MOT

The equation that governs the number of atoms in the trap can be written as [23]:

$$\frac{dN}{dt} = R - \beta N \quad (2.5.3)$$

where N is the number of the trapped atoms, R is the rate at which the atoms are captured from the background gas, and β is the loss rate due to collision. By assuming that $N(t=0)=0$, the solution of the equation (2.5.3) is given as

$$N(t) = N_{ss}(1 - e^{-t/\tau}) \quad (2.5.4)$$

This solution shows that the number of atoms in the trap N will grow exponentially just as a capacitor charging function. Where $N_{ss} = \frac{R}{\beta}$ is the steady-state number of the trapped atoms, and $\tau = 1/\beta$ is the time constant for the trap to fill its steady state defined by N_{ss} from the background vapour density. It is also the average time of an atom to remain in the trap before it is knocked out by collisions. It is also known as the inverse of the loss rate β [11]. Loss of the atoms from the trap can be due to two body intratrap collision or due to collisions with the hot background gas [24]. The intratrap collision is usually not important, but the collision due to the hot (room temperature) background gas is important and it is the dominance factor of the loss rate because these hot background molecules and atoms (Rb and contaminants) have more than enough energy to knock atoms out of the trap [11].

The loss rate $1/\tau$ due to collision with hot Rb and non-Rb atoms can be expressed in terms of the collisional cross sections (σ_{Rb} and σ_{non}), densities of the Rb and non-Rb component (n_{Rb} and n_{non}) as well as their average velocities (v_{Rb} and v_{non}) [11]:

$$\beta = \frac{1}{\tau} = n_{Rb}\sigma_{Rb}v_{Rb} + n_{non}\sigma_{non}v_{non} \quad (2.5.5)$$

The first part of the above equation in the the right hand side describes the loss rate due to collisions between Rb atoms, while the second term is for the collisions between the non-Rb atoms.

The steady-state number N_{ss} of the trapped atoms is defined as the number at which the loss rate and capture rates are equal. The capture rate is defined by the number of atoms entering the trap volume (as defined by the overlap of the trapping laser beams) with speed less than v_{max} [11], the maximum velocity an atom can have and be captured [25]. It is determined entirely

by the Doppler slowing which provides the damping [11]. R is proportional to the Rb density, $(v_{\max})^4$, and the surface of the cross sectional area A of the trap volume. When the background vapour is predominately Rb, the loss and capture rates are both proportional to Rb pressure, hence we can write N_{ss} in the following form [24; 25]:

$$N_{\text{ss}} = \left(\frac{0.1A}{\sigma_{\text{Rb}}} \right) \left(\frac{v_{\max}}{v_{\text{avg}}} \right)^4 \quad (2.5.6)$$

where $v_{\text{avg}} = \left(\frac{3k_{\text{B}}T}{m} \right)^{1/2} = 239 \text{ m/s}$ is the average velocity of the Rb atoms in the vapour at 298 K. If the loss due to collision with non-Rb background gas is significant then equation (2.5.5) must be multiplied by the following factor [11]:

$$\left(\frac{n_{\text{Rb}}\sigma_{\text{Rb}}v_{\text{avg}}}{n_{\text{Rb}}\sigma_{\text{Rb}}v_{\text{avg}} + n_{\text{non}}\sigma_{\text{non}}v_{\text{non}}} \right). \quad (2.5.7)$$

Finally when the collision with non-Rb background gas is the dominance of the loss rate in this case the number of atoms in the trap is proportional to the ratio of Rb pressure to the non-Rb pressure and τ will be independent of the Rb pressure [11].

From all the three cases above $N_{\text{ss}} \propto A(v_{(\max)}^2)$. This makes the number of trapped atoms very sensitive to the beam size, power and frequency. The beam size determines the A directly. The beam size, power and frequency influence the Doppler cooling, and therefore v_{\max} .

The number of trapped atoms is more sensitive to parameters that affect the cooling force than the parameters that affect the trapping force. Cooling force entirely depends on laser frequency which must be red shifted from the resonance frequency of the atom in order to achieve cold trapped atoms. While the trapping force is based on the magnetic field gradient. The change in the magnetic field gradient will obviously lead to a change in the number of trapped atoms. This is because at zero magnetic field gradient, we cannot achieve Zeeman splitting, hence trapping will not take place [11]. The trapped atoms are less sensitive to some factors such as trapping beams alignment and polarisation. For example the change alignment affects the shape of the cloud of trapped atoms, but many different shapes of the cloud of trapped atoms can still have the same number of atoms. However, when alignment is changed enough to affect the trapping volume (the overlap of the trapping laser beams), this will change the shape of the cloud and significantly affect the number of the trapped atoms [11].

Chapter 3

Experimental setup

3.1 Overview

Figure 3.1 gives an overview of the MOT experiment. Two lasers are required for the trapping and repumping processes. Two commercial external cavity diode lasers (ECDL) (described in more detail in section 3.2) are used and optical isolators are placed in front of both lasers to reduce the optical feedback. Two setups for saturated absorption spectroscopy (see section 3.3) are used to lock the lasers frequencies to the trapping and repumping transitions in ^{87}Rb . For the frequency locking system a side-lock servo is used (section 3.3). The vacuum system consists of a roughing pump, a turbo-molecular pump, an ion pump to evacuate the trapping cell and a Rb source (section 3.4.1). The trapping takes place in a glass trapping cell (section 3.4.1.3). Two magnetic field coils are placed on both sides of the trapping cell to generate a magnetic field gradient (section 3.4.2). The optical setup is designed to deliver 6 trapping beams and the repump beam to the trapping cell (section 3.4.3).

Two test setups (not shown in Figure 3.1) were used to optimise the polarisation of the trapping beams (section 3.5). A setup (not shown in Figure 3.1) was built for imaging the trapped atoms and measuring fluorescence from the trap (section 3.6)

3.2 Lasers system

A MOT requires tunable, narrow spectral bandwidth it must resolve the hyperfine structural lines, the bandwidth must be in order of 300 kHz or smaller for the Rb atoms, must be easy to lock laser output frequency to an atomic transition, and highly stable output frequency at the optical transition line of the atom. Although dyes and semiconductor diode lasers are tunable, the bandwidth of their output beam is still broad compared to the natural linewidth of the atomic transition line. These requirements can be met in the ECDL. The ECDL is constructed by adding an optical element such as a diffraction grating to the normal diode laser. This grating

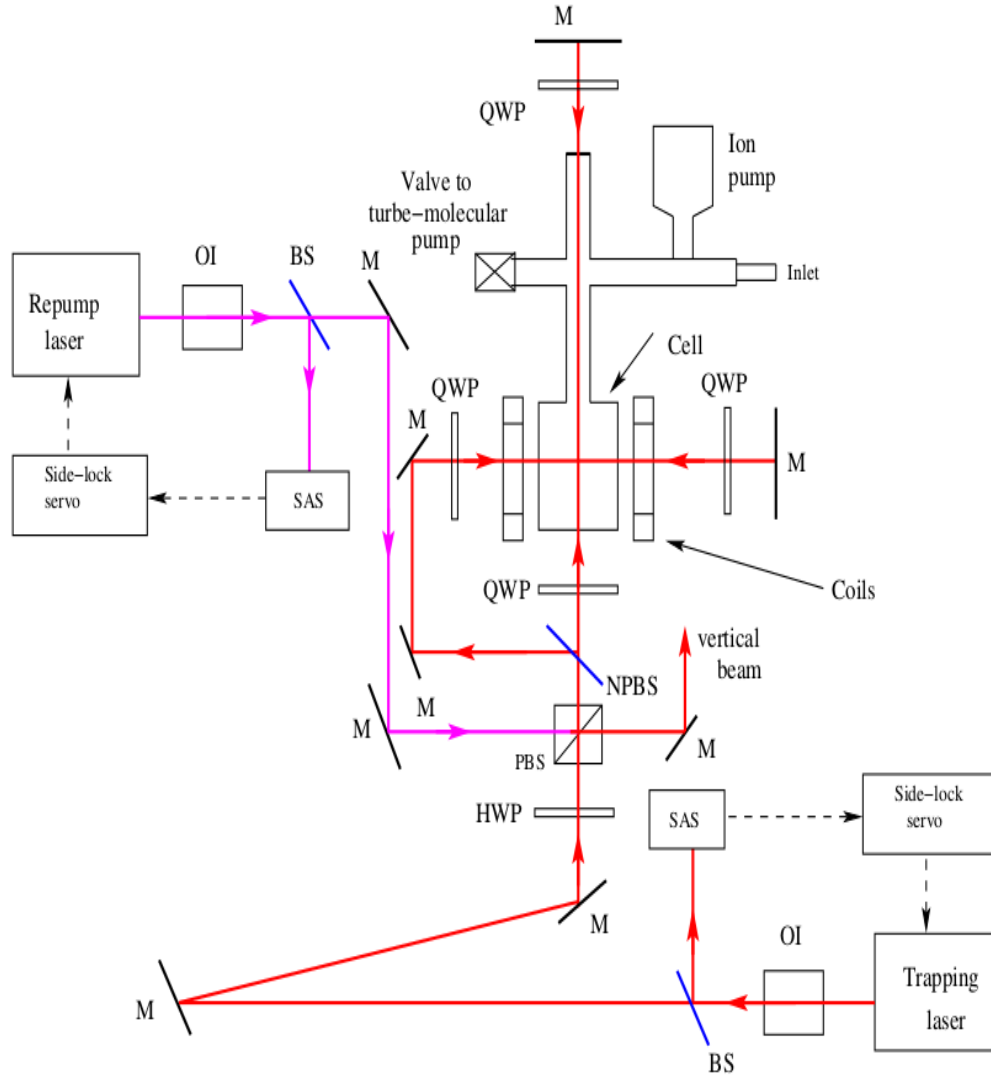


Figure 3.1: Overview of the experimental MOT setup. Key: OI-optical isolator, BS-beam splitter, SAS-saturated absorption spectroscopy, PBS-polarising beam splitter, NPBS-non-polarising beam splitter, M-mirror, HWP-half-wave plate, QWP-quarter-wave plate.

is placed in front of the diode laser output to feed the diode crystal with a small amount of its output. Hence the diode will lase at a narrow frequency similar to the frequency of the optical feedback. The grating is mounted onto a piezoelectric transducer, which allows the grating to be rotated to achieve a fine tuning and scanning of the output laser frequency under electronic control.

Two ECDLs used for trapping and repumping in our MOT setup are New Focus Vortex TLB-6913 and NEW Focus Vortex TLB-6013), respectively. They provide laser beams at the central wavelength $\lambda = 780 \text{ nm}$, the highest output power is used as the trapping, while the other is for the repumping. Table 3.1 shows the specifications of TLB-6913 and TLB-6013 ECDLs from their specification sheets. Their frequency can be locked to the desired hyperfine lines of Rb, with the aid of saturated absorption spectroscopy and side-lock electronics.

Table 3.1: Trapping and repumping ECDLs specifications

Function	Trapping	Repumping
Model	TLB-6913	TLB-6013
Tuning range	≥ 100 GHz	75GHZ
Typical power	50 mW at 780 nm	20 mW at 780.24 nm
Linewidth	≤ 300 kHz	not specified

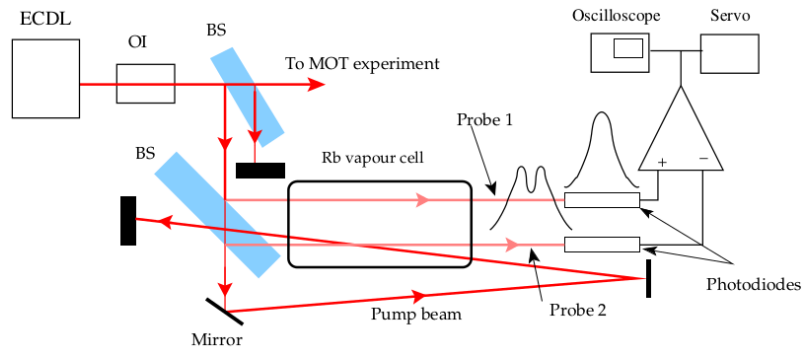
The lasers and optical setup are made on a metal lab table without any mechanism to reduce mechanical vibrations coming from the ground. For that reason the effect of vibrations on the lasers and optics is a problem. The most serious problem is that the frequencies of the lasers show jitter. Two laser holders were designed and used to isolate the lasers against vibrations. The holders were made of two metal layers and four rubber feet. The first layer is 8 mm thick. This layer is directly connected to the optical table using screws. The second layer onto which the laser is positioned is 10 mm thick. The layers are connected to each other using the four rubber feet with screws. The height of each rubber foot is 14 mm.

3.3 Saturated absorption spectroscopy setups

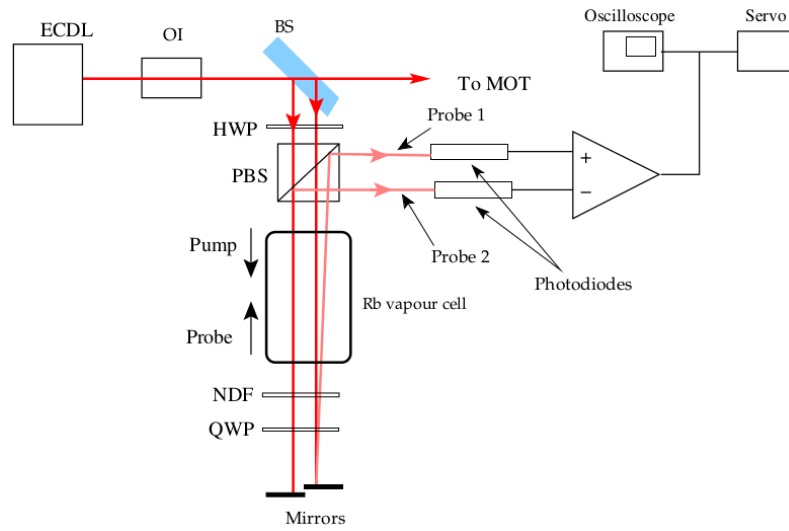
Figure 3.2 shows the three setups of the Doppler-free saturated absorption spectroscopy(SAS) experiments.

In Figure 3.2(a) the Simple SAS (S SAS) setup is depicted. The 11 mm thick beam splitter is placed in front of the diode laser to split the output laser beam into three beams. The more intense beam is directed to the main experiment, and one of the two weaker beams formed by reflections from the beam splitter will be used for the SAS. This beam passes again through another beam splitter which is a 12 mm thick glass and forms three new beams. Among these three beams, two less intense parallel beams, referred to as probe 1 and probe 2 pass through the rubidium vapour cell from left to the right. The more intense pump beam is sent to the cell in the opposite direction to the probe beams so that it overlaps with the probe 2 beam without intersecting probe 1 beam. In the (S SAS) the probe 2 is not really parallel to the pump beam, therefore they can only overlap in over short distance.

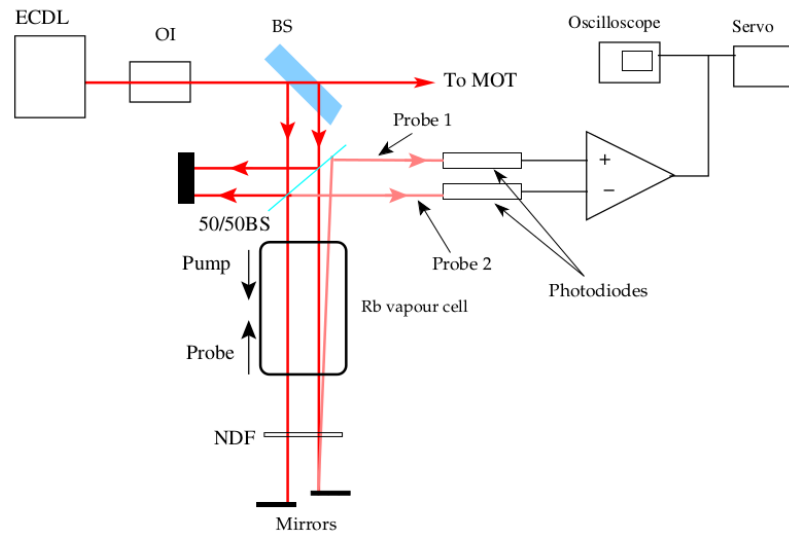
Figure 3.2(b) is polarising beam splitter saturated absorption (PBS SAS) setup. There are two new beam generated by the 11 mm beam splitter (BS). The beams pass through a half-wave plate (HWP), and a polarising beam splitter (PBS), then propagate through the rubidium vapour cell. After this cell the beams pass through a quarter-wave plate (QWP), and the neutral density filter (NDF), and then retroreflected. One of the reflected beams completely overlaps with its incoming beam. This incoming beam used as a pump beam to saturate all possible transitions in rubidium atoms, whereas the reflected beam that overlaps with the pump beam is used as a probe 2 beam. The reflected beam that does not overlap with its incoming beam is a probe 1 beam.



(a) Simple SAS setup



(b) PBS SAS setup



(c) 50/50BS SAS setup

Figure 3.2: Schematic of the experimental setups for saturated absorption spectroscopy of Rb. Key: NDF-neutral density filter, 50/50BS, other abbreviations as in Figure 3.1.

The HWP controls the polarisation of the beams in order to pass approximately all the beams through the PBS. The QWP reverses the polarisation of the reflected beams so that they can be reflected from the air gap of the PBS and detected by the photodiode detectors. The NDF attenuates the probe beams intensity. The advantage of the (SAS PBS) setup is that, probe 2 beam is parallel and well overlaps with the pump.

Lastly Figure 3.2(c) shows the 50/50 beam splitter saturated absorption spectroscopy (50/50BS SAS) setup. The two beams after (BS) encounter a 50/50 beam splitter, which reflect part of the beams and transmit the other part. The transmitted part of the beams pass through the rubidium vapour cell and the NDF then retroreflected to propagate again through the NDF and the cell. One of the reflected beams completely overlaps with its incoming beam, while the other does not. These beams are labelled as probe 2 and probe 1, respectively. The incoming beam that overlaps with the probe 2 beam is called a pump beam. Although the probe 2 beam is parallel and well overlaps with the pump beam, there is also a lot of loss in power in this setup.

For each of the setups, the two probe beams are incident onto two photodiodes. The signals produced by probe beam at the photodiodes are adjusted to be equal using a Proportional Integral Derivative (PID) controller. They are then subtracted from each other to give the Doppler-free spectral lines signal. The signal is shown on the oscilloscope. The same signal is used as an input signal to the side-lock servo (a custom made Proportional Integral Differential (PID) controller) to lock the frequency of lasers on the correct transitions of Rb for trapping and repumping. N. G. Botha has shown how a laser's frequency can be locked using the side-lock servo electronics system in her master's thesis [26].

The rubidium vapour cell is a cylinder glass cell of a length $L = 83$ mm, and outer diameter $D = 19$ mm. It contains natural rubidium vapour with the two isotopes; ^{85}Rb and ^{87}Rb . The background gas pressure of the cell is about 1×10^{-7} mbar.

3.4 Experimental setup for the MOT

3.4.1 Vacuum system and rubidium source

The vacuum system and rubidium source are important parts in the MOT experiment. In this section, we will discuss the structure of the chamber and the pump system, the rubidium source, and the trapping cells, which have been tested.

3.4.1.1 The structure of chamber and the pump system

Although trapped rubidium atoms can be achieved at pressure of 10^{-7} mbar, which is the vapour pressure of rubidium atoms at room temperature, the atoms remain in the trap for a very short time, because of the collision with the hot background atoms which increases the loss rate from

the trap. Secondly the trapped atoms cannot be seen clearly because of the bright fluorescence from un-trapped background atoms. The preferred range of pressure in MOT is (10^{-8} — 10^{-9}) mbar [11]. In the preferred range, fluorescence from the trapped atoms can be easily observed, and distinguished from the untrapped atoms' fluorescence.

A metal sealed vacuum system with suitable vacuum pumps are required in order to remove the unwanted background gas and obtain the preferred range of pressure.

Three pumps are used in our experiment: a roughing pump, a turbo pump, and an ion pump. Each one operates within a specific range of pressure as shown in Table 3.2. The arrangement of our system is depicted in Figure 3.3.

Table 3.2: Pressure range of the roughing, turbo-molecular, and ion vacuum pumps

Pump type	Pressure range (mbar)
Roughing pump	1 bar \rightarrow 1.9×10^{-3}
Turbo-molecular pump	0.5×10^{-2} \rightarrow 10^{-7}
Ion pump	10^{-6} \rightarrow 10^{-11}

As illustrated in Figure 3.3(a), the roughing pump is connected to the turbo-molecular pump via a flexible metal tube and rubber a sealed angle valve. On top of the turbo pump the electrical controlled and pneumatically operated gate valve is attached. A vacuum gauge is attached above the gate valve. The vacuum system up to this point, is sealed by rubber o-rings and Klein Flange (KF) flanges. The gate valve closes when the electric current is turned off to protect against power interruption. The metal angle seal valve is used to isolate the ultra-high metal sealed vacuum system from the turbo pump. The angle valve is connected to one of the flanges of a six-way cross. On the flange opposite to the valve, there is an inlet and a branch in which the ion pump is connected. At the other four flanges, we have the following as illustrated in Figures 3.3(a) and 3.3(b).

- 1 – The one in the front is connected to a 16 ConFlat (CF) to 40CF adapter to which the glass trapping cell is glued with vacuum epoxy.
- 2 – A window is attached to the flange opposite to the glass trapping cell. This window transmits the trapping beams along this axis.
- 3 – An extension pipe on which the electrical feed-through for the Rb dispenser is attached on the bottom flange.
- 4 – The flange on top is closed by a blank flange.

The operation procedure of the vacuum system is explained in the Appendix 7.

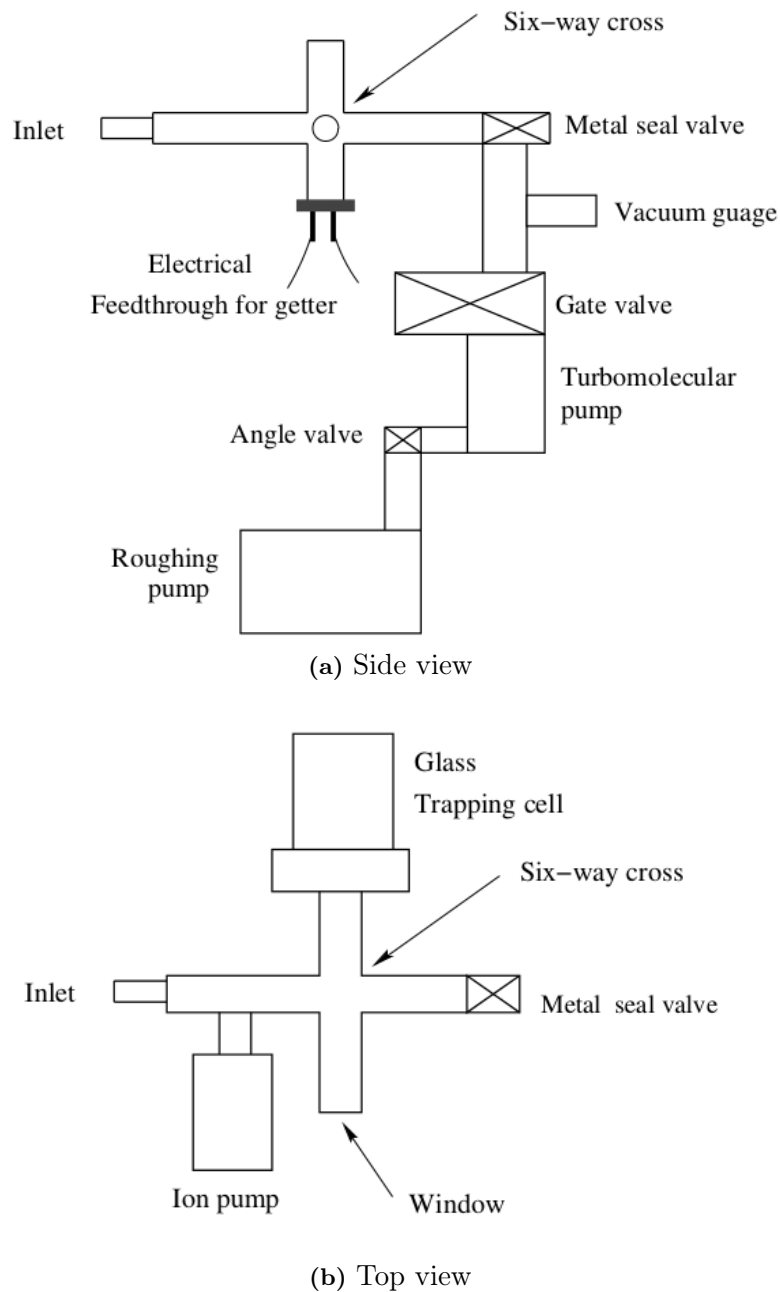


Figure 3.3: Illustration of the vacuum system setup, (a) Side view of the system, which shows the turbo and roughing pumps, the three valves, and the vacuum gauge, six-way cross, and the electrical feedthrough for the getter. (b) Top view which shows the ion pump, the trapping cell, and a window on the flange opposite to the cell.

3.4.1.2 Atomic source of the rubidium

Atomic rubidium vapour is introduced by applying electric current through a rubidium dispenser (getter). A dispenser is a controllable source of Rb vapour which contains several milligrams of a rubidium compound [19]. The rubidium compound is contained in a small stainless steel oven. This oven is affixed onto two pins of vacuum feed-through system. When a current is

applied, Rb vapour is produced and flows in the cell. The dispenser can only emit Rb atoms if the threshold current is exceeded. The more current applied to the dispenser the more rubidium vapour is produced.

There are several advantages of using the dispenser to produce the rubidium atoms in MOT experiment. It is easy to implement them inside the vacuum chamber. They can deliver rubidium atoms to the region where they are needed [27]. It is also easy to control their atomic source by switching their heating current source on, when it is required [28].

The SAES Getters S.P.A. Code 5G01258, model RB/NF/3.4/12 FT10+10 getters are used in our experiment. Its active length is 12 mm, and it can deliver 3.4 mg of Rb.

The Rb dispenser must be positioned as close as possible to the trapping cell. There must not be line of sight between the Rb dispenser and the ion pump. In our final setup the dispenser is placed inside the trapping cell. This has the disadvantages that the wire leading the dispenser reduces the cross section of the trapping beam in one direction.

3.4.1.3 Trapping Cells

Trapping cells of different geometries were tested in our setup. Firstly a spherical glass cell which has a cylindrical connection to the vacuum system was tested. The diameter of the spherical shape is 30 mm and the length and diameter of the cylindrical connection are 10 mm and 23 mm, respectively. This connection is glued by vacuum epoxy onto the 16CF to 40CF conversion flange that comes from one side of the six-way cross. By testing the expanded beam after passing through the spherical cell we observed that, the curvature of the cell's surface focuses the expanded beam at a very short distance about 150 mm from the front surface of the cell. Consequently the beam is completely distorted, and it does not even resemble a circular shape on the other side of the cell. This effect probably will distort the polarisation of the beams, and they should not be retroreflected to the cell.

Therefore, the spherical cell is replaced with a glass cell as shown in Figure 3.3(b). The cell consists of a four rectangular sides (28 mm \times 50 mm, 3 mm thick) and one square side (30 mm \times 30 mm, with 3 mm thickness). Using vacuum epoxy the open side of the cell is glued onto the 16CF to 40 CF. Observation showed that there was no distortion made by this cell on the expanded trapping beams.

3.4.2 Magnetic field coils for the trapping cell

The magnetic field gradient required for trapping is generated by applying an electrical current through two coils arranged in an anti-Helmholtz configuration, with zero magnetic point at the geometrical center. The center of the coils is aligned with the center of the trapping cell.

Two coils made of copper wire with diameter 0.6 mm are used in our setup. The coils parameters are listed in Table 3.3. These data is from the MSc thesis of CI Rigby [17], who designed these coils.

Table 3.3: Coils parameters

Coil Parameter	Value	Units
Shape	Circular	
Length of the Wire	26.52	m/coil
Loops	222	/coil
Inner Diameter	30	mm
Average Diameter	38	mm
Average Perimeter	119.32	mm
Radial Thickness	8	mm
Axial Thickness	10	mm
Face to face separation	26	mm
Center to center separation	46	mm
Wall thickness	5	mm

These coils are wound around an aluminium bobbin which has rectangular fins to remove the heat that is generated by the coils. Each bobbin has 27 mm hole in its center to allow the trapping beams to transmit through the trapping cell. The distance between the centres of the bobbins is 46 mm. This distance is large enough for the trapping cell to fit to between the coils as shown in Figure 3.4 in cross section. The coils are designed for a current 2 A [17]

3.4.3 Optical setup of MOT experiment

The optical setup for our MOT experiment is shown in Figure 3.5. Firstly, the output beam of each laser is passed through an optical isolator (OI). The OIs are used to prevent the optical feedback of the reflection of the laser's power into itself, which may cause the output beam not to be stable or even can damage the laser. The IO-5-780-HP optical isolator series is used for trapping laser beam, and IO-3-780-HP is for repumping laser. The factors 5 and 3 are the diameters of the apertures of the isolators in millimeter, and 780 nm is the wavelength for which is designed.

A small portion about 5% from each beam is split off by a beam splitter and sent to the (SAS) setup for the purpose of locking the frequency. The main beams are expanded by two convex lenses L1 with $f = 35$ mm, and L2 with $f = 500$ mm, for the trapping laser and L1 with $f = 25$ mm, and L2 with $f = 400$ mm for the repumping laser. The distance between L1 and L2 is the sum of their focal lengths. The size of the trapping laser beam after beam expansion is: 11 mm, and 12 mm for the repump laser. The height is 195 mm from the optical table. The expanded beam of the trapping laser passes a half-wave plate (HWP) and enter the polarising

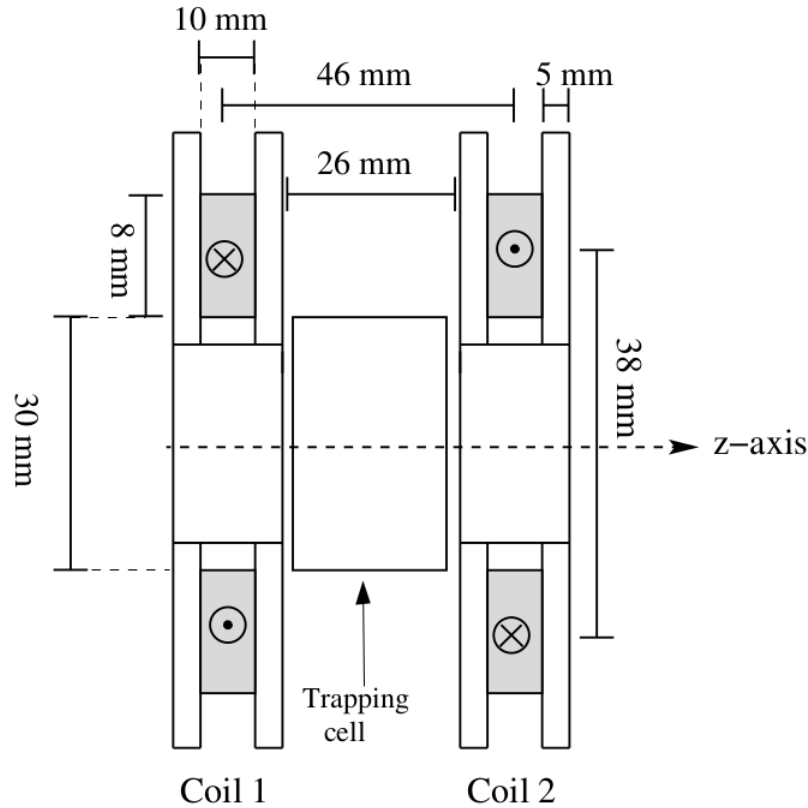


Figure 3.4: Schematic of the cross section of the magnetic coils configuration, and the current flowing through them in the opposite direction. The cross sections of the coil windings are shaded. The figure is not drawn to the scale.

beam splitter (PBS). The HWP is used to adjust and make the intensities of the six trapping beams equal at their intersection point in the trapping cell. The PBS splits the expanded beam into two beams, the reflected and transmitted beams. The reflected beam is reflected from the air gap and it is used for the vertical trapping beam. It is guided by mirrors which are aligned along the vertical axis through the center of the trapping cell. The transmitted beam is split again into two beams by the non-polarising beam splitter (NPBS), that is positioned after the PBS. The beams are guided in order to be used for the two horizontal trapping beams along the two horizontal axes. The PBS is used also to combine the repump laser beam with the three trapping beams. A part of repumping laser beam is transmitted through the PBS to combine with the vertical trapping beam, and the other part that is reflected by the PBS is combined with the two horizontal trapping beams.

The three trapping beams are aligned to propagate through the center of the cell orthogonally along the three Cartesian axes and are retroreflected by mirrors. The beams and their retro-reflection beams are aligned to intersect at the center of the trapping cell. Two quarter-wave plates (QWP) are introduced in the path of each of the three trapping beams, one on each side of the cell. The first QWP is to induce a circular polarised light according to the orientation of the fast or slow axis relative to the linear polarisation of the incident beam. The second QWP is to

correct the circular polarisation after retro reflection.

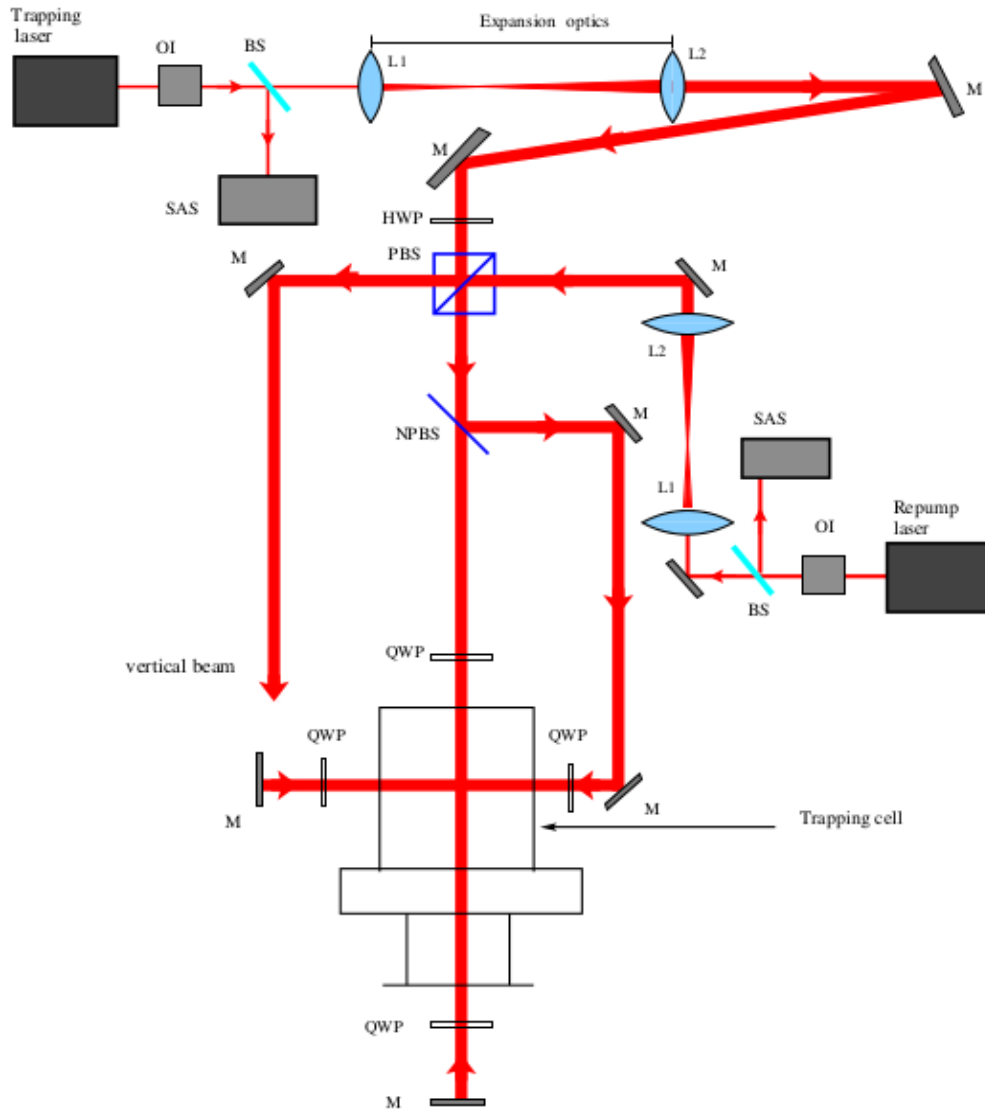


Figure 3.5: Schematic of the optical setup for the MOT experiment: the trapping and repump lasers beams, and their path through the optics on the table. Key: L-lens, other abbreviations as in the previous figures.

3.5 Test setups for optimisation of polarization of trapping beams

The polarisation state of the trapping beam plays an important role in MOT experiment. Therefore test optical setups were used to optimise the circular polarisation state of these beams as illustrated in Figure 3.6. The purpose of the setups will be discussed in Chapter 4.

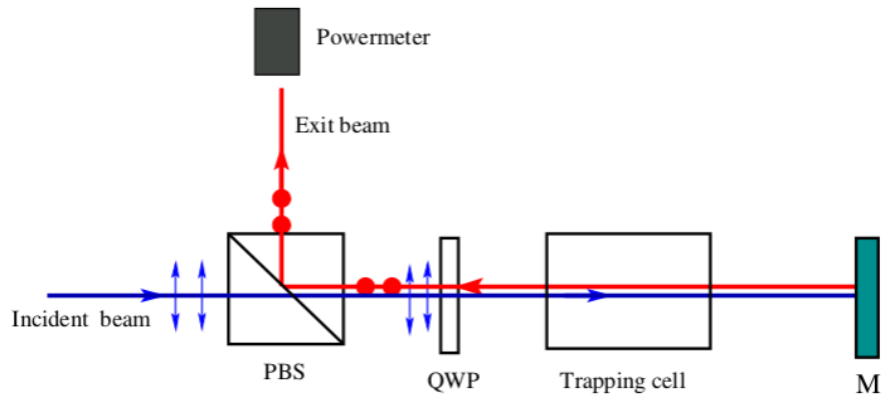
Figure 3.6(a) shows the optical setup of the test setup 1. An extra PBS is mounted before the first QWP in the trapping beam. The second QWP after the trapping cell is removed for the test. The linearly horizontal polarised beam is transmitted through PBS to pass through the QWP. If the QWP is oriented correctly, this QWP converts the linearly polarised light into circular polarisation. This circular polarised light is passed through the trapping cell and retro reflected by a mirror M, to again pass through the trapping cell and the QWP. Polarisation of the returning beam will be linearly orthogonal to the incident beam. Therefore the PBS that transmits the incident beam will reflect the returning beam to the detector. The power of the reflected beam is measured as a function of the angle of the slow axis of the QWP with respect to the horizontal axis.

The optical setup of the test setup 2 is illustrated in Figure 3.6(b). A PBS (PBS1) is inserted before the first QWP and the retroreflecting mirror is replaced by a second PBS (PBS2). The second QWP remains in position. The linearly horizontal polarised light is passed through the PBS1 and QWP1. If QWP1 is oriented correctly, the QWP1 converts the polarisation of the beam to the circular polarisation. This beam passes through the trapping cell and the QWP2. The slow axis of the QWP2 is pre-aligned at 45° ccw relative to the horizontal axis and therefore changes the polarisation from circular to linear orthogonal or parallel to the incident beam polarisation depends on the orientation of QWP1. When this beam enters the PBS2 that is positioned in a similar way as the PBS1, the horizontal and vertical polarisation components of the beam are separated. Using a powermeter, we measure the power of the reflected beam for different angles of the slow axis of the QWP1 with respect to the horizontal axis.

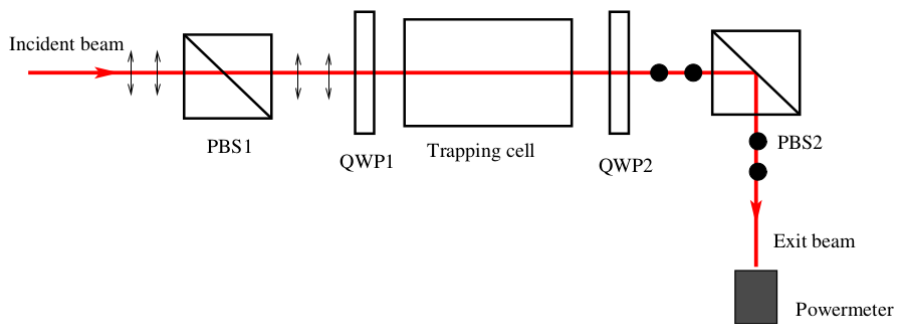
3.6 MOT Characterisation System

Two techniques were used to characterise our MOT system. The first is the imaging technique, in which the trapped atoms were imaged by a camera. In our experiment a monochromatic CMOS camera, 1280×1024 pixels (Thorlabs, DCC 1545M) is used. A lens (Thorlabs, MVL25) is mounted in front of the camera and 400 mm from the center of the trapping cell. This lens is used to focus the light emitted from the trapped atoms onto the camera. The camera is connected to a computer with a USB cable to show the image.

The second technique is the measurement technique in which a photodiode detector is used to measure the fluorescence from the trapped atoms. Figure 3.7 depicts our imaging system, which consists of a lens system, a photodiode detector that is capable of converting the light into a voltage, an amplifier and oscilloscope to read the amplified voltage. Two lenses are used to image the fluorescence. A large collimating lens L_1 with $f = 100$ mm, $D = 50$ mm is used as a collection lens, where f is the focal length and D is the diameter of the lens, which could be able to collect significant amount of the fluorescence. The collimating lens is positioned at a distance equal to its focal length from the center of MOT. The focusing lens L_2 with $f = 100$ mm, $D = 50$ mm focuses the collimated fluorescence onto the photodiode, which is positioned at f_2 away from the



(a) Test setup 1



(b) Test setup 2

Figure 3.6: Schematic of the optical setup of the tests for optimisation of the circular polarisation states of the trapping beams.

photodiode. The photodiode and lens system are inserted into a black tube, and positioned at an appropriate side of the trapping cell, in order to prevent unwanted scattered photons to hit the active area of the photodiode.

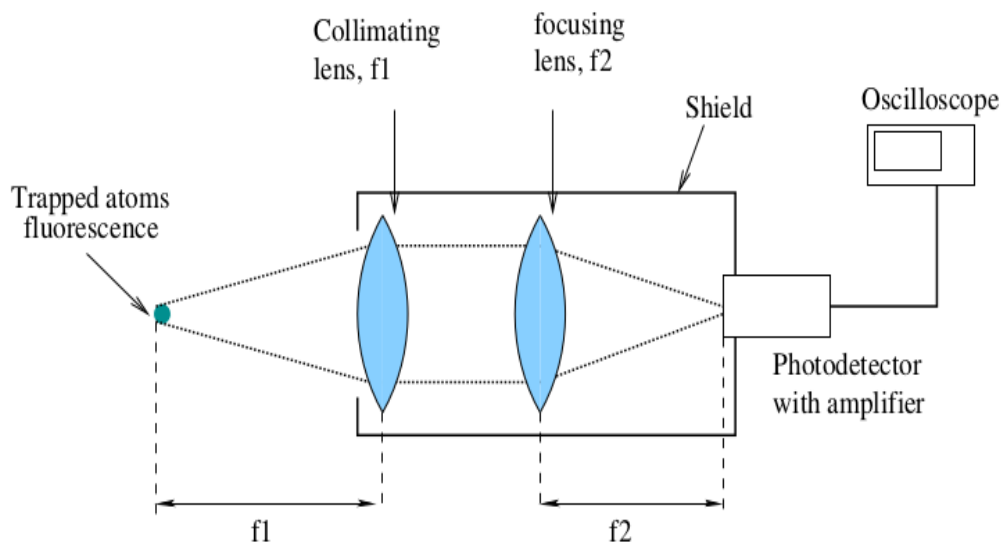


Figure 3.7: Illustration of the setup for the measurement of the fluorescence from the trapped atoms.

Chapter 4

Results and Discussions

4.1 ECDL characteristics

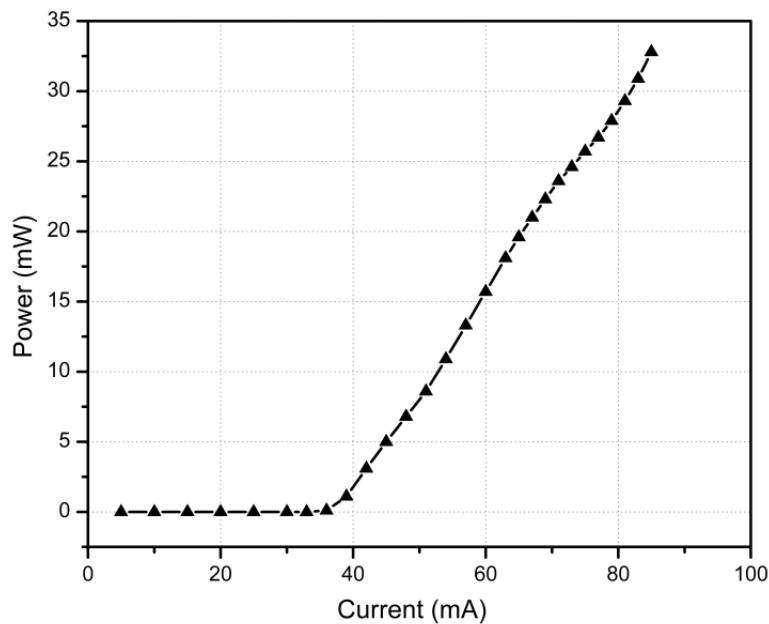


Figure 4.1: Trapping laser turn on curve

Figure 4.1 shows the turn-on curve of the ECDL that is used as a trapping laser (New Focus Vortex TLB-6913). The laser output power is measured as a function of the injection current of the diode laser at room temperature 23.2 C° , using a powermeter. The powermeter is positioned at 20 cm distance from the laser source. As seen in the Figure 4.1 the lasing threshold current is 36.0 mA (32.77 mA was measured in a previous measurement recorded in the thesis of Charles Rigby [17]), which is the injection current at which the diode starts to lase. After the threshold current the power increases linearly with the current. The slope efficiency is 0.69 mW/mA (0.35 mW/mA previous measurement [17]) which is calculated from a linear fit of the measured power

after the threshold current. The maximum output power of the laser is 85.0 mW at 32.8 mA injection current.

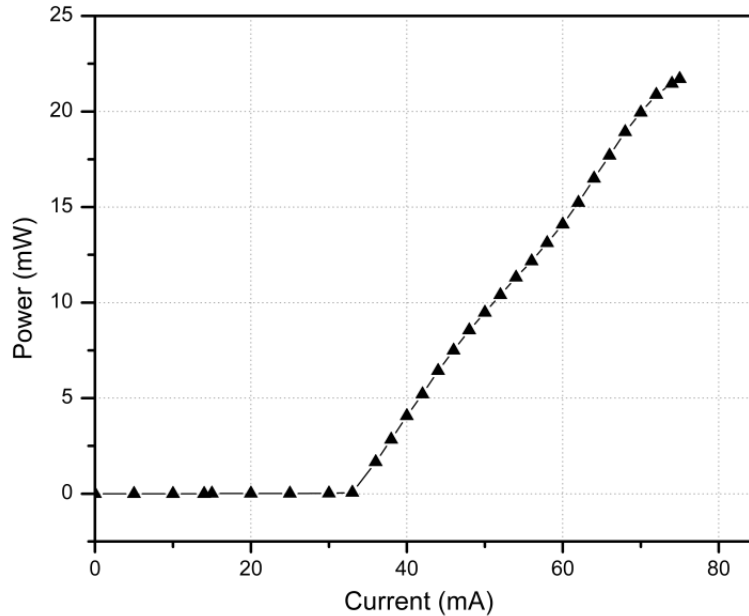


Figure 4.2: Repumping Laser turn on curve

Figure 4.2 shows the turn-on curve of the ECDL, that is used as a repumping laser (New Focus Vortex LTB 6013). The threshold current is 33.0 mA (31.83 mA previous measurement [17]). Similarly the power increases linearly with the injection current after the threshold current. The slope efficiency is 0.53 mW/mA (0.48 mW/mA previous measurement [17]), and the maximum output power of the laser is 21.7 mW which is reached when the injection current is 75 mA.

4.2 Saturated absorption spectra

Figure 4.3 shows the Doppler broadened absorption spectrum of the rubidium atoms at room temperature. The signal was taken with PBS SAS setup (3.2b) and with both probe 2 and pump beams blocked, while probe 1 beam was unblocked. The four peaks observed are due to the ground state hyperfine splitting of ^{85}Rb and ^{87}Rb . The peaks are labelled by the isotopes and the F values of the ground state from which the line originates. The reason why the peaks of the ^{85}Rb are larger than those of ^{87}Rb is because ^{85}Rb is approximately three times more abundant than ^{87}Rb [29]. The separation between the two outer peaks of ^{87}Rb is 6.5 GHz and that of the two inner peaks of ^{85}Rb is 3 GHz. It should be noted that the peaks due to the excited state hyperfine splitting are not resolved and cannot be seen.

The relative frequency shift of the ground state hyperfine level, as given in Table 9.1 in the Appendix 9 were used to calibrate the horizontal axis of the spectrum. The frequency of each level was plotted against the pixel position of the peaks as read from the oscilloscope. The linear

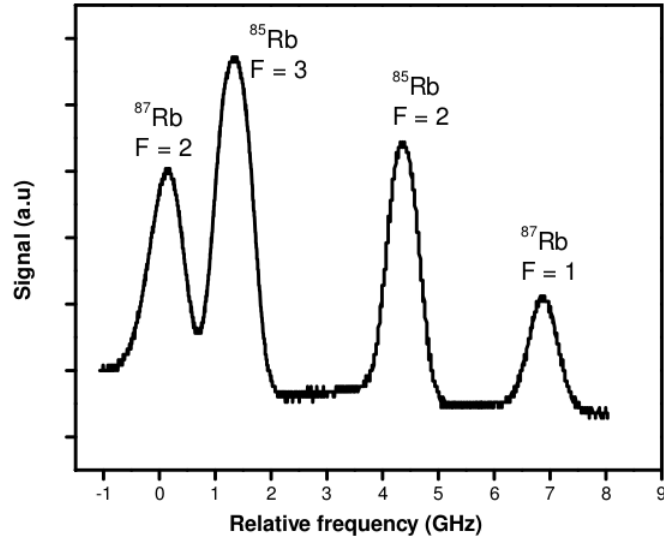


Figure 4.3: Doppler-broadened absorption spectrum of Rb atoms measured with only probe 1 beam unblocked

relation between the pixel position and the relative frequency of the peaks is shown in Figure 4.4. The FWHM of the peaks were calculated after the calibration and results are listed in Table 4.1. All the FWHM of the peaks in this section were just measured at the half height of the peaks, no fitting method has been used.

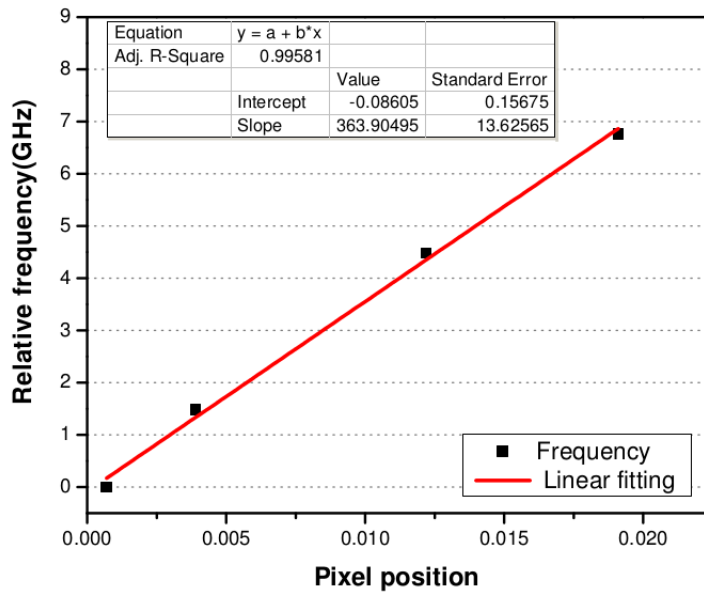
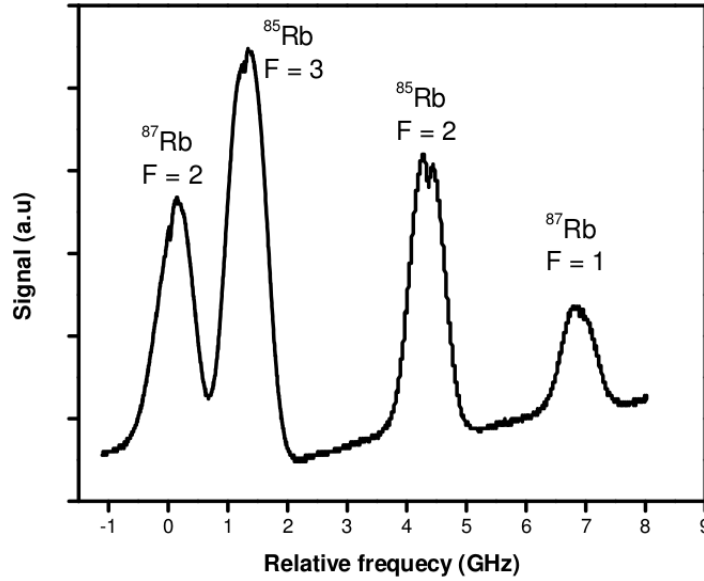


Figure 4.4: Horizontal axis calibration of Doppler broadened absorption spectrum of Rb. The relative frequencies of the ground levels as given by the author in [30] are plotted against the pixel position of the peaks as read from the oscilloscope.

Table 4.1: FWHM of the Doppler-broadened absorption spectrum of Rb peaks

Peak	^{87}Rb F = 2	^{85}Rb F = 3	^{85}Rb F = 2	^{87}Rb F = 1
FWHM/GHz	0.60	0.69	0.62	0.57

Figure 4.5 shows the Doppler-broadened absorption spectrum with hyperfine structure (dips) on each peak of the Rb atoms. The signal was measured with probe 1 beam blocked in the PBS SAS experiment. The FWHM of the spectral peaks were calculated after the calibration of the horizontal axis and the results are shown in Table 4.2.

**Figure 4.5:** Doppler-broadened absorption spectrum of Rb atoms with the hyperfine structure**Table 4.2:** The FWHM of the Doppler-broadened absorption spectral peaks of Rb atoms with hyperfine structure

Peak	^{87}Rb F = 2	^{85}Rb F = 3	^{85}Rb F = 2	^{87}Rb F = 1
FWHM/GHz	0.56	0.69	0.66	0.69

Figures 4.3 and 4.5 show that the hyperfine structure cannot be resolved if Doppler broadening is present, because of the Doppler-free saturated absorption spectrum features are much smaller than the Doppler broadened lines. Therefore by subtracting the signals of the two probe beams, the Doppler-free saturated absorption spectrum is measured in which the hyperfine structure of the spectral peaks is resolved. The hyperfine structure of each of the Doppler Broadened spectral lines consists of six peaks. Three of these peaks are due to the real hyperfine transitions and are labelled by the F' values of the hyperfine excited state to which the atoms are excited.

The hyperfine transition occurs when the atoms are at rest, the frequency of the both pump and probe laser beams at the resonance with the transition. The excitation by the pump laser reduces the absorption of the probe beam.

The other three are due to crossover transitions, and they are often more pronounced than those due to hyperfine transitions [31].

The crossover peaks occur when a group of atoms in the ground state level interacts with the overlapping beams. Some atoms would be travelling at the correct velocity to see the probe beam frequency Doppler red-shifted to one spectral line, while the same atoms would see the pump beam frequency Doppler blue-shifted to the other spectral line. Since the two spectral lines share the same ground level, saturation occurs. The crossover peaks labelled with * has two subscript numbers. The numbers are the F' values of the two excited states involved in the crossover. The conditions for the crossover transition to occur are the laser frequency must be halfway between two transition frequencies and these two transition must also have the same ground state.

The hyperfine structures of the spectral lines of Rb atoms were obtained using three different SAS experiment setups.

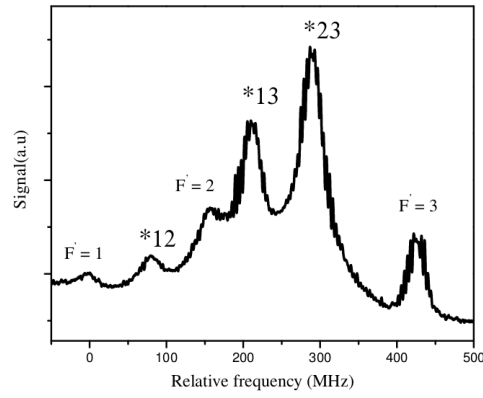
Figure 4.6 shows the Doppler-free hyperfine structure of the spectral line of ^{87}Rb with $5^2\text{S}_{1/2}$ $F = 2$ as ground state. The structure was obtained using the three SAS setups, and the results are shown in Figures 4.6(a), 4.6(b) and 4.6(c). All the six peaks are resolved. Three of the six are due to the hyperfine transitions from $5^2\text{S}_{1/2}$ $F = 2$ to $5^2\text{P}_{3/2}$ $F' = 1, 2$ and 3 , while the other three are due to crossover transitions. The cooling transition of ^{87}Rb is $5^2\text{S}_{1/2}$ $F = 2 \rightarrow 5^2\text{P}_{3/2}$ $F' = 3$. The frequency of the trapping laser can be locked to the slope on the red side frequency of the cooling transition. Table 4.3 shows the FWHM of the peaks, which were calculated after the calibration of the horizontal axis of the spectrum.

Table 4.3: The FWHM of peaks of the hyperfine structure of $5^2\text{S}_{1/2}$ $F = 2$ spectral line of ^{87}Rb

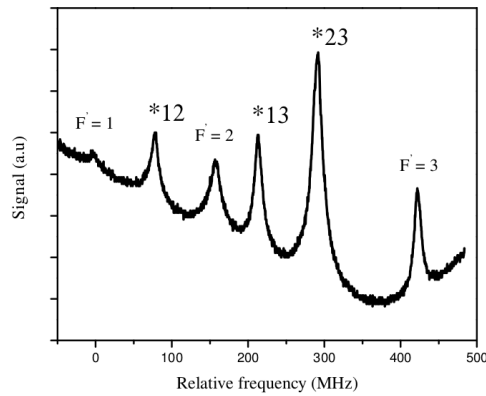
Peak	$F=2 \rightarrow F'=1$	$F=2 \rightarrow F'=2$	$F=2 \rightarrow F'=3$	* ₁₂	* ₁₃	* ₂₃
Simple SAS	-	-	25.2	25.2	25.2	32.9
PBS SAS	-	14.7	9.8	9.8	9.8	14.7
50/50BS SAS	-	16.4	9.8	13.1	16.4	16.5

Table 4.4: The FWHM of peaks of the hyperfine structure of the $5^2\text{S}_{1/2}$ $F = 1$ line of ^{87}Rb

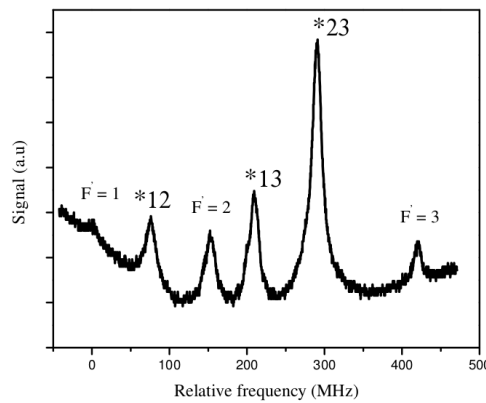
Peak	$F=1 \rightarrow F'=0$	$F=1 \rightarrow F'=1$	$F=1 \rightarrow F'=2$	* ₀₁	* ₀₂	* ₁₂
Simple SAS	-	-	22.3	-	-	32.8
PBS SAS	-	8.6	13.3	-	7.6	15.2
50/50BS SAS	-	10.7	18.8	-	9.0	15.2



(a) Simple SAS setup



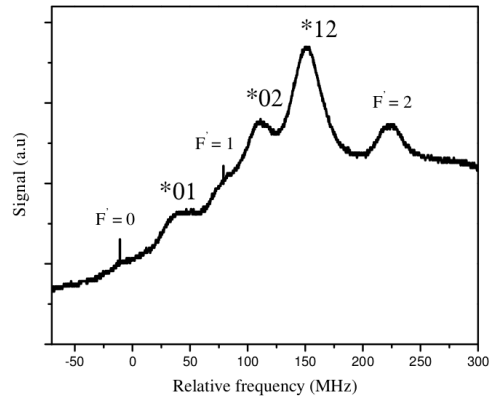
(b) PBS SAS setup



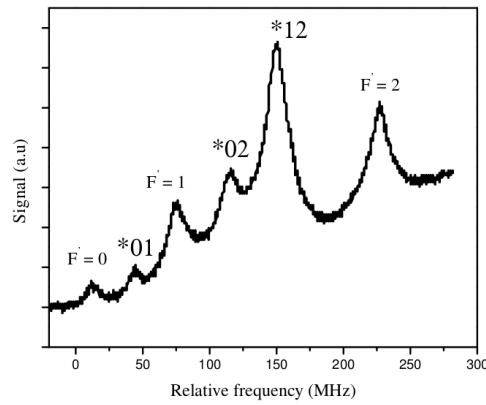
(c) 50/50BS SAS setup

Figure 4.6: The Doppler-free hyperfine structure of the ^{87}Rb line with $5^2\text{S}_{1/2}$ $F = 2$ as ground state. The structure was obtained by the all three different SAS setups as indicated below each graph.

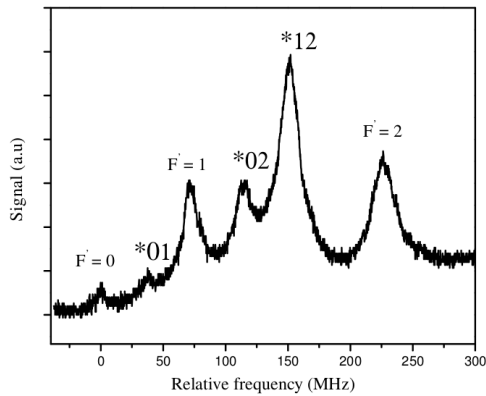
Figure 4.7 shows the Doppler-free hyperfine structure of the spectral line of ^{87}Rb with $5^2\text{S}_{1/2}$ $F = 1$ as ground state. The structure was obtained using the three SAS setups, and the results are shown in Figures 4.7(a), 4.7(b) and 4.7(c). The peaks in Figure 4.7(a) are more broadened than the frequency separation between them, hence some of the peaks are not resolved. In Figures 4.7(b) and 4.7(c) all the six peaks are resolved. The repumping transitions of the ^{87}Rb is $F = 1$



(a) Simple SAS setup



(b) PBS SAS setup



(c) 50/50BS SAS setup

Figure 4.7: The Doppler-free hyperfine structure of the ^{87}Rb line with $5^2\text{S}_{1/2}$ $F = 1$ as ground state. The structure was obtained by the all three SAS setups as indicated below each graph.

$\rightarrow F' = 1$ and 2 . The frequency of the repumping laser can be locked to the slope on the red side of one of the repumping transitions. The FWHM of the spectral peaks is shown in Table 4.4.

The calculated frequency shift of the hyperfine levels of ^{87}Rb shown in Table 2.3 was used to calibrate the horizontal axis of the spectrum in Figures 4.6 and 4.7. The frequency shift of each

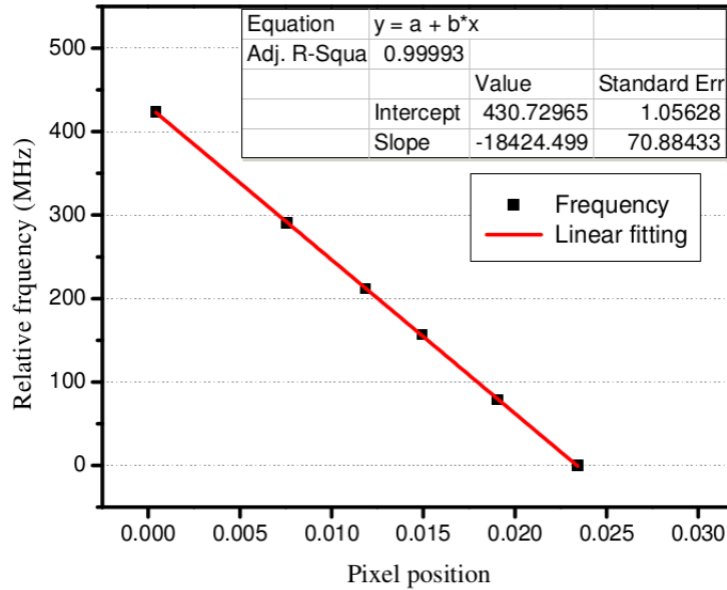


Figure 4.8: Calibration of the horizontal axis of the hyperfine structure of the $5^2S_{1/2}$ $F = 2$ line. The frequency shift of each level is plotted against the pixel positions of the peaks.

hyperfine level is plotted against the pixel positions of peaks. Figure 4.8 shows an example of the horizontal axis calibration for the hyperfine structure. The graph shows a linear relation between the pixel position of the peaks and the frequency of the peaks of the $5^2S_{1/2}$ $F = 2$ spectral line of ^{87}Rb .

The hyperfine structure of ^{85}Rb was also measured using our SAS setups.

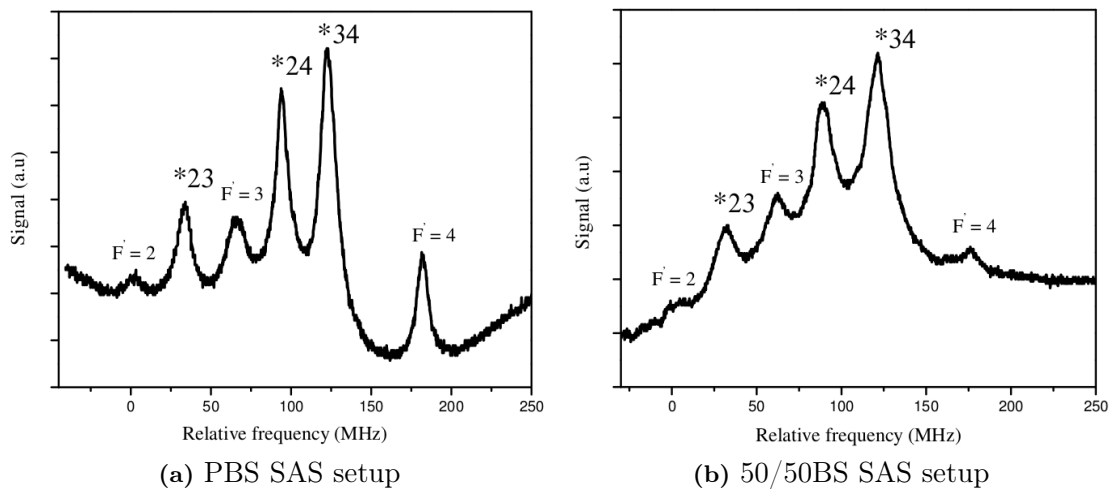


Figure 4.9: The Doppler-free hyperfine structure of the line of ^{85}Rb with $5^2S_{1/2}$ $F = 3$ as ground state. The structure was obtained by PBS SAS and 50/50BS SAS setups as indicated below each graph.

Table 4.5: The FWHM of peaks of the hyperfine structure of the $5^2S_{1/2}$ $F = 3$ line of ^{85}Rb

Peak	$F=3 \rightarrow F'=2$	$F=3 \rightarrow F'=3$	$F=3 \rightarrow F'=4$	* ₂₃	* ₂₄	* ₃₄
PBS SAS	-	10.0	8.3	8.3	7.5	8.3
50/50BS SAS	-	-	-	8.2	9.6	12.3

Figure 4.9 is the hyperfine structure of the ^{85}Rb line with $5^2S_{1/2}$ $F = 3$ as ground state. The structure was only obtained using the PBS SAS and 50/50BS SAS setups, and the results are shown in Figures 4.9(a), 4.9(b) and 4.9(c). All the six are resolved. Three peaks are due to the hyperfine transitions from $5^2S_{1/2}$ $F = 3$ to $5^2P_{1/2}$ $F' = 2, 3$, and 4, while the other three are due to crossover transitions. The cooling transition of ^{85}Rb is $5^2S_{1/2}$ $F = 3 \rightarrow 5^2P_{1/2}$ $F' = 4$. After the horizontal axis calibration the FWHM of peaks were calculated and listed in Table 4.5.

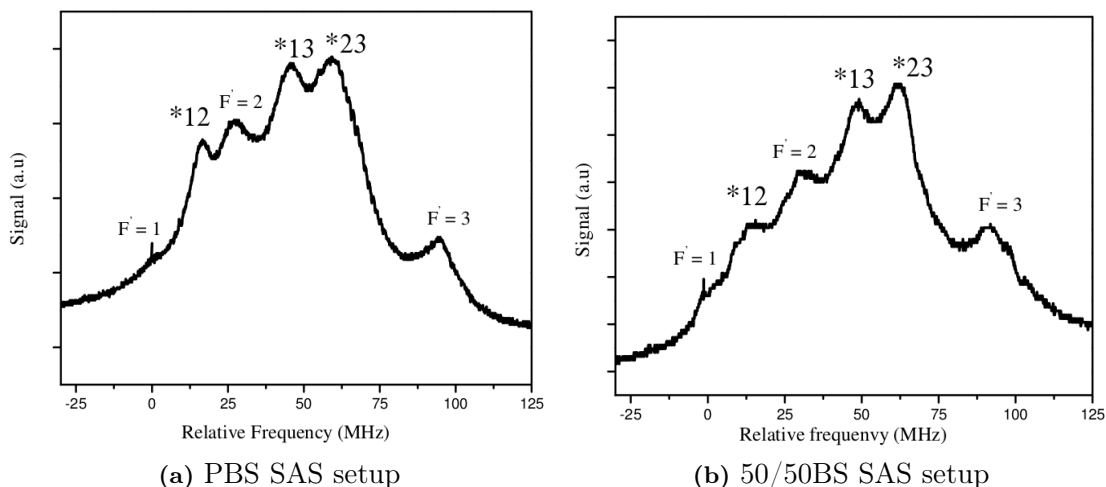

Figure 4.10: Doppler-free hyperfine structure of $5^2S_{1/2}$ $F = 2$ of ^{85}Rb . The structure was obtained by the PBS SAS and 50/50BS SAS setups as indicated below each graph.

Figure 4.10 shows the hyperfine structure of the ^{85}Rb line with $5^2S_{1/2}$ $F = 2$ as ground state. The structure was obtained using the PBS SAS and 50/50BS SAS setups, and the results are shown in Figures 4.10(a) and 4.10(b). The hyperfine peaks are resolved, but it was impossible to calculate their FWHM. This is because of the frequency spacing between the hyperfine peaks is very small compared with peaks width, and all the six peaks are in range of 90 MHz. The repumping transitions of ^{85}Rb is $5^2S_{1/2}$ $F = 2 \rightarrow 5^2P_{3/2}$ $F' = 2$ and 3.

The horizontal axis of the spectra in Figures 4.9 and 4.10 were calibrated using the frequency shift of the hyperfine levels that is given in Table 9.2 in the Appendix 9.

From the FWHM results in Tables 4.3, 4.4 and 4.5 it is clear that the simple SAS setup measures broader peaks than PBS SAS and 50/50BS SAS setups.

The broadening of the hyperfine spectral peaks can be explained as follows: The FWHM of the hyperfine structure peaks can be affected by the angle between the two overlapped probe and

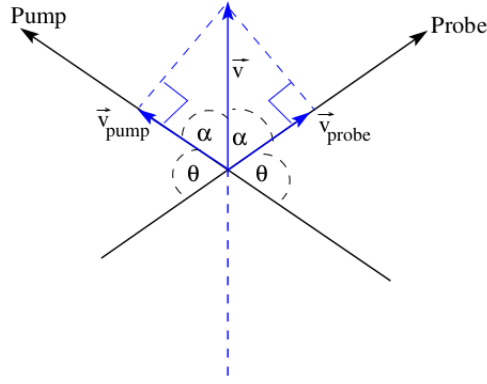


Figure 4.11: Illustration of an atom moving in the plane with velocity $|\vec{v}|$, and has equal velocity components along the direction of probe and pump beams $|\vec{v}_{\text{pump}}| = |\vec{v}_{\text{probe}}|$.

pump beams [31; 26]. When the probe and pump beams are not perfectly parallel, we consider the atoms having a velocity vector that is at the same angle (α) to the pump and probe beams as shown in Figure 4.11. The atoms with $|\vec{v}| \neq 0$ can have the same velocity component along the propagation axis of both beams $|\vec{v}_{\text{pump}}| = |\vec{v}_{\text{probe}}|$. This will contribute to the SAS signal, but at shifted frequency $\nu = \nu_{\text{laser}} - \frac{1}{h}\vec{k} \cdot \vec{v}_{\text{probe}}$, consequently the peak is broadened. In the PBS SAS and 50/50BS SAS setups the angle θ between the two overlap beams is approximately 0.5° , hence $|\vec{v}_{\text{pump}}| = |\vec{v}_{\text{probe}}| = |v|\sin(0.25)$. At this small value of the angle θ a very narrow FWHM of the spectral lines are expected. But in the Simple SAS $\theta \approx 5^\circ$, hence $|\vec{v}_{\text{pump}}| = |\vec{v}_{\text{probe}}| = |v|\sin(2.5)$. As a result the measured FWHMs by the Simple SAS are broader than the FWHM measured by the PBS SAS and 50/50BS setups by a factor. In the experimental result this factor is approximately 2.2.

In general, all hyperfine structure peaks obtained by the PBS SAS and 50/50BS SAS setups are narrower than those of the Simple SAS setup as shown in Table 4.3. This is because the angle between the overlapping beams in the Simple SAS setup is bigger compared with the other two SAS setups.

In our setup of the MOT experiment the two lasers have to be locked to the red slope of the cooling transition and the repumping transition peaks. The PBS SAS setup was used to lock the frequency of the trapping laser to the cooling transition, while for the repumping laser was used the 50/50 SAS setups. This is because the hyperfine structure from these two SAS setups are resolved better than that of Simple SAS setup, and it is easy to determine the peaks due to the cooling or repumping transitions in order to lock frequency of the lasers at the correct transitions.

Figure 4.12 shows the fluorescence of the two probe and pump beams passing through the rubidium vapor cell in the PBS SAS setup. The trapping laser frequency is locked at the cooling transition of ^{87}Rb .

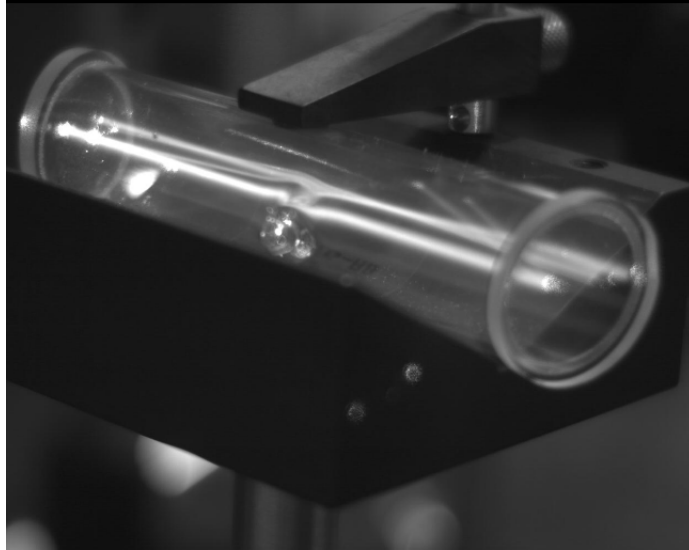


Figure 4.12: The fluorescence of the two probes and pump beams passing through the Rb vapor cell, when the laser frequency was locked at the cooling transition.

When we were trying to lock the laser frequency, there was about 500 Hz frequency noise (frequency jitter) on the signal. This makes the signal to be not stable hence the locking process can be difficult in the presence of this noise. This noise is probably due to the effect of vibrations on the ECDLs, in spite of efforts to reduce the vibrations.

4.3 Polarization and power control of the trapping beams

4.3.1 Power control

The ECDL provides vertical linearly polarised light. In MOT setup, several elements are used to achieve the correct circular polarisation of the trapping beams in the trapping cell. Figure shows 4.13 the optical setup of the polarisation for our MOT experiment.

The Optical Isolator (OI) rotates the vertical linearly polarised beam of the ECDL by 45° clockwise (when looking into beam), in order to block reflection from getting back to the laser source.

The OI consists of an input linear polariser, with its transmission axis vertically aligned, a rotator based on the Faraday effect, and an output polariser or analyser. The transmission axis of the analyser is rotated by 45° relative to the transmission axis of input polariser. The vertical polarised light from the ECDL pass the input polariser to enter the Faraday rotator, which rotates the plane of polarisation by 45° into the direction of the analyser in order to pass through it. The direction of the rotation is independent of the propagation direction of the beam, hence any light reflected back into the OI will be rotated by 45° again, and then it will be

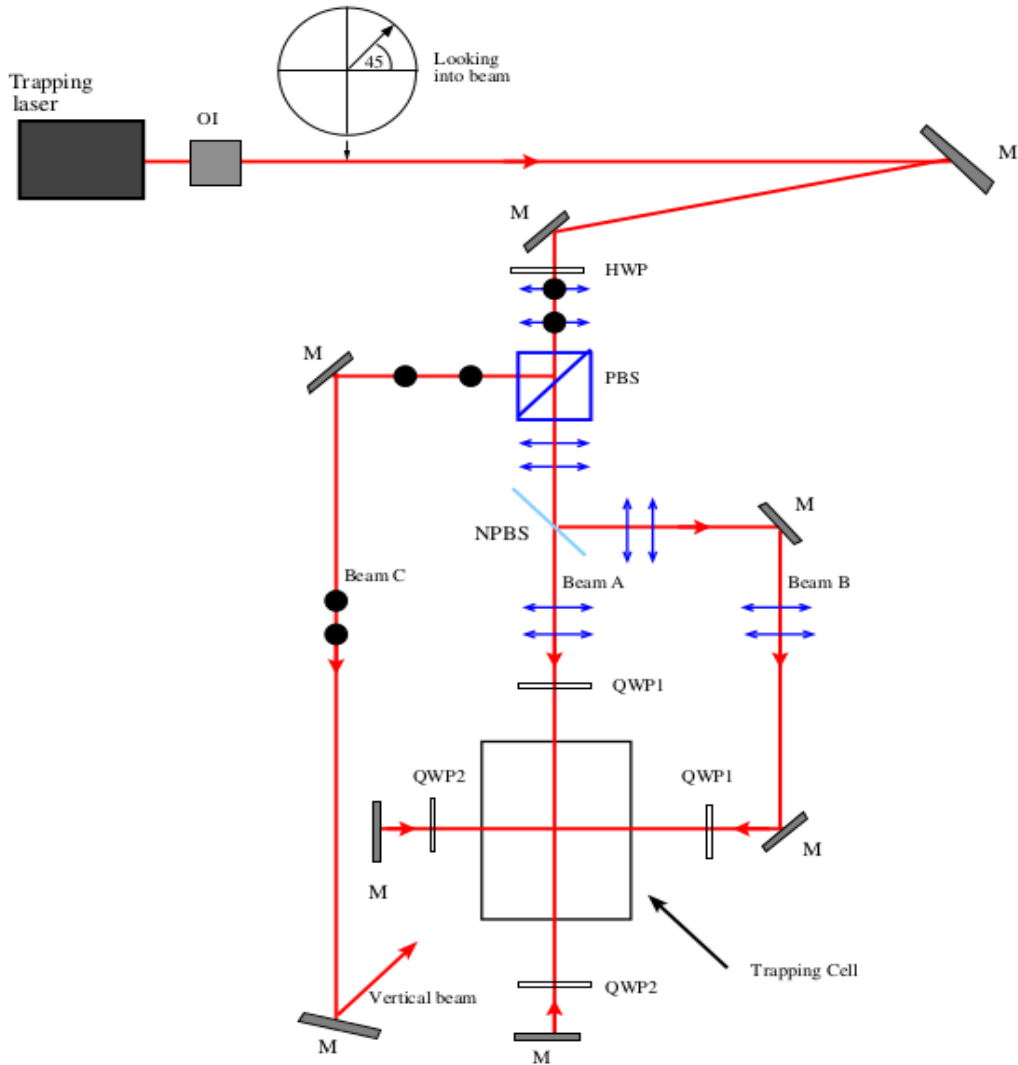


Figure 4.13: Optical setup of the circular polarisation for the MOT experiment

linearly polarised at 90° relative to the input beam. Therefore this reflected light will be blocked by the input polariser.

A half-wave plate (HWP) and polarising beam splitter PBS are used to adjust the fraction of power reflected off for the vertical beam. The transmitted beam is split approximately 50/50 by a non-polarising beam splitter (NPBS).

Six quarter-wave plates (QWP) are used to provide the correct circular polarisation of the trapping beam in the trapping cell. The orientation of the first QWP in each beam is critical. The second QWP can have any orientation.

Jones matrix formulation is used to calculate the effect of the polarising element on the beams. The calculation is compared to the experimental measurements in order to characterise the polarisation of different parts of the setup.

The beam after the OI is the linearly polarized at $+45^\circ$ with respect to the horizontal axis see

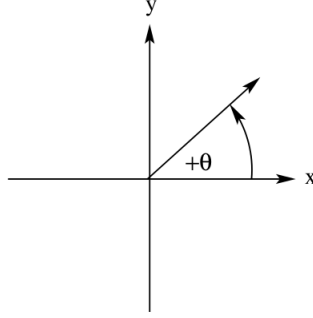


Figure 4.14: Illustration for measurement of angle

Figure 4.14. This can be expressed by the following vector according to the Jones formulation [32]

$$E_{45} = \frac{1}{\sqrt{2}} \begin{bmatrix} 1 \\ 1 \end{bmatrix} \quad (4.3.1)$$

The expression of the Jones matrix for the HWP is (as proven in Appendix 8)

$$M_{\text{HWP}}(\theta) = \begin{bmatrix} \cos 2\theta & \sin 2\theta \\ \sin 2\theta & -\cos 2\theta \end{bmatrix} \quad (4.3.2)$$

where θ is the angle that the fast axis of the HWP makes with respect to the horizontal axis. The polarization of the output beam from the HWP can be calculated as follows:

$$E_t = M_{\text{HWP}}(\theta) \cdot E_i \quad (4.3.3)$$

where E_t and E_i the electric field vectors of the transmitted and the incident beams, respectively. M_{HWP} is the transformation matrix of the HWP. By substituting equations (4.3.2) and (4.3.1) into equation (4.3.3) we obtain

$$E_t = \frac{1}{\sqrt{2}} \begin{bmatrix} \cos 2\theta + \sin 2\theta \\ \sin 2\theta - \cos 2\theta \end{bmatrix}. \quad (4.3.4)$$

Equation (4.3.4) shows that the transmitted light is linearly polarized but its plane of polarisation has been rotated. The ratio of the horizontal component of the light to the vertical component of the light depends on the angle θ of the slow axis of the HWP. The beam power is proportional to the amplitude square of the electric field vectors. Hence by squaring the two components of the electric field vector equation (4.3.4), we obtain the power of the horizontal and vertical components of the beams separately as

$$I_x = \left(\frac{1}{\sqrt{2}} \cos 2\theta + \frac{1}{\sqrt{2}} \sin 2\theta \right)^2 \quad (4.3.5)$$

$$I_y = \left(\frac{1}{\sqrt{2}} \sin 2\theta - \frac{1}{\sqrt{2}} \cos 2\theta \right)^2. \quad (4.3.6)$$

If we assume that light beam after OI is linearly polarised at an angle ϕ , instead of 45° , equation (4.3.1) will become

$$E_\phi = \begin{bmatrix} \alpha \\ \beta \end{bmatrix}. \quad (4.3.7)$$

And equations (4.3.5) and (4.3.6) will be

$$I_x = (\alpha \cos 2\theta + \beta \sin 2\theta)^2 \quad (4.3.8)$$

$$I_y = (\alpha \sin 2\theta - \beta \cos 2\theta)^2 \quad (4.3.9)$$

where α and β represent the two elements of the Jones vector that describes the linear polarisation of the beam after the OI. Their values can be determined from the fitting of the experimental measurements. The angle ϕ is determined by the formula

$$\phi = \tan^{-1}(\beta/\alpha) \quad (4.3.10)$$

Experimentally the vertical and horizontal polarised beam are separated by the PBS. The PBS transmits the horizontal linearly polarised beam, and reflects the vertical linearly polarised beam. The power of these beams are measured as a function of θ , the orientation angle of the slow axis of the HWP with respect to the horizontal axis. The measured power and the calculated results from equations (4.3.8) and (4.3.9) are plotted in Figure 4.15.

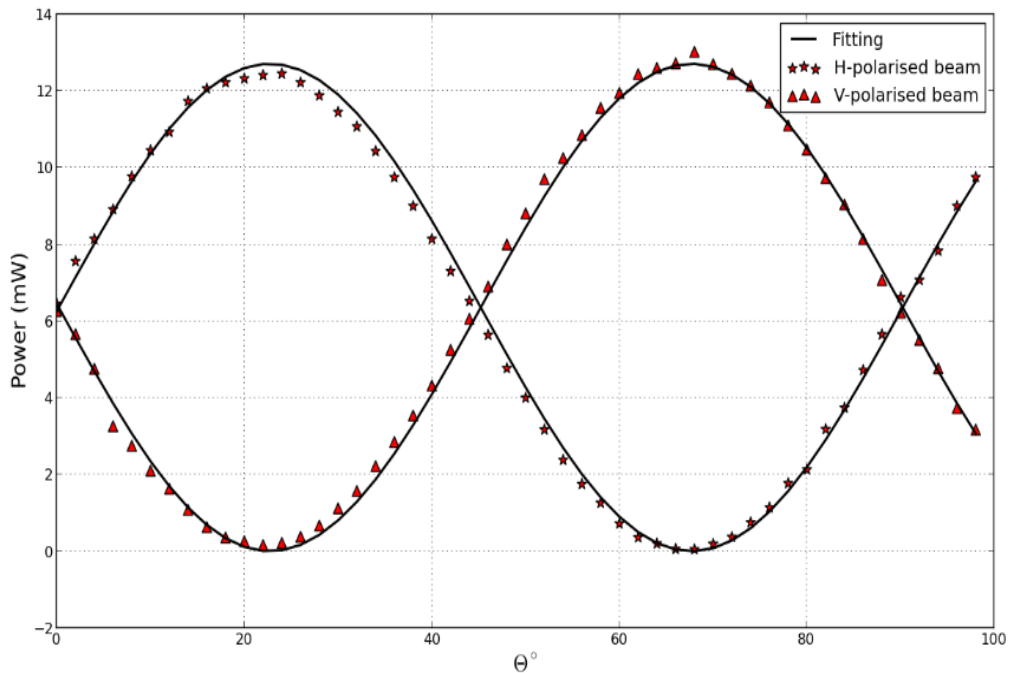


Figure 4.15: powers of the linearly horizontal and vertical polarized light varying the angle θ , which the fast axis of the HWP makes with horizontal axis.

Equations (4.3.8) and (4.3.9) have been fitted to the measured power data by a least squares fit to determine the value of α and β . The χ^2 fitting formula used in the fitting algorithm is

$$\text{Least square value} = \left(\frac{1}{N-1} \sum_{i=1}^N [(I_{\text{Exp}})_i - (I_{\text{Th}})_i]^2 \right)^{1/2}. \quad (4.3.11)$$

N is the number of experimental data of points, I_{Exp} is the experimentally measured power, I_{Th} is the theoretical calculated power from equations (4.3.8) and (4.3.9). The values of α and β were adjusted by the fitting algorithm using a selected step size and within a selected range. The pair of α and β values that yields the smallest SD value was determined.

Table 4.6: Fitting parameters and ϕ values for different ranges and fixed step size

Step size	Range	α	β	Least square value	ϕ
0.001	0 – 5	2.975	3.02	0.000366623	45.43007
0.001	0 – 10	2.975	3.02	0.000366623	45.43007
0.001	0 – 15	2.975	3.02	0.000366623	45.43007
0.001	0 – 20	2.975	3.02	0.000366623	45.43007

Table 4.7: Fitting parameters and ϕ values for different steps size and fixed range

Step size	Range	α	β	Least square value	ϕ
0.1	0 – 10	3.0	3.0	0.0271429	45
0.01	0 – 10	2.98	3.02	0.0028992	45.38197
0.001	0 – 10	2.975	3.02	0.000366623	45.43007
0.0001	0 – 10	2.9754	3.02021	9.86887×10^{-6}	45.42811

Tables 4.6 and 4.7 shows the fitting parameters and the values for the different ranges and steps size. The angle ϕ of the linearly polarised light after the OI is also determined, which is 45.42811 for the minimum SD value. As can be seen in Table 4.6, changing the range in which α and β lie has no effect on their values. More accurate values of α and β can be obtained by reducing the step size as shown in Table 4.7.

In Figure 4.15 the variation of the horizontal and vertical polarised powers as function of θ is shown. As shown in the graph, at $\theta = 22.5^\circ$ the power of the horizontal polarised transmitted beam by PBS is maximum, and a the power for the vertical polarised reflected beam by the PBS is minimum, because the incident beam at this angle is totally horizontally polarised. Whereas at $\theta = 67.5^\circ$ incident beam is completely vertically polarised, therefore maximum power is measured for the vertical polarisation and minimum for the horizontal polarisation. At $\theta = 0^\circ, 45^\circ$, and 90° the ratio of the beam polarisation is 1:1. Our interest is at $\theta = 5.6^\circ$ and 39.4° , where the ratio of the horizontal to vertical polarisation power is about 2:1, because the horizontal polarised beam will be split again into two equal power beams by a NPBS. The HWP, PBS, and NPBS enable

us to adjust the the division of power between the vertical and horizontal trapping beams in the MOT experiment.

4.3.2 Circular polarisation of trapping beams

Two test setups, as discussed in section 3.5, were used to optimise the orientations of the first quarter wave plate in each trapping beam. The purpose of the first setup as shown in Figure 3.6(a) is to determine the two optimum orientations $\theta = \frac{\pi}{4}$ and $\theta = \frac{-\pi}{4}$ of the slow axis of the QWP. At these two orientations perfectly circularly polarised light, either clockwise (cw) or counter-clockwise (ccw) is obtained after the QWP. The cw polarisation is induced, when the slow axis of the QWP is at $\frac{\pi}{4}$ clock wise with respect to the linear polarisation of the light before the QWP. Whereas the ccw polarisation is obtained when the slow axis is at $\frac{\pi}{4}$ ccw with respect to the linearly polarisation of the light before the QWP.

In Figure 3.6(a) linear horizontally polarised light is chosen as an incident beam. The component of the electric field of such beam has the following vector expression as given by Jones

$$E_H = \begin{bmatrix} 1 \\ 0 \end{bmatrix}. \quad (4.3.12)$$

The beam passes the QWP with its slow axis is oriented at angle θ with respect to the horizontal axis. The transformation Jones matrix of QWP rotated by an angle θ ccw relative to horizontal axis is give as

$$M_{\text{QWP}}(\theta) = \begin{bmatrix} \cos^2 \theta - i \sin^2 \theta & \cos \theta \sin \theta (1 + i) \\ \cos \theta \sin \theta (1 + i) & -i \cos^2 \theta + \sin^2 \theta \end{bmatrix}. \quad (4.3.13)$$

The proof of this transformation matrix is shown in the Appendix 8.

Hence the polarisation state of the output beam after the QWP is described by (same form as Equation (4.3.3))

$$E = M_{\text{QWP}}(\theta) \cdot E_H \quad (4.3.14)$$

$$= \begin{bmatrix} \cos^2 \theta - i \sin^2 \theta \\ \cos \theta \sin \theta (1 + i) \end{bmatrix}. \quad (4.3.15)$$

The beam passes through the trapping cell, and is retroreflected by a mirror M. The reflection reverse the cw polarisation into ccw, or vice versa. Therefore equation (4.3.15) can be rewritten for the reflected beam as follows

$$E_{\text{retro}} = \begin{bmatrix} 1 & 0 \\ 0 & -1 \end{bmatrix} \cdot E = \begin{bmatrix} \cos^2 \theta - i \sin^2 \theta \\ -\cos \theta \sin \theta (1 + i) \end{bmatrix}.$$

The reflected beam passes through the QWP on its return path. However, this time the slow axis of the QWP is at the angle $-\theta$ with respect to the horizontal axis due to the opposite propagation direction of the beam. Therefore the polarisation of the final beam is described by

$$\mathbf{E}_F = \begin{bmatrix} \cos^2 \theta - i \sin^2 \theta & -\cos \theta \sin \theta (1 + i) \\ -\cos \theta \sin \theta (1 + i) & -i \cos^2 \theta + \sin^2 \theta \end{bmatrix} \cdot \mathbf{E}_{\text{retro}} \quad (4.3.16)$$

$$= \begin{bmatrix} \cos^4 \theta - i \sin^4 \theta \\ -2 \cos \theta \sin \theta \end{bmatrix} \quad (4.3.17)$$

The real part of the y-component of the electric field vector of the final beam, expressed in equation (4.3.17), is calculated for different angles and squared, in order to use as the calculated power of the beam.

The calculated power of the transmitted beam is plotted on the same graph with the measured power from the test experiment. The result is shown in Figure 4.16.

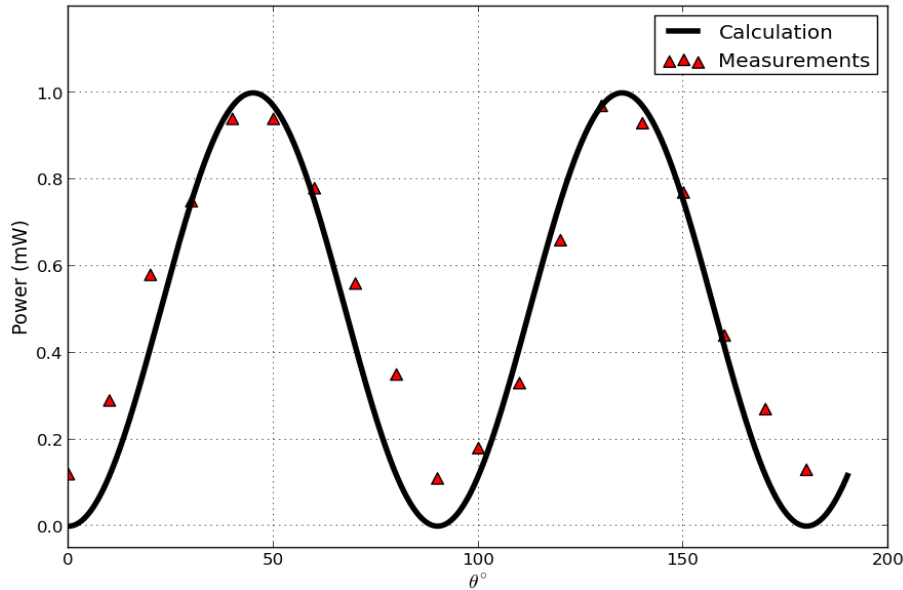


Figure 4.16: Result of Test 1: The power of the reflected beam by the (PBS) power as a function of the angle of the slow axis of the QWP with respect to the horizontal axis.

In Figure 4.16, the maximum measured power is at $\theta = \frac{\pi}{4}$ and $\frac{3\pi}{4}$. These are the two orientations of the slow axis of QWP that give a ccw and cw circular polarisation. At $\theta = \frac{\pi}{4}$ ccw circular polarisation is induced, hence the reflected beam is cw circular polarised. When this beam passes the QWP it is converted to a vertical linear polarisation and totally reflected by the PBS. While at $\theta = \frac{3\pi}{4}$ cw circular polarisation is induced and the reflected beam becomes ccw polarised. Therefore it will also be converted to a vertical linearly polarisation when it is again passes through the QWP, and it will be totally reflected by the PBS.

In test 1 it is not possible to determine from the result whether the slow axis is at 45° or at 135° . If the slow and fast axis are incorrectly labelled on the QWP mount (as was the case with one of our QWP's) this will not show in test 1. Therefore the second test is needed. The second test setup that is depicted in Figure 3.6(b) is used to distinguish between the two optimum orientations of the QWP1 axis, that were determined by the first test.

As shown in Figure 3.6(b), a linearly polarised beam passes through the PBS1 and the QWP1. The slow axis of the QWP1 can be rotated by an angle θ ccw with respect to the horizontal axis. Hence the beam's polarisation after QWP1 is given as

$$\mathbf{E} = \begin{bmatrix} \cos^2 \theta - i \sin^2 \theta \\ \cos \theta \sin \theta (1 + i) \end{bmatrix}. \quad (4.3.18)$$

The beam after the trapping cell enters the QWP2. The slow axis of the QWP2 is oriented at -45° with respect to the horizontal axis. The polarisation of the output beam from the QWP2 is given by

$$\mathbf{E} = \begin{bmatrix} 1 - i & -i - 1 \\ -1 - i & 1 - i \end{bmatrix} \begin{bmatrix} \cos^2 \theta - i \sin^2 \theta \\ \cos \theta \sin \theta (1 + i) \end{bmatrix} \quad (4.3.19)$$

$$= \begin{bmatrix} \cos^2 \theta - \sin^2 \theta - i(1 + 2 \cos \theta \sin \theta) \\ 2 \cos \theta \sin \theta - 1 + i(\sin^2 \theta - \cos^2 \theta) \end{bmatrix}. \quad (4.3.20)$$

The vertically polarised component of this beam is totally reflected by the second PBS to the detector.

The real part of the y component of the electric field amplitude of the final beam, in equation (4.3.20) is calculated for different angles and squared. This calculated powers and measured powers for this test are shown in Figure 4.17. The calculated power is multiplied by 1.6 factor in order to match with the measured power.

As shown in Figure 4.17 the minimum and maximum measured power are at $\frac{\pi}{4}$ and $\frac{3\pi}{4}$ respectively. The minimum is when the slow axis of the QWP1 is oriented at $\frac{\pi}{4}$ and that of the QWP2 is at $\frac{-\pi}{4}$. This means that the beam after QWP1 is ccw circular polarised, but when it passes the QWP2 it becomes linearly horizontally polarised. This is because the QWP2 cancel the 90° phase shift made by the QWP1. Therefore the beam is transmitted by the PBS2 and a minimum power is measured. But when the slow axes of both QWP1 and QWP2 are at 135° or -45° there is a cw circular polarisation after QWP1, and vertically linear polarisation after QWP2. This is because QWP2 again makes 90° phase in the same direction of that made by QWP1. Therefore the beam is reflected by PBS2 and a maximum power is measured at this point.

From the tests the slow axis orientations 45° and 135° (or -45°) can well be determined and distinguished in order to obtain the ccw or cw circular polarisation. We have to decide which one of them is required for a certain trapping beam. This depends on the polarisation of

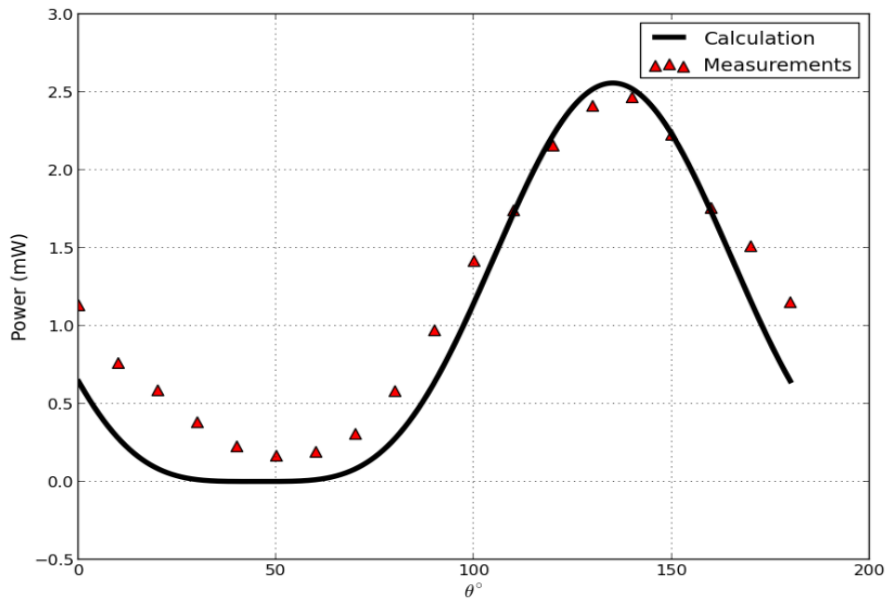


Figure 4.17: Result of Test 2: The power of the reflected beam by the PBS2 as varying the slow axis angle of the QWP1 with respect to the horizontal axis.

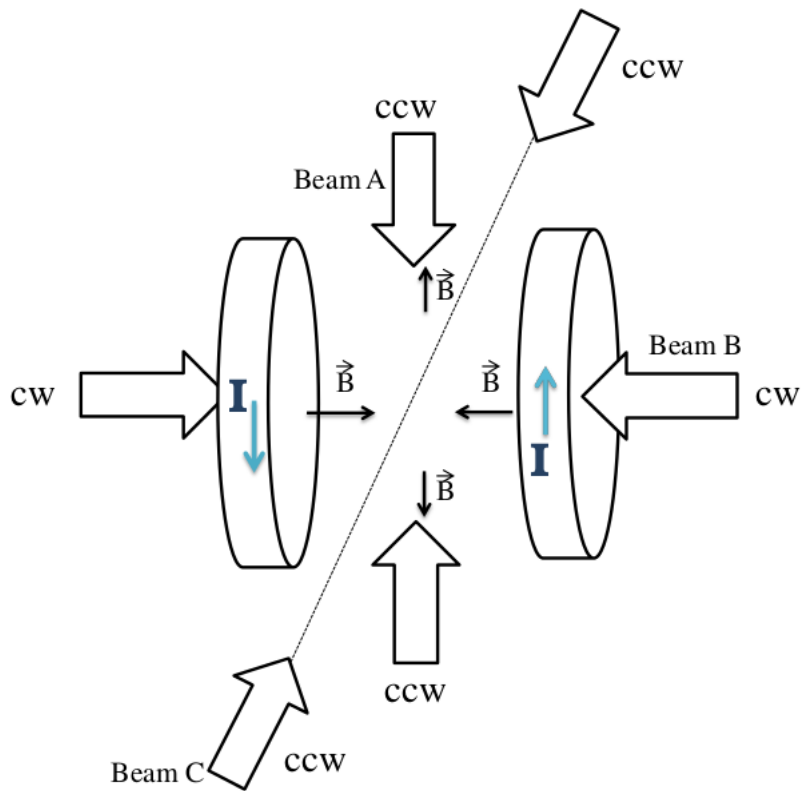


Figure 4.18: Schematic illustration of a cooling and trapping experiment using two symmetric magnetic coils with oppositely directed currents and three pairs of counter-propagating laser beams illuminating the atom from all six directions. See Appendix 6 for the details

the beam before the QWP and orientation of the magnetic field vectors along that axis. The polarisation requirements (cw or ccw) of the three trapping beams are shown in Figure 4.18. These polarisations are obtained in the following way:

- Beam A is linearly horizontally polarised before QWP1 and along the axis in the trap, the \vec{B} fields are pointing outwards from the center. Consequently, a ccw polarised light trapping beam is needed along this axis, therefore the QWP1 slow axis is rotated by 45° ccw relative to the linear horizontal polarisation direction axis.
- Beam B is linearly horizontally polarised before QWP1 and \vec{B} fields are pointing inward toward the center along this axis. As a result, a cw polarised light trapping beam is needed along this axis, therefore the QWP1 slow axis is rotated by 45° cw relative to the linear horizontal polarisation direction.
- Beam C is linearly polarised (polarisation direction parallel to the propagation direction of beam C before it is reflected upwards into the cell) before QWP1 and \vec{B} are pointing outwards from the center. Consequently, ccw polarised light trapping beam is needed along this axis, hence the QWP1 slow axis is rotated by 45° ccw relative to the linear polarisation direction.
- The retroreflected beams will have correct polarisation for any orientation of QWP2.

4.4 Power and losses in optical setup

Figure 4.19 shows the measured optical power of trapping laser beam at different points in the optical setup. As seen in Figure 4.19, the total power produced by the trapping laser is 37.1 mW at 85 mA injection current. 35.6 mW optical power is measured for the transmitted beam through the OI. 1.8 mW power is split off by the BS and sent to the SAS setup. 32.9 mW is transmitted through the BS. This beam will be divided into three beams with roughly equal optical power. 29 mW power is measured before the PBS. The PBS transmits a beam with 17.8 mW, and reflects a beam with 9.0 mW power. The optical power ratio of the two beams depends on the slow axis orientation of the HWP. The reflected beam is guided by optics and aligned vertically to the trapping cell. Its power is 6.1 mW after QWP. The transmitted beam by the PBS is again divided by NPBS into two parts. The first one which transmits through the NPBS has 7.0 mW power after QWP. The other reflects from the NPBS, is guided by optics to the trapping cell, and aligned orthogonally to the first one along the horizontal axis. Its measured power after QWP is 5.7 mW.

Table 4.8 shows the power of the three incoming trapping beams and the power of their retroreflected beams. It is necessary that the three trapping beams have approximately equal optical power in order to exert same force from the six directions of the trapping beams onto the atoms. The effect of the unbalanced trapping beams is shown in section 4.7.

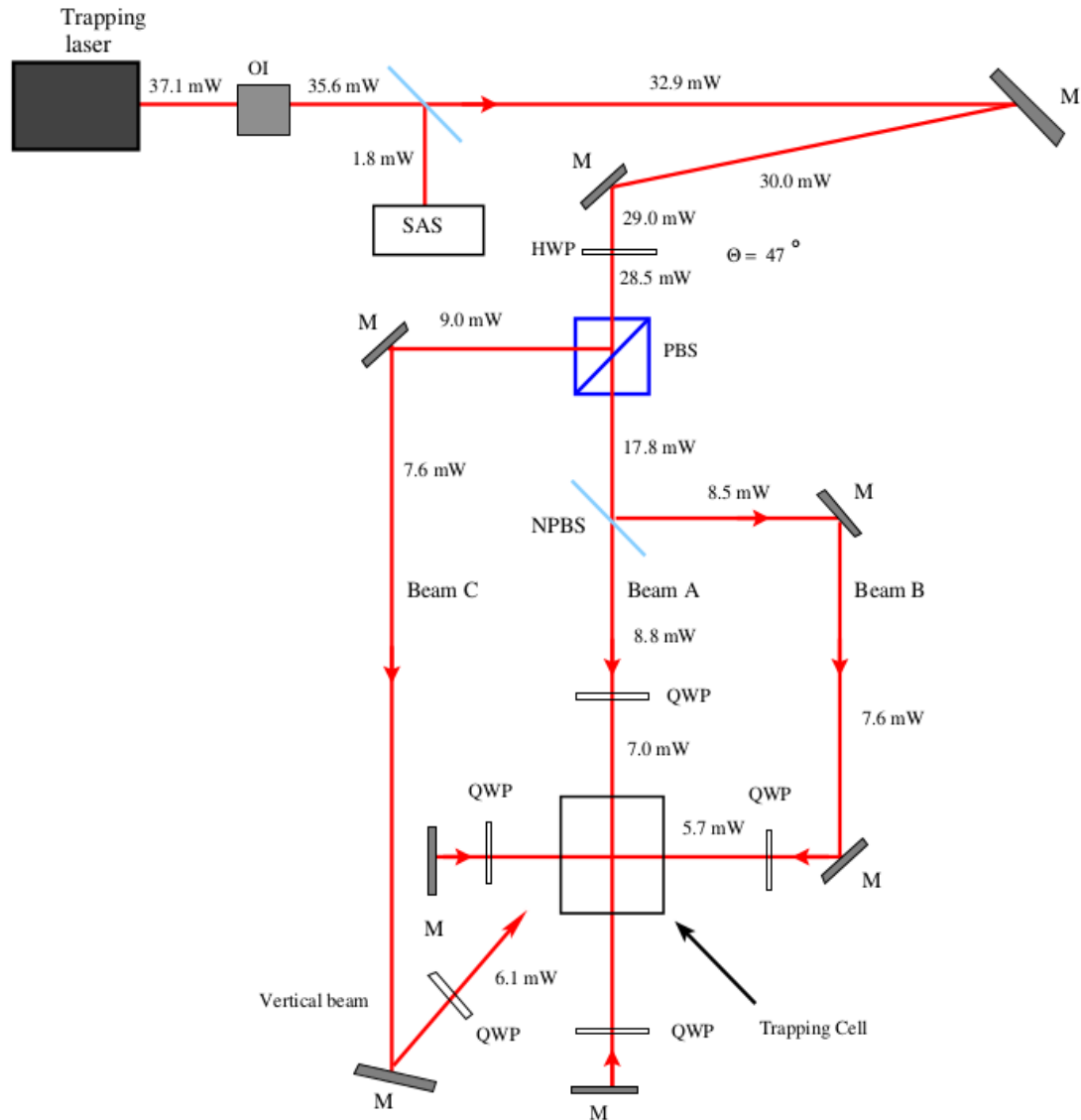


Figure 4.19: Power and losses in the optical setup of the trapping laser

Table 4.8: The power of the trapping beams and their retroreflected beams

Beam	Incoming beam power	Reflected beam power
Beam A	7.0 mW	5.0 mW
Beam B	5.7 mW GHz	4.0 mW
Beam C	6.1 mW	4.3mW

Figure 4.20 shows the optical power of the repumping laser beam. The output power produced by the repumping laser is 20.7 mW when the injection current is 73.5 mA. 18.3 mW is transmitted through the OI. 0.7 mW and is sent to the SAS setup by the BS. The transmitted beam by the BS is linearly combined with all three beams of the trapping laser using PBS. As seen in Figure 4.20, the power of the three beams of the repumping laser before reaching to trapping cell are 3.4 mW, 2.6 mW and 4.0 mW. It is neither necessary that the repumping laser is combined with

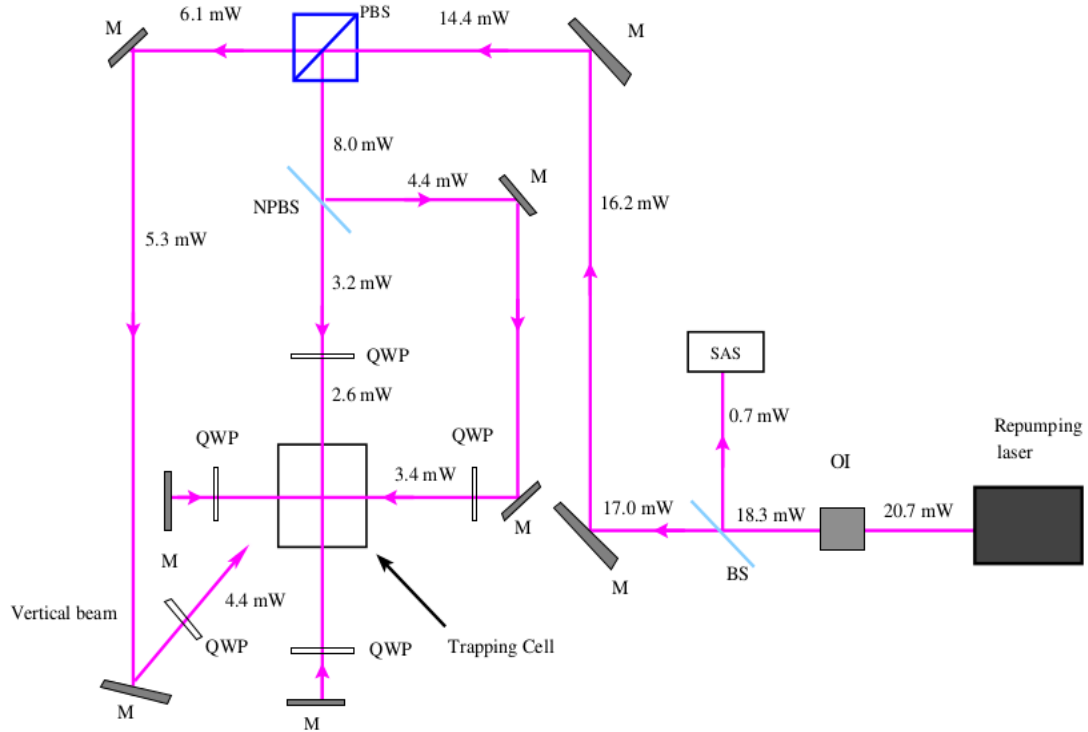


Figure 4.20: Power and losses in the optical setup of the repumping laser

all the trapping beams nor that its power is equally distributed among them.

From the result above, it appears that over 10% power is lost on each reflection from a mirror. This is because mirrors are gold mirrors, not dielectric mirrors specifically designed for 780 nm.

4.5 Result on the magnetic field gradient

Figure 4.21 shows the magnetic field value between the two coils along x-axis. This graph was obtained using equation (2.3.1), for $R = 0.023$ m, $h = 0.046$ m, $I = 0.5$ Ampere, and $n = 222$ loops. As can be seen in Figure 4.21, the magnetic field at the center along x-axis is linearly proportion to the distance from the coils. The calculated magnetic field gradient along x-axis in the range (-0.015 to 0.015 m) is 14.8 G/cm. The field has maximum values at the position of the coils and zero in the center between the coils.

Figure 4.22 shows the magnetic field gradient along the propagation axes of the three trapping beams (x , y , z). The simulation was made by M. Morrissey using Radia software. More details can be found in the Appendix 10. The magnetic coil parameters used in the calculation are shown in Table 3.3. As shown in Figure 4.22, the magnetic field gradients along the x-axis for the current values 0.5 Ampere and 1 Ampere are 14.8709 G/cm and 29.7418 G/cm, respectively. For the same current values, the field gradients along the other two axes y and z are 7.42745 G/cm and 14.8709 G/cm.

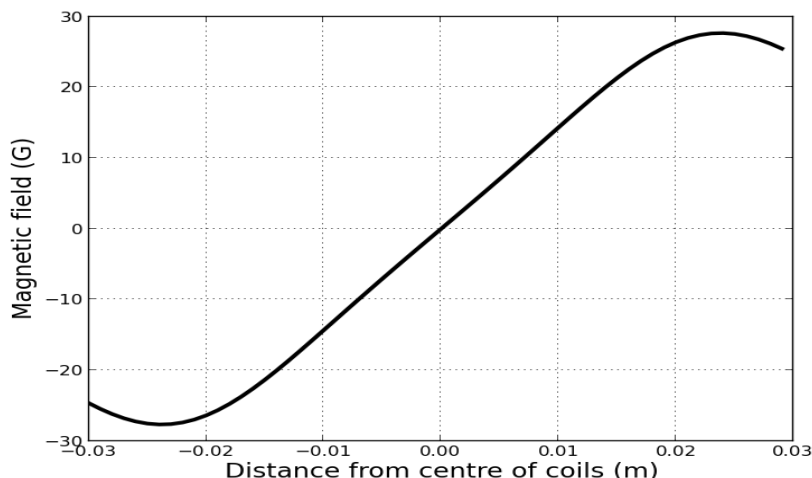


Figure 4.21: The magnetic field value between the coils for a current of 0.5 Am

For the same coils the calculated and measured magnetic gradients along the x-axis by CI Rigby [17] for $I = 0.5$ Ampere are 16.4 G/cm and 17.2 G/cm , respectively. While the calculated magnetic field gradient along the y-axis is 7.7 G/cm .

The calculated magnetic field gradient along the three axes (x, y, z) by M. Morrissey is roughly equal to that calculated by CI Rigby [17]. Our calculation of the field gradient along the x-axis is in agreement with that of M. Morrissey and CI Rigby.

Although the magnetic field gradient is enough to create MOT as shown by M. Morrissey in [7], the difference in the field gradient along the x-axis will affect the MOT shape by making it more compact from both side of the trapping beams the axis.

4.6 Simulation of the cooling force

Figure 4.23 shows the simulation of the velocity dependent cooling force versus velocity. Equation (2.2.4) was used in the simulation code for the following values of the parameters $\Gamma = 6 \text{ MHz}$ for the ^{87}Rb , $k = 2\pi/\lambda$, where $\lambda = 780 \text{ nm}$ for D_2 line in ^{87}Rb , $I_s = 1.6 \text{ mW/cm}^2$ saturation intensity of the ^{87}Rb [9], and $I = 15 \text{ mW/cm}^2$ the average intensity of one trapping beam in our experiment. F_- is for k in negative direction, and F_+ is for the k in the positive direction with respect to the direction of the atom velocity. The solid curve is the net force. As one can see in Figure 4.23, when the velocity is in the positive direction the maximum values of the net force is in the negative direction and vice versa, this confirms that the cooling force always in the opposite direction to the velocity. The position of the cooling force peaks depend on the detuning value of the laser frequency from the resonance Δ . Figure 4.23(a) show the cooling force curve at $\Delta = -0.5\Gamma$, Figure 4.23(b) at $\Delta = -\Gamma$, 4.23(c) at $\Delta = -1.5\Gamma$, and Figure 4.23(d) at $\Delta = -2\Gamma$.

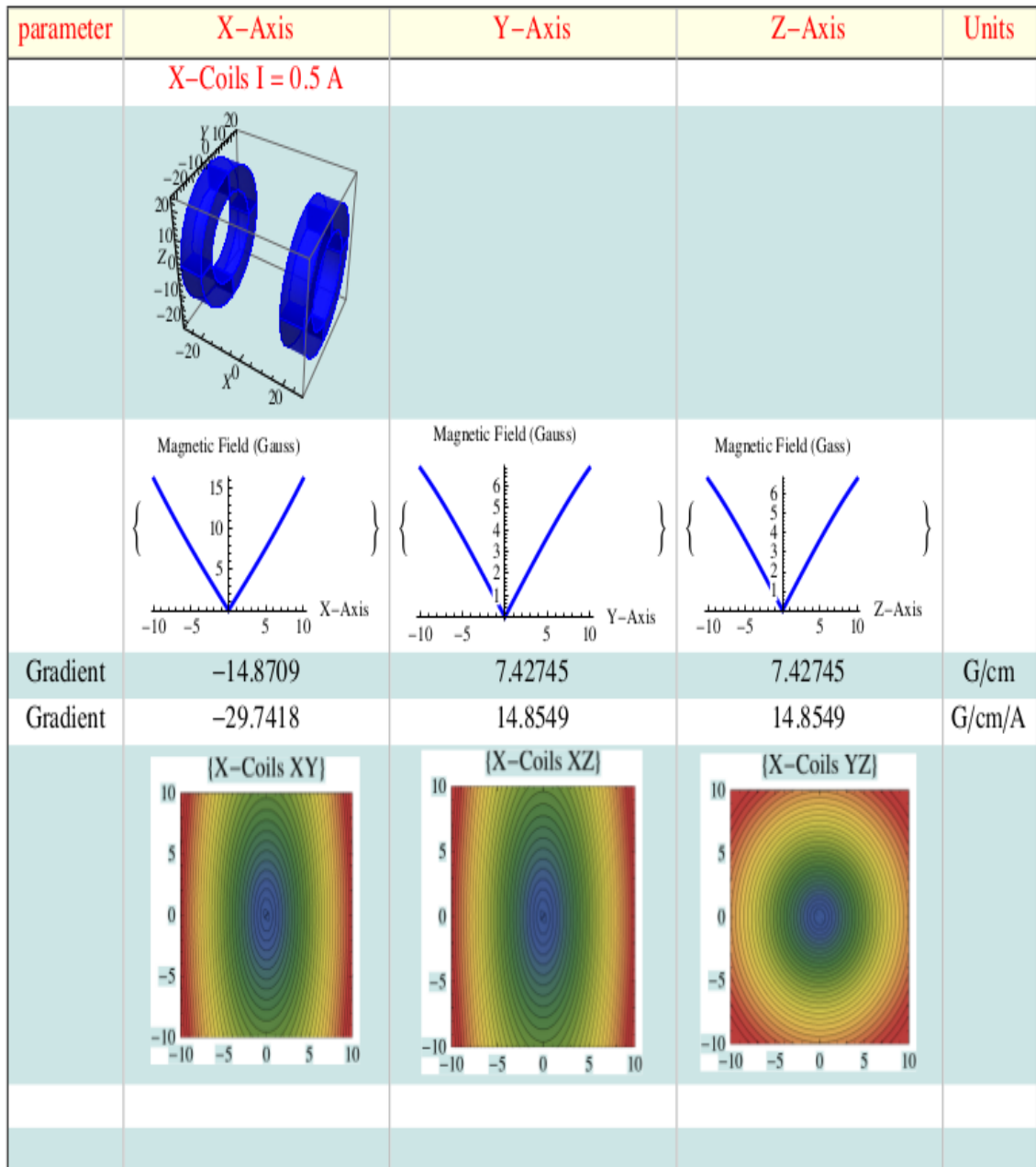


Figure 4.22: Result in the magnetic field. It has been done by M. Morrissey using Radia Software.

Figure 4.23(a) shows that when the detuning Δ is small the net cooling force will also have small value. Although in Figure 4.23(d) the cooling force has a large value compared to the other three graphs, but it shows that the cooling force for a large detuning Δ can have very small values in the low velocity range near to zero. As a result this will not be efficient for cooling and trapping. Therefore at $\Delta = -1.5\Gamma$ and $\Delta = -\Gamma$ detuning values as in Figures 4.23(b) and 4.23(c) the most efficient cooling force can be achieved.

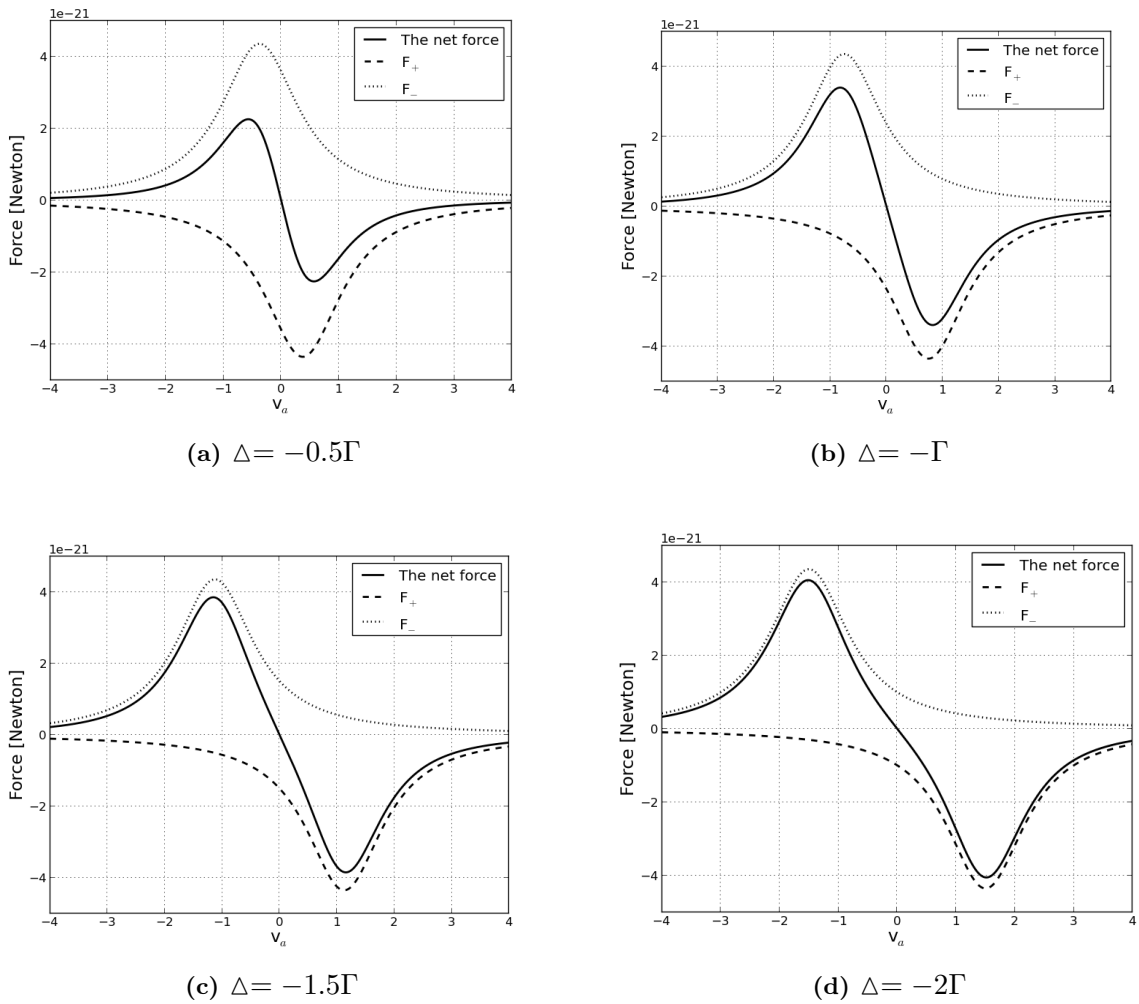


Figure 4.23: Cooling force versus velocity of atom in one-dimension, choose + direction for v_a . F_- is for \vec{k} in - direction, F_+ is for \vec{k} in + direction. The solid line is the net force \vec{F} .

4.7 Simulation of the trapping force

Figure 4.24 shows the simulation of the trapping force versus the detuning of the frequency Δ_z due to Zeeman effect. Equation (2.3.2) was used in the simulation code for $v_a = 0$, the other parameters have the same values as in section 4.6. Figure 4.24(a) is when the intensities I_1 and I_2 have the same value 15 mW/cm^2 , while Figure 4.24(b) is for $I_1 = 15 \text{ mW/cm}^2$ and $I_2 = 10 \text{ mW/cm}^2$. These intensity values are approximately the same values that were measured in our experimental setup. The F_- curve is for the beam that coming from the negative z -direction, F_+ curve is the beam that coming from the positive z -direction and the solid curve is the net force. As appeared in Figure 4.24 the net force has a positive value in the negative z -direction and has negative value in the positive z -direction. This confirm that the trapping forces from both sides of the z -axis are pointing toward the centre where the magnetic field $B = 0$.

Figure 4.24(a) shows that the trapping forces from the two sides of z -axis can have the same value

when the two counter-propagating trapping beams have equal intensity. But for the unbalanced trapping beams intensity, the trapping forces will be asymmetric as shown in Figure 4.24(b). Consequently, the zero-point of the net trapping force is not at $z = 0$ (where $B = 0$), but at $z = -4$ mm and this will shift the centre of mass of the final MOT.

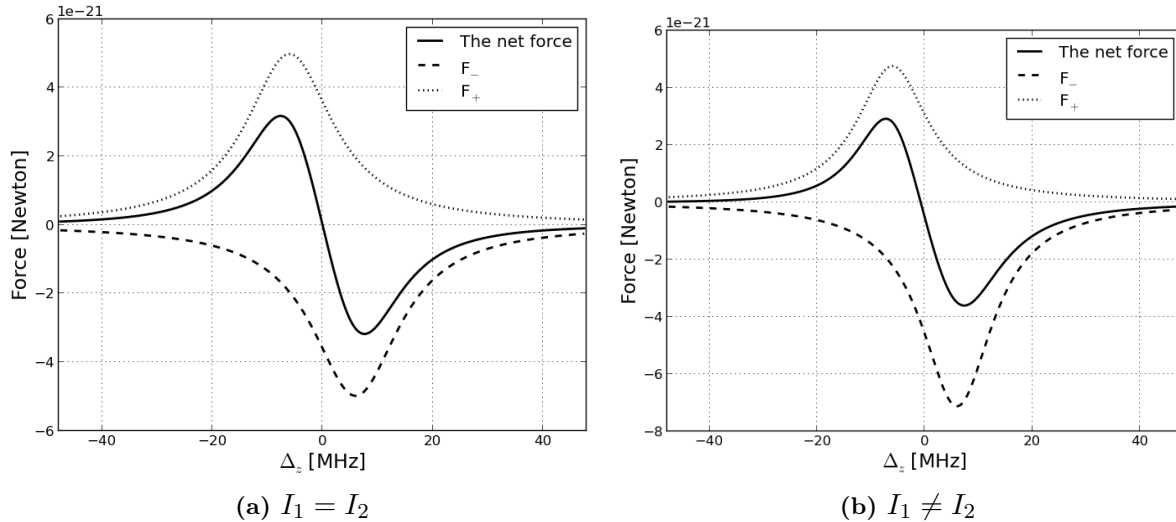


Figure 4.24: Trapping force versus the detuning of the frequency Δ_z due to Zeeman effect, of atom in one-dimension. F_- is for the coming from the positive z -direction, F_+ is for the beam coming from the negative z -direction. The solid line is the net force \vec{F} .

4.8 Procedure to achieve magneto optical trapping

To demonstrate a MOT one must be assured that all optics of the main MOT setup and the two SAS experiments are well aligned. The magnetic field coils are positioned on their place and the current directions are specified. The QWP axes are adjusted at the correct angles with regard to magnetic field vector directions. The power of the six trapping beams is adjusted. The imaging and measurement systems are positioned. At this stage the below procedure can be followed in order to see the trapped atoms:

- 1- Obtain the ultra-high vacuum pressure 10^{-9} mbar in the trapping cell (see Appendix 7).
- 2- Find the low operating current of the dispenser (see section 4.8.1).
- 3- Replace the expansion optics, which have been removed for the previous procedure.
- 4- Lock the frequencies of the lasers.
- 5- Introduce rubidium atoms inside the cell by switching on the current source of the dispenser. Adjust the current to the operating current.

- 6- Turn on the current source of the magnetic coils.
- 7- Trapped atoms should appear as a faint spot that is brighter than the background in the centre of the cell. Use the CMOS camera to observe them.

4.8.1 How to find the operating current of the dispenser

The operating current is the current at which the dispenser emits rubidium atoms at a slow rate, building up a low rubidium pressure so that a weak fluorescence can be seen by CMOS camera along the beam paths of the trapping beams as shown in Figure 4.25. During this procedure the expansion optics in the trapping beams were removed in order to see the fluorescence from the trapping beams easily. The procedure is suitable when using Rb dispensers type RB/NF/3.4/12 FT10+10 from SAES Group

- 1- Obtain the ultra-high vacuum pressure $\leq 10^{-8}$ mbar in the trapping cell.
- 2- Send 8 Ampere current to the dispenser for a period of 10 – 15 sec. This current is to heat up the dispenser and expand the slit of the dispenser.
- 3- Sent a high current to the dispenser for a short periods about 5 second several times. This high current makes the dispenser release all the contaminants that may be present on the dispenser into the cell where the ion pump will take them away. This process is call burn-in the dispenser.
- 4- Find the low operating current of the dispenser by sending 2 Ampere current to the dispenser and observe the trapping beams fluorescence using the CMOS camera. If fluorescence cannot be seen after waiting 20 seconds, the current can be increased by 0.5 Ampere. Repeat the step until weak stable rubidium fluorescence is seen.

4.8.2 Status of the magneto optical trapping experiment

So far trapped rubidium atoms in the MOT have not been realised. However, some important tasks in the experiment have been achieved. For example, circularly polarised trapping beams have been formed, locking of the laser frequencies has been done, the expansion optics have been aligned, the magnetic coils are operational and the CMOS camera has been used to image the fluorescence.

There are some challenges we have faced during the development of the experiment. These include; the development of the leaks in the vacuum system during bake-out, getting low Rb pressures in the cell using the dispenser, locking the laser frequencies in case of external vibrations.

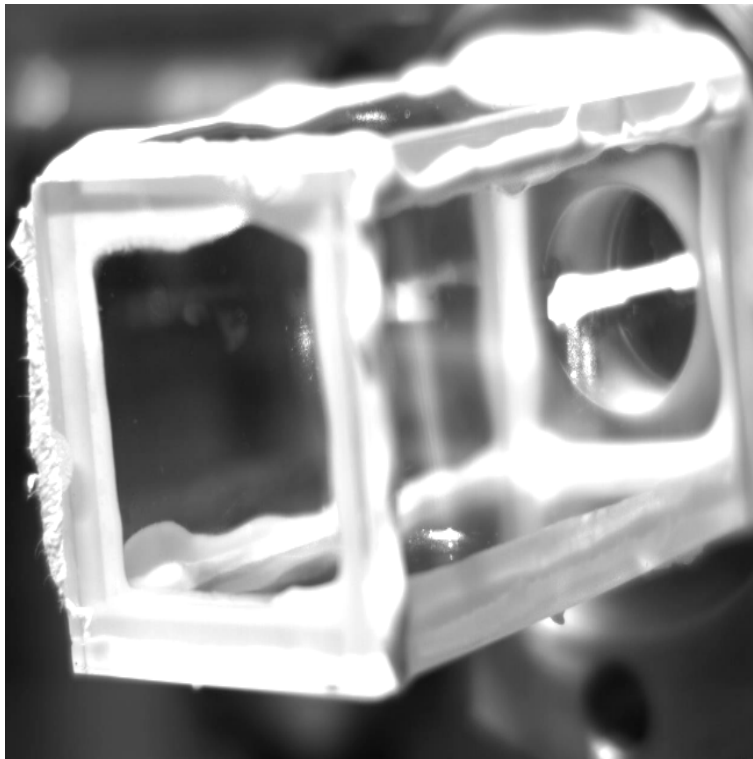


Figure 4.25: Rubidium fluorescences from the trapping beams.

Chapter 5

Conclusions and future work

5.1 Summary and Conclusions

In this study, the principles of laser cooling and magneto optical trapping of ^{87}Rb has been reviewed. It was shown from basic theory that the type of circular polarisation of the trapping beams (clockwise or counter clockwise) required for magneto optical trapping only depends on the relative direction of the magnetic field along the relative axis (outward pointing magnetic field requiring ccw polarisation and vice versa). This information was not available from the literature. The influence of trapping parameters on the number of trapped atoms has been investigated by a literature study. The investigation showed that, the trapped atoms in the MOT are sensitive to the following parameters; rubidium atom background vapour pressure, trapping beam sizes and power. However, the trapped atoms are less sensitive to some factors such as magnetic field gradient, trapping beam polarisation and alignment.

On the experimental point of view, we have contributed to the development of the MOT experiment that was started by G.N. Botha [26] and C.I. Rigby [17]. The existing two Vortex ECDL lasers in [17] were re-characterised. The effect of the vibrations on the lasers was reduced by new designed mounts. The laser with more power was used as the trapping laser from which the optical molasses was formed. The other laser is used for the repumping process. The beam expansion system for both laser beams, two optical test setups and two new setups for saturated absorption spectroscopy (SAS) of rubidium atoms were designed. Circular polarisation of the trapping beams was induced and optimised experimentally by using the two test setups. The rubidium dispensers as source of rubidium atoms was moved to a position inside the trapping cell, its opening facing in the direction of the centre of the cell. The two magnetic coils manufactured by Charles Rigby [17] in the Anti-Helmholtz coil configuration, was characterised by comparison of new calculation with values of the magnetic field measured previously. It was verified that adequate magnetic field gradient for demonstrating the magneto optical trapping process was achieved.

High resolution Doppler-free saturated absorption spectra of both ^{87}Rb and ^{85}Rb isotopes were measured using different setups. Using the newly developed SAS setups where the counter propagating pump and probe beams are truly collinearly aligned SAS spectra with narrower peaks than measured before in this lab have been obtained. The higher spectral resolution made it possible for the first time to resolve the hyperfine structure of the $5^2\text{S}_{1/2}$ $F = 2$ transition of ^{85}Rb . The signals of the spectrum were used in the side-lock servo systems (built by [26] and [17]) to lock the frequencies of the lasers for trapping and repumping transition in ^{87}Rb .

We successfully formed an optical molasses from three pairs of roughly equal power laser beams. The intersection point of the molasses beams is at the center of the trapping cell. The result of the optical setup tests showed that well optimised clock and counter-clock wise circularly polarised trapping beams were generated. The measurements were combined with the theory to ensure that the circular polarisation of every beam was correct. The fluorescence of the rubidium atoms in the trapping cell was observed. The fluorescence provides evidence that enough rubidium atoms were released from the dispenser in the trapping cell, and at the same time the frequency of the trapping laser remained locked to the chosen transition.

Appreciable experimental knowledge on the magneto optical trapping experiment was attained besides the research experience in the study. The MOT experiment was successfully developed up to the stage where it can be attempt magneto optical trapping. Adequate ultra-high vacuum pressure that is required for trapping has not been obtained. This is arguably because of small leaks that develop during bake-out of the system and are difficult to locate. In addition, our ion vacuum pump is small which makes it extremely difficult to achieve the desirable pressure for the trapping process. Therefore, cold trapped ^{87}Rb atoms were not successfully demonstrated. Consequently, the influence of the trapping parameters on the number of the trapped atoms was not studied experimentally.

5.2 Recommendations for future work

In the future, we suggest that the entire vacuum system should be enlarged. As a result, the trapping beam sizes can also be expanded. In this case, the rubidium dispenser can be positioned further away from the beam, and hence the beams will not be clipped by the tip of the dispenser. An ion pump with larger pumping capacity will be needed. A different source of Rb should be used that does not need frequent replacement of the rubidium dispensers, as each replacement means opening the vacuum system to air. With this expansion, one can obtain large numbers of cold trapped atoms in the MOT system, which can be used as cold atomic sample for further studies. It can also be interesting to design a temperature measuring technique and be added to the experiment so that one can determine the temperature of the trapped atoms. Hopefully these suggestions and recommendations can solve the present challenges and lead to the goal of the main project, which in turn will be a considerable contribution to the achievements of the Laser Research Institute at Stellenbosch University.

Chapter 6

Appendix A

6.1 Derivation of the polarization of the trapping beams from the first principles

If we consider a simple atom with spin angular momentum \vec{S} and orbital angular momentum \vec{L} , then the total electron angular momentum \vec{J} , is given as

$$\vec{J} = \vec{S} + \vec{L}$$

The magnitude J and the z-component J_z of \vec{J} are specified by j and m_j quantum numbers, according to the usual quantization conditions [33] as follow

$$J = \sqrt{j(j+1)}\hbar$$

$$J_z = m_j\hbar$$

with m_j taking the following possible values

$$-j, -j+1, 0, j-1, +j.$$

The relation between the total angular momentum and its magnetic dipole moment is [33]

$$\vec{\mu}_j = \frac{-g_j\mu_B\vec{J}}{\hbar}$$

$$\vec{\mu} \cdot \hat{z} = \mu_{j_z} = -g_j\mu_B m_j$$

where g_j is called the Landé factor, and $\mu_B = \frac{e\hbar}{2m}$ is the Bohr magneto.

Considering a hypothetical atom with $J=0$ ($m_j=0$) for the ground level, and $J=1$ ($m_j = -1, 0, +1$) on the excited state. In the presence of a weak inhomogeneous magnetic field, these magnetic sub-levels will be split with an energy shift of according to the Zeeman effect as shown in Figure 6.1. Our interest is in the transition caused by σ^+ and σ^- polarised light.

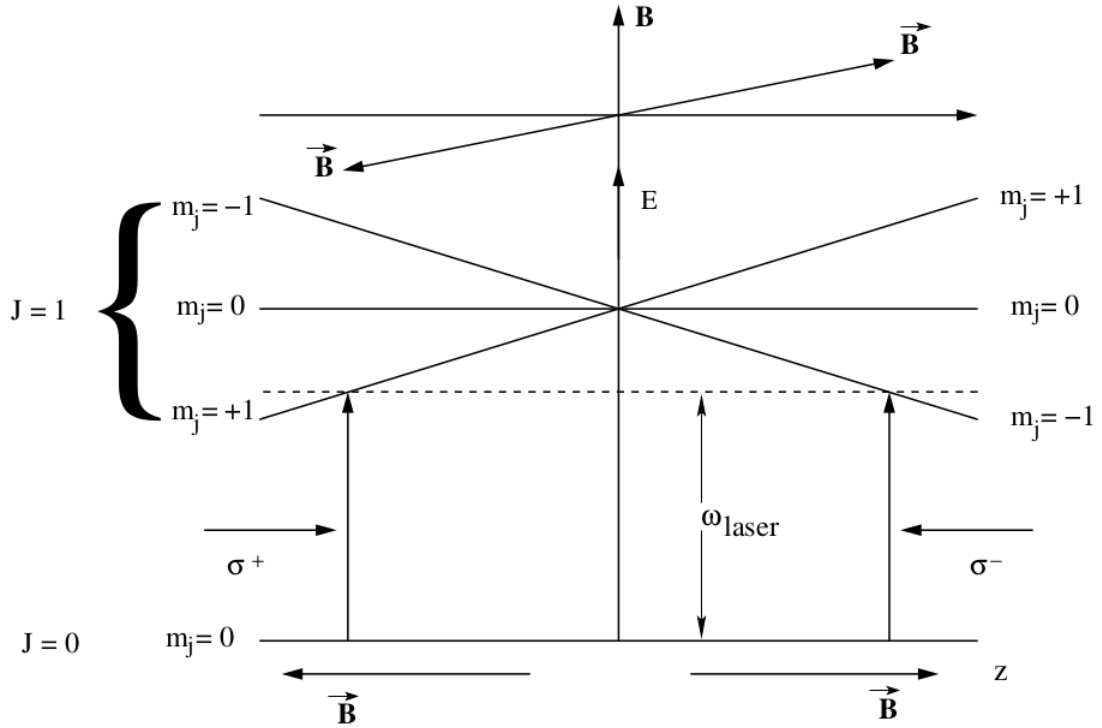


Figure 6.1: Illustration of the trapping by circular polarised light and the split of the J level of the excited state in the presence of an external magnetic field.

When the magnetic field B is zero at the (0) point in the origin of z -axis and increasing linearly in the opposite direction along the positive and negative z -axis respectively, then on the R.H.S where \vec{B} is in the $+\hat{z}$ -direction we can derive the expression for the shift in energy due to the Zeeman effect as follows

$$\begin{aligned}
 U &= -\vec{\mu} \cdot \vec{B} \\
 &= -\vec{\mu} \cdot (|\vec{B}|\hat{z}) \\
 &= -\vec{\mu} \cdot \hat{z}|\vec{B}| \\
 &= -|\vec{B}|\mu_{jz} \\
 &= -|\vec{B}|(-g_j\mu_B m_j) \\
 &= |\vec{B}|(g_j\mu_B m_j) \begin{cases} > 0 & \text{for } m_j = +1 \\ = 0 & \text{for } m_j = 0 \\ < 0 & \text{for } m_j = -1 \end{cases} \quad (6.1.1)
 \end{aligned}$$

On the L.H.S where \vec{B} is in the $-\hat{z}$ direction we can derive the following equations

$$\begin{aligned}
 U &= -\vec{\mu} \cdot \vec{B} \\
 &= -\vec{\mu} \cdot (-|\vec{B}|\hat{z}) \\
 &= \vec{\mu} \cdot \hat{z}|\vec{B}| \\
 &= |\vec{B}|\mu_{jz} \\
 &= |\vec{B}|(-g_j\mu_B m_j) \\
 &= -|\vec{B}|(g_j\mu_B m_j) \begin{cases} > 0 & \text{for } m_j = -1 \\ = 0 & \text{for } m_j = 0 \\ < 0 & \text{for } m_j = +1 \end{cases} \quad (6.1.2)
 \end{aligned}$$

As shown in the equations (6.1.1) and (6.1.2), the magnetic sub-level $m_j = -1$ and $m_j = +1$ in the excited state are in the lowest energy level on the R.H.S and L.H.S respectively. The transitions to lower levels are more likely than to the higher energy levels with red-tuned laser. Our goal is to achieve a position dependent trapping force toward the center. Hence, we must illuminate the atoms from the R.H.S by σ^- polarized light, and from the L.H.S by σ^+ polarised as shown in Figure 6.1.

The σ^+ polarised light is defined as the light possessing the angular momentum that is required to drive a transition with $\Delta m_j = +1$, whereas σ^- is the light possessing angular momentum that is required for a transitions with $\Delta m_j = -1$ [5]. Here, $\Delta m_j = m'_j - m_j$, where m'_j and m_j are the quantum number of the excited and ground states respectively.

The following method was used to show the association of the σ^- and σ^+ with cw or ccw circularly polarized light.

- Direction of \vec{B} relative to \vec{z} determine which m_j value has lowest energy.
- m_j with lowest energy determine whether σ^+ or σ^- is required.
- From the angular momentum vectors associated with m_j values the angular momentum Ω of the σ^- or σ^+ photon can be determine as shown in Figure 6.2.
- The direction of the Ω , together with the direction of \vec{k} give cw or ccw circularly polarised light.

Figure 6.3 shows the association of the σ^- and σ^+ with cw or ccw circularly polarized light depends on the relative direction of the wave vector \vec{k} and \hat{z} .

The result is that if the \vec{B} fields are pointing outwards from the centre, the trapping beams along that axis must be ccw circular polarised. If the \vec{B} fields are pointing inwards towards the centre, the trapping beams must be cw circular polarised.

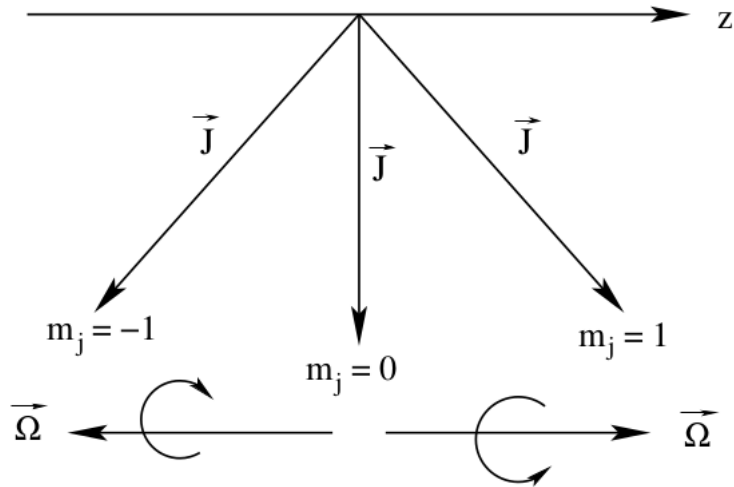


Figure 6.2: Illustration of the association of the angular momentum vectors with m_j values. This association is independent from the direction of the external magnetic field.

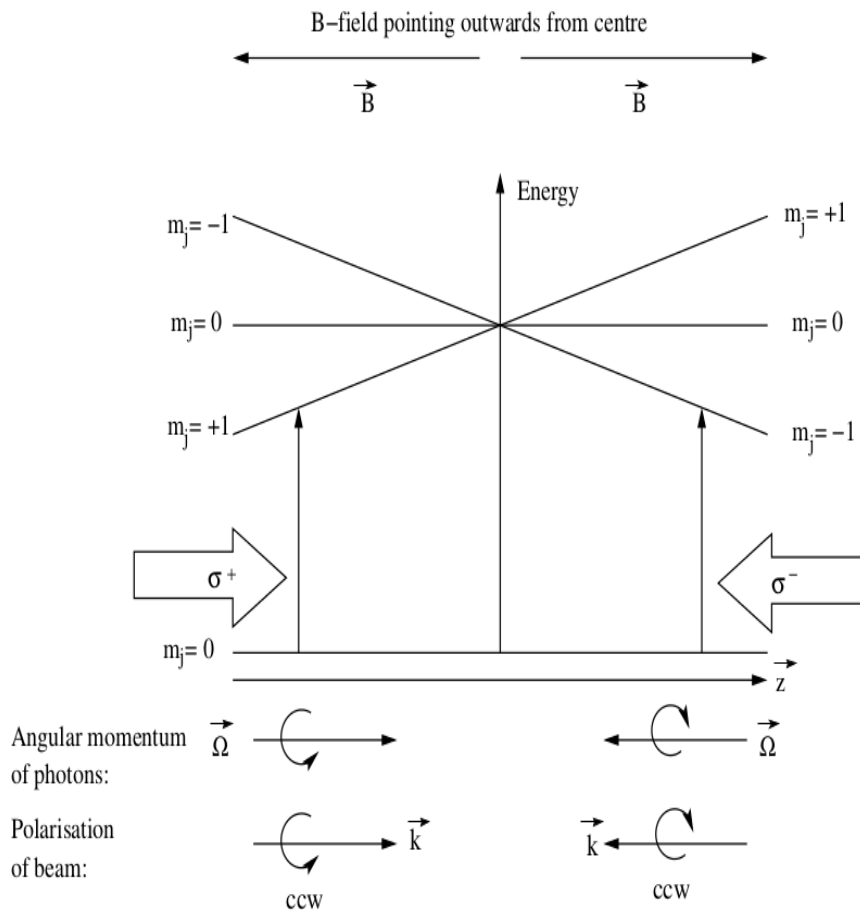


Figure 6.3: Illustration of the association of σ^- and σ^+ transitions with the cw and ccw circular polarised light.

Chapter 7

Appendix B

7.1 Operation of the Vacuum System

- 1– After we ensure that all flanges are properly connected, the three valves (rubber angle, gate valve, and metal seal valve) are opened, and the vacuum gauge is turned on. The roughing pump is also turned on to begin the evacuation.
- 2– After few minutes or when the pressure has dropped to 2×10^{-2} mbar, the turbo pump is turned on.
- 3– After 24 hours the pressure on the gauge is about 10^{-6} mbar. At this point of pressure the vacuum system is tested for leak, by spreading ethanol onto the points of the chamber surface where the leak can occur, and also checking the readings on the vacuum gauge if there has been a change in the pressure. If no change in the pressure is read, then this means that there is no leak.

The entire system is heated up to 120 C° for a few days, while the turbo and roughing pumps are left running in order to evaporate and remove the contaminants, such as water and other gases. The higher the temperature and the longer the bake-out, the lower the pressure can be achieved. But the melting point of the vacuum epoxy determines the maximum temperature of the process [7].

To end bake-out close metal angle valve to separate ultra high vacuum part from turbo pump. Switch off turbo and roughing pumps and turn on the ion pump.

- 4– After few hours when the pressure on the ion pump controller is about 1×10^{-7} mbar, and the ion pump is running properly, switch off heating. The pressure on the ion pump controller is known by reading the current on it, and comparing it with its corresponding vacuum level on the graph provided on a paper by the ion pump manufacturers.

Chapter 8

Appendix C

8.1 Jones Matrices of Polariser

When a polarised light beam described its Jones vector E_i passes through an optical element, the emerging beam will have a different polarisation represents by its new Jones vector E_t . This is because the optical element has transformed the polarisation of the beam from E_i to E_t . And each an optical element has its 2×2 Jones transformation Matrix [32].

The Jones vector that describes the emerging beam polarisation is given by the product of the Jones matrix of the optical element and the Jones vector that represent the polarisation of the incident light, as shown in Equation (8.1.1)

$$E_t = ME_i \quad (8.1.1)$$

where E_i and E_t are Jones vectors that describe the polarisation of the incident and emerging beams, respectively. And M is the transformation matrix of the optical element.

The transformation matrices of some optical elements are shown in Table 8.1 [32]. When the

Table 8.1: Jones transformation matrices of the half and quarter wave plates

Optical element	Jones matrix	Source
Half-wave plate, fast or slow axis vertical	$\begin{bmatrix} 1 & 0 \\ 0 & -1 \end{bmatrix}$	[32]
Quarter-wave plate, fast axis vertical, slow axis horizontal	$e^{i\pi/4} \begin{bmatrix} 1 & 0 \\ 0 & -i \end{bmatrix}$	[32]
Quarter-wave plate, fast axis horizontal, slow axis vertical	$e^{i\pi/4} \begin{bmatrix} 1 & 0 \\ 0 & i \end{bmatrix}$	[32]

optical element is rotated by an angle θ counter-clockwise relative to the horizontal axis the new

transformation matrix of the element is given as

$$A(\theta) = R(\theta)MR(-\theta) \quad (8.1.2)$$

where

$$R(\theta) = \begin{bmatrix} \cos(\theta) & -\sin(\theta) \\ \sin(\theta) & \cos(\theta) \end{bmatrix} \quad (8.1.3)$$

Using Equation (8.1.3) and the corresponding Jones matrix of the half-wave plate in Table 8.1, the transformation matrix of the half-wave plate rotated by an angle θ relative to the horizontal axis, can be found as

$$M_{\text{HWP}}(\theta) = \begin{bmatrix} \cos(2\theta) & \sin(2\theta) \\ \sin(2\theta) & -\cos(2\theta) \end{bmatrix} \quad (8.1.4)$$

And similarly for the quarter-wave plate with fast axis vertical (slow axis horizontal) rotated by θ ccw relative to horizontal

$$M_{\text{QWP}}(\theta) = \begin{bmatrix} \cos^2 \theta - i \sin^2 \theta & \cos \theta \sin \theta (1 + i) \\ \cos \theta \sin \theta (1 + i) & -i \cos^2 \theta + \sin^2 \theta \end{bmatrix}. \quad (8.1.5)$$

Chapter 9

Appendix D

Table 9.1 shows the relative frequency of the Doppler-Broadened absorption spectrum peaks of the Rb atoms. The is given by the author in [30]

Table 9.1: The relative frequency of the Doppler-Broadened absorption spectrum peaks of Rb atoms

Peak	Relative frequency /GHz
^{87}Rb F = 2	0
^{85}Rb F = 3	1.48
^{85}Rb F = 2	4.49
^{87}Rb F = 1	6.76

Table 9.2 shows the hyperfine levels energy shift in the ground and excited levels of the D₂ line in ^{85}Rb , the data are given by the author in [34].

Table 9.2: The energy shift of the hyperfine levels of the ground and excited levels of the D₂ transition in ^{85}Rb .

Fine level	Hyperfine level	Energy shift /MHz
$5^2\text{S}_{1/2}$	F = 2	-1770.8439228(35)
	F = 3	1264.8885163(25)
$5^2\text{P}_{3/2}$	F' = 1	-113.208(84)
	F' = 2	-83.835(34)
	F' = 3	-020.435(51)
	F' = 4	100.205(44)

Chapter 10

AppendixE

The program in this appendix was created by Dr. M. Morrissey using Radia software, in which the input parameters were the dimensions of the magnetic coils used in this thesis. The code is reproduced with his permission.

```
(Debug) In[209]:= << Radia` ;                (* Load Radia package *)
                RadUtiMem[];

Wrong Version of Radia.exe

Radia is copyright ESRF, France.

Portions copyright Synchrotron SOLEIL, France.

Portions copyright Wolfram Research, Inc.
```

Program Parameters;

```
D2Plots = 1; (*0 = do not calculate 2D plot data.... 1 = plot 2d plots*)
(*it takes time to generate data for teh
lots so programs runs much faster without 2D plots*)

(*these are teh plting settings*)
PlotLimits = 10;
PlotResolution = .1;
ContLin = 30;
ContourPoints = 40;
ContourRes = 0.5;
```

Input Coil Parameters;

```
(*The dimensions of the wire coil *)

ICoil = 0.5; (* A *)

InnerDiam = 30; (* mm *)
RadWidth = 8;
AxWidth = 10; (* mm *)
CoilSeparationS = 26; (*S = separation of coils from Surface-to-Surface*)

WireDiam = 0.6; (* mm *)
EnamelThickness = 0.1;

WallThick = 5;
```

geometrical & Electrical calculations;

```
OuterDiam = InnerDiam + RadWidth * 2 ;

CoilSeparationC = CoilSeparationS + AxWidth + 2 * WallThick;
(*separation centre → centre*)

PackRatio = 3.14 / 4; (* Takes into account the empty space left by wire*)
WireCrossSect = 3.14 * ((WireDiam) / 2) ^ 2;
CuCrossSect = 3.14 * ((WireDiam - EnamelThickness) / 2) ^ 2;
(*wire cross section minus the enamel layer mm *)

CuDensity = 8.96 * 10^3 ; (*density of copper Kg/m^3*)
CuResistivity = 1.68 * 10^-8; (*Ohm meter*)
CuSHC = 0.39; (*(kJ/kg K)*)

AxLayers = AxWidth / WireDiam;
RadLayers = RadWidth / WireDiam;
NumLoops = AxLayers * RadLayers;
DiamAve = InnerDiam + RadWidth;
PerimAve = 2 * 3.14 * (DiamAve / 2);
WireLengthTot = NumLoops * PerimAve;
WireVol = WireLengthTot * WireCrossSect;
CuVol = WireLengthTot * CuCrossSect;
CoilMass = CuVol * CuDensity;
```

```

ICoilDensity = PackRatio * ICoil / WireCrossSect;

DSRatio = DiamAve * CoilSeparationC^-1;
(*XCoilResistance = CuResistivity*(XWireLengthTot*10^-3)/(10^-6*XCuCrossSect);*)
CoilPairResistance = 2 * CuResistivity * (WireLengthTot * 10^-3) / (10^-6 * CuCrossSect);

ICoilPair = ICoil;
CoilPairVoltage = ICoil * CoilPairResistance;
CoilPairPower = ICoilPair^2 * CoilPairResistance;
AmpereWindings = ICoil * NumLoops;
ICoilDensity = PackRatio * ICoil / WireCrossSect; (*Current density A/mm^2 *)

```

Define Coils;

```

Coil1 = radObjRaceTrk[{0, 0, (CoilSeparationC) / 2},
  {InnerDiam / 2, OuterDiam / 2}, {0, 0}, {AxWidth, 100, -ICoilDensity};
Coil2 = radObjRaceTrk[{0, 0, -(CoilSeparationC) / 2},
  {InnerDiam / 2, OuterDiam / 2}, {0, 0}, {AxWidth, 100, ICoilDensity};

(*Set coils rotation axis and angle*)
coiltransformx = radTrfRot[{0, 0, 0}, {0, 1, 0}, -π / 2];
coiltransformy = radTrfRot[{0, 0, 0}, {1, 0, 0}, -π / 2];

(*Rotate the coils According to the above rotation*)
Coil1 = radTrfOrnt[Coil1, coiltransformx];
Coil2 = radTrfOrnt[Coil2, coiltransformx];

(*Group all the coils together*)
Group = radObjCnt[{Coil1, Coil2}];
(* Group the X coils and the Y coils separately*)

radObjDrwAtr[Coil1, {0, 0, 1}, 0.001];
radObjDrwAtr[Coil2, {0, 0, 1}, 0.001];

DrawCoils = radObjDrw[Group];
CoilsDraw = Show[Graphics3D[DrawCoils, Axes → True, AxesLabel → {X, Y, Z}]];

```

Magnetic field;

```

CoilPlotX = {ListLinePlot[Table[{x, 10000
  Norm[radFld[Group,
    "b", {x, 0, 0}]]}, {x, -PlotLimits, PlotLimits, PlotResolution}],
  PlotStyle → {Blue, Thick}, Axes → True,
  AxesLabel → {"X-Axis", "Magnetic Field (Gauss)"}, AxesOrigin → {0, 0}]];

CoilPlotY = {ListLinePlot[Table[{y, 10000
  Norm[radFld[Group, "b", {0, y, 0}]]}, {y, -PlotLimits, PlotLimits, PlotResolution}],
  PlotStyle → {Blue, Thick}, Axes → True,
  AxesLabel → {"Y-Axis", "Magnetic Field (Gauss)"}, AxesOrigin → {0, 0}]];

CoilPlotZ = {ListLinePlot[Table[{z, 10000
  Norm[radFld[Group, "b", {0, 0, z}]]}, {z, -PlotLimits, PlotLimits, PlotResolution}],
  PlotStyle → {Blue, Thick}, Axes → True,
  AxesLabel → {"Z-Axis", "Magnetic Field (Gauss)"}, AxesOrigin → {0, 0}]];

(*=====
*)

Xx = Table[{x, radFld[Group, "bx", {x, 0, 0}]}], {x, -1, 1, 0.01}];
XfitFuncx = Fit[Xx, {1, x, x^2}, x];

```

```

Gradx = 105 Extract[XfitFuncx, {2, 1}];

Xy = Table[{y, radFld[Group, "by", {0, y, 0}]}, {y, -1, 1, 0.01}];
XfitFuncy = Fit[Xy, {1, y, y2}, y];
Grady = 105 Extract[XfitFuncy, {2, 1}];

Xz = Table[{z, radFld[Group, "bz", {0, 0, z}]}, {z, -1, 1, 0.01}];
XfitFuncz = Fit[Xz, {1, z, z2}, z];
Gradz = 105 Extract[XfitFuncz, {2, 1}];

GradxA = Gradx / (ICoil);
GradyA = Grady / (ICoil);
GradzA = Gradz / (ICoil);

```

Plots;

```

If[D2Plots == 1,
  TableXY =
    Flatten[Table[{x, y, 10 000 * Norm[radFld[Group, "b", {x, y, 0}]}], {x, -PlotLimits,
      PlotLimits, ContourRes}, {y, -PlotLimits, PlotLimits, ContourRes}], 1];

  CoilPlotXY = ListContourPlot[TableXY, ColorFunction -> "DarkRainbow",
    PlotLabel -> {"X-Coils XY"}, AxesLabel -> {"X-Axis", "Y-axis"}, Contours -> ContLin,
    PlotRange -> {{-PlotLimits, PlotLimits}, {-PlotLimits, PlotLimits}},
    MaxPlotPoints -> ContourPoints];

  TableXZ =
    Flatten[Table[{x, z, 10 000 * Norm[radFld[Group, "b", {x, 0, z}]}], {x, -PlotLimits,
      PlotLimits, ContourRes}, {z, -PlotLimits, PlotLimits, ContourRes}], 1];

  CoilPlotXZ = ListContourPlot[TableXZ, ColorFunction -> "DarkRainbow",
    PlotLabel -> {"X-Coils XZ"}, AxesLabel -> {"X-Axis", "Z-axis"}, Contours -> ContLin,
    PlotRange -> {{-PlotLimits, PlotLimits}, {-PlotLimits, PlotLimits}},
    MaxPlotPoints -> ContourPoints];

  TableYZ =
    Flatten[Table[{y, z, 10 000 * Norm[radFld[Group, "b", {0, y, z}]}], {y, -PlotLimits,
      PlotLimits, ContourRes}, {z, -PlotLimits, PlotLimits, ContourRes}], 1];

  CoilPlotYZ = ListContourPlot[TableYZ, ColorFunction -> "DarkRainbow",
    PlotLabel -> {"X-Coils YZ"}, AxesLabel -> {"Y-Axis", "Z-axis"}, Contours -> ContLin,
    PlotRange -> {{-PlotLimits, PlotLimits}, {-PlotLimits, PlotLimits}},
    MaxPlotPoints -> ContourPoints];

]

```

Print results;

```

Print[Style["===== ", 24, Red]];
WIRE;
WireTableData = {
  {"Shape", "Circular", "mm"},
  {"Diameter", WireDiam, "mm"},
  {"Enamel", EnamelThickness, "mm"},
  {"Wire Total CS ", WireCrossSect, "mm2"},
  {"Cu CS ", CuCrossSect, "mm2"},
  {"Packing Ratio", PackRatio, ""},
  {"Resistivity (Cu)", CuResistivity, "Ohm m"},
  {"Density (Cu)", CuDensity, "Kg/m3"},
  {"SHC (Cu)", CuSHC, "(kJ/kg K)"}
};

Print[Style["WIRE", 24, Red]]

```

```

Print[Style["Paramets of the wire used to make the coils", 14, Blue]];

Text@Grid[Prepend[WireTableData, {Style["Parameter", 14, Red],
  Style["X Value", 14, Red], Style["Units", 14, Red]}], Background →
  {None, {Lighter[Yellow, 0.9], {White, Lighter[Blend[{Blue, Green}], .8]}},
  Dividers → {{Darker[Gray, .6], {Lighter[Gray, .5]}, Darker[Gray, .6]},
  {Darker[Gray, .6], Darker[Gray, .6], {False}, Darker[Gray, .6]}}

Print[Style["MOT COIL", 24, Red]];
Print[Style["=====", 24, Red]];
Print[Style["Illustration of MOT coils", 14, Blue]];
Print[CoilsDraw];

Istr = ToString[ICoil];
IstrLable = StringJoin["I = ", Istr, " A"];
IstrLableX = StringJoin["Coils for ", IstrLable];

IstrLableMag = StringJoin["X-Coils ", IstrLable];

```

General Properties X;

```

MOTTableGen =
{
  {"Shape", "Circular"},
  {"Configuration", "Anti-Helmholtz"},
  {"Inner Diameter", InnerDiam, "mm"},
  {"Outer Diameter", OuterDiam, "mm"},
  {"Axial Thickness ", AxWidth, "mm"},
  {"Radial Thickness ", RadWidth, "mm"},
  {"Axial Layers", AxLayers},
  {"Radial Layers", RadLayers},
  {"Average Diameter", DiamAve, "mm"},
  {"Average Perimeter", PerimAve, "mm"},
  {"Loops", NumLoops, "/coil"},
  {"Lenght of Wire", WireLengthTot * 10^-3, "m/coil"},
  {"Total Volume", WireVol * 10^-3, "cm^3/coil"},
  {"Cu Volume", N[CuVol * 10^-3, 2], "cm^3/coil"},
  {"Mass", CoilMass * 10^-9, "kg/coil"},
  {"Separation (s-s)", CoilSeparationS, "mm"},
  {"Separation (c-c)", CoilSeparationC, "mm"},
  {"D/S Ratio", DSRatio, "mm"}
};

MOTTableGenPrint = Text@Grid[Prepend[MOTTableGen, {Style["Coil Parameter", 14, Red],
  Style["ue for Single Coil", 14, Red], Style["Units", 14, Red]}], Background →
  {None, {Lighter[Yellow, 0.9], {White, Lighter[Blend[{Blue, Green}], .8]}},
  Dividers → {{Darker[Gray, .6], {Lighter[Gray, .5]}, Darker[Gray, .6]},
  {Darker[Gray, .6], Darker[Gray, .6], {False}, Darker[Gray, .6]}}];

Print[MOTTableGenPrint];

(*=====*)

```

Electro Properties ;

```

MOTTableElectro =
{
  {"Current", ICoil, "Amps"},
  {"Resistance", CoilPairResistance, "Ohm"},
  {"Inductance", , "mH"},
  {"Current Density", ICoilDensity, "A/mm^2"},
  {"Voltage", CoilPairVoltage, "V"},
  {"Power", CoilPairPower, "W"}
};

```

```
MOTTableElectroPrint =
Text@Grid[Prepend[MOTTableElectro, {Style["X-Coil Parameter", 14, Red],
Style["Coil Pair", 14, Red], Style["Units", 14, Red]}], Background →
{None, {Lighter[Yellow, 0.9], {White, Lighter[Blend[{Blue, Green}], .8]}]},
Dividers → {{Darker[Gray, .6], {Lighter[Gray, .5]}, Darker[Gray, .6]},
{Darker[Gray, .6], Darker[Gray, .6], {False}, Darker[Gray, .6]}}];

Print[Style["Electrical Properties of the MOT Coils", 14, Blue]];
Print[MOTTableElectroPrint];
```

Magnetic Properties;

```
Print[Style["Magnetic Properties of the MOT Coils", 14, Blue]];
MOTTableMagnetic =
{
{"", Style[IStringLableMag, 14, Red], , , ""},
{"", CoilsDraw, , , ""},
{"", CoilPlotX, CoilPlotY, CoilPlotZ, ""},
{"Gradient", Gradx, Grady, Gradz, "G/cm"},
{"Gradient", GradxA, GradyA, GradzA, "G/cm/A"},
{"", CoilPlotXY, CoilPlotXZ, CoilPlotYZ, ""},
{"", , , , ""},
{"", , , , ""}
};

MOTTableMagneticPrint = Text@Grid[Prepend[MOTTableMagnetic,
{Style["parameter", 14, Red], Style["X-Axis", 14, Red], Style["Y-Axis", 14, Red],
Style["Z-Axis", 14, Red], Style["Units", 14, Red]}], Background →
{None, {Lighter[Yellow, 0.9], {White, Lighter[Blend[{Blue, Green}], .8]}]},
Dividers → {{Darker[Gray, .6], {Lighter[Gray, .5]}, Darker[Gray, .6]},
{Darker[Gray, .6], Darker[Gray, .6], {False}, Darker[Gray, .6]}}];
Print[MOTTableMagneticPrint]
```

=====

=====

WIRE

Params of the wire used to make the coils

Parameter	X Value	Units
Shape	Circular	mm
Diameter	0.6	mm
Enamel	0.1	mm
Wire Total CS	0.2826	mm ²
Cu CS	0.19625	mm ²
Packing Ratio	0.785	
Resistivity (Cu)	1.68 × 10 ⁻⁸	Ohm m
Density (Cu)	8960.	Kg/m ³
SHC (Cu)	0.39	(kJ/kg K)

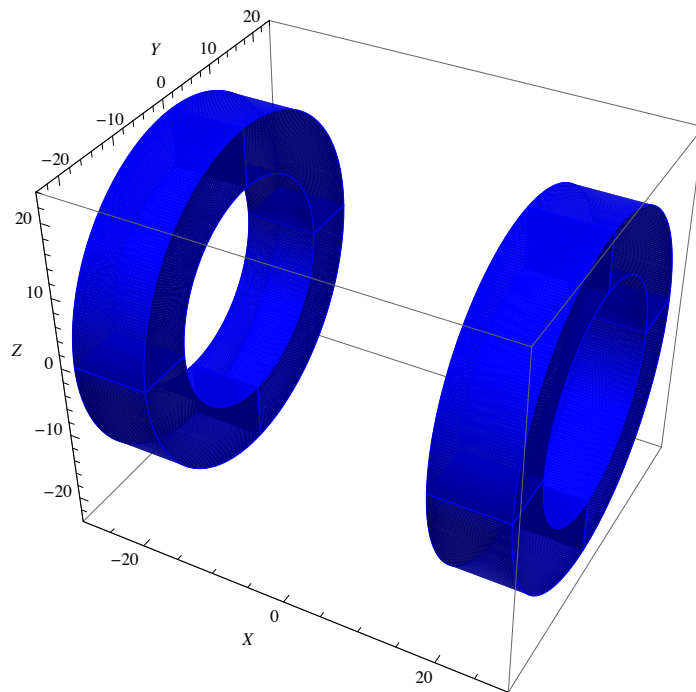
(Debug) Out[366]=

MOT COIL

=====

=====

Illustration of MOT coils

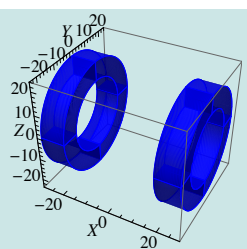
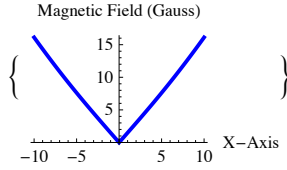
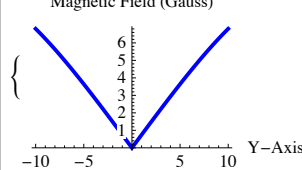
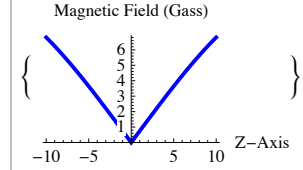
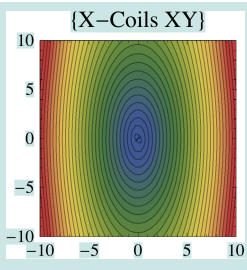
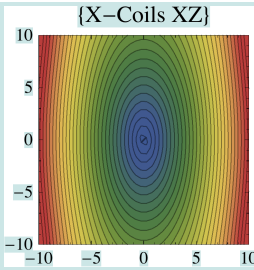
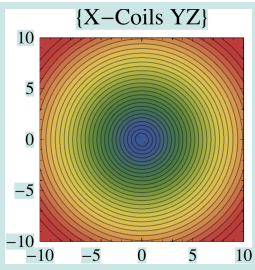


Coil Parameter	Value for Single Coil	Units
Shape	Circular	
Configuration	Anti-Helmholtz	
Inner Diameter	30	mm
Outer Diameter	46	mm
Axial Thickness	10	mm
Radial Thickness	8	mm
Axial Layers	16.6667	
Radial Layers	13.3333	
Average Diameter	38	mm
Average Perimeter	119.32	mm
Loops	222.222	/coil
Length of Wire	26.5156	m/coil
Total Volume	7.4933	cm ³ /coil
Cu Volume	5.20368	cm ³ /coil
Mass	0.046625	kg/coil
Separation (s-s)	26	mm
Separation (c-c)	46	mm
D/S Ratio	$\frac{19}{23}$	mm

Electrical Properties of the 2-D MOT Coils

X-Coil Parameter	Coil Pair	Units
Current	0.5	Amps
Resistance	4.53973	Ohm
Inductance		mH
Current Density	1.38889	A/mm ²
Voltage	2.26987	V
Power	1.13493	W

Magnetic Properties of the 2-D MOT Coils

parameter	X-Axis	Y-Axis	Z-Axis	Units
	X-Coils I = 0.5 A			
				
	Magnetic Field (Gauss) 	Magnetic Field (Gauss) 	Magnetic Field (Gauss) 	
Gradient	-14.8709	7.42745	7.42745	G/cm
Gradient	-29.7418	14.8549	14.8549	G/cm/A
	{X-Coils XY} 	{X-Coils XZ} 	{X-Coils YZ} 	

(Debug) Out[388]= Null'

(Debug) In[299]:= **CoilPairResistance**

(Debug) Out[299]= 4.53973

List of References

- [1] Philips, W.D.: Laser cooling and trapping of neutral atoms. Nobel lecture, National Institute of Standards and Technology, Physics Laboratory, Atomic Physics Division, Gaithersburg MD 20899, USA, December 1997.
- [2] Jain-hua, G., Yi-min, Xu-zong, Hai-feng, L. and Yi-qiu, Y.: Magneto-optical trap of cesium atoms. *Chin.phys.lett*, vol. 13, no. 11, pp. 821–824, 1996.
- [3] Tung, S.-K., Chen, Y.-C., Lin, C.-W., Hsu, L. and Yu, I.A.: Cooling atoms below 100 k. *Chinese Journal Of Physics*, vol. 38, no. 2-11, pp. 395–399, April 2000.
- [4] Wineland, D.J. and Itano, W.M.: Laser cooling. *Physics Today*, vol. 40, no. 6, pp. 34–40, June 1987.
- [5] Steck, D.A.: Rubidium 87 d line data. Tech. Rep., University of Oregon, available online at <http://steck.us/alkalidata>, .
- [6] Preston, D.W.: Doppler free-saturated absorption spectroscopy: Laser spectroscopy. *Am. J. Phys*, vol. 64, no. 11, pp. 1432–1436, November 1996.
- [7] Morrissey, M.J.: *Manipulation Tools for Laser-Cooled Rubidium Atoms : Ultrathin Optical Fibres and Magnetic Diffraction Gratings*. Ph.D. thesis, Cork Institute of Technology, Cork, July 2009.
- [8] Chormaic, S., Yarovitskiy, A., Shoett, B., Deasy, K. and Morrissey, M.: Precision control of magneto-optical cooled rubidium atoms. Dept. of Applied Physics and Instrumentation. Cork Institute of Technology. Cork. Ireland and Tyndall National Institute. Prospect Row. Cork. Ireland.
- [9] Metcalf, H.J. and van der Straten, P.: Laser cooling and trapping of neutral atoms. *Physics Report*, vol. 244, pp. 203–286, January 1994.
- [10] Hansch, T.W. and Schawlow, A.L.: Cooling of gases by laser radiation. *Optics Communications*, vol. 13, no. 1, pp. 68–69, January 1975.
- [11] Wieman, C., Flowers, G. and Gilbert, S.: Inexpensive laser cooling and trapping experiment for undergraduate laboratories. *American Journal of Physics*, vol. 63, no. 4, pp. 317–330, 1995.
- [12] Adams, C.S. and Riis, E.: Laser cooling and manipulation of neutral particles. Tech. Rep., Cambridge University.
- [13] Knight, P.L. and Miller, A.: *The Physics of Laser-atom Interactions*. Cambridge University Press, Edinburgh building, Cambridge CB2 2RU, UK, 1997.

- [14] Claude, N. and Willium, D.P.: New mechanism for laser cooling. *Physics Today*, vol. 43, no. 10, pp. 34–40, October 1990.
- [15] Liwag, J.W.F., Sicam, V.A. and Karremans, K.: Measurement of the temperature of rubidium atoms in a magneto-optical trap. *Science Diliman*, vol. 15, no. 1, pp. 22–26, January 2003.
- [16] Lett, P.D., Phillips, P.D., Rolston, S.L., Tanner, C.E., Watts, R.N. and Westbrook, C.L.: Optical molasses. *Opt. Sec. Am.*, vol. 6, no. 11, pp. 2084–2104, July 1989.
- [17] Rigby, C.I.: *Development of a Laser Cooling and Magneto-Optical Trapping of Rubidium 87 Atoms*. Master's thesis, Stellenbosch University, December 2010.
- [18] Horbanki, M. and Kriger, J.: *Magneto Optic Trap*. www.jkrieger.de/download/mot_report.pdf, June 2005.
- [19] Lewandowski, H.J., Harber, D.M., Whitaker, D.L. and Cornell, E.A.: Simplified system for creating a bose-einstein condensate. *Low Temperature Physics*, vol. 132, no. 516, pp. 309–367, September 2003.
- [20] Saturated absorption spectroscopy. Tech. Rep., University of Florida-Department of Physics, available online at www.physik.rwth-aachen.de/.../Saettigungsspektroskopie.pdf, March 2008. Advance Physics Laboratory.
- [21] Lett, P.D., Watts, R.N., Westbrook, C.L., Phillips, W.D., Cloud, P.L. and Metcalf, H.J.: Observation of atoms cooled below the doppler limit. *Physics Review Letters*, vol. 16, no. 2, pp. 169–173, July 1988.
- [22] Silva, R.R., Magalhaes, K.M.F., Henn, E.A.L., Marcassa, L.G. and Bagnato, V.: Temperature determination for magneto optical trapped atoms using a single parameter transient absorption. *Optics Communications*, vol. 265, no. 2, pp. 526–531, March 2006.
- [23] Monroe, C., Swann, W., Robinson, H. and Wiemann, C.: Very cold trapped atoms is a vapor cell. *Physics Review Letters*, vol. 65, no. 13, pp. 1571–1574, September 1990.
- [24] Haw, M., Evetts, N., Gunton, W., Dongen, J.V., Booth, I.L. and Madison, K.W.: Magneto-optical trap loading rate dependence on trap depth and vapor density. *Opt. Soc. Am. B*, vol. 29, no. 3, pp. 475–483, March 2012.
- [25] Lindquist, K., Stephens, M. and Wieman, C.: Experimental and theoretical study of the vapor-cell zeeman optical trap. *Physics Review A*, vol. 46, no. 7, pp. 4082–4091, October 1992.
- [26] Botha, G.N.: *Development of an external cavity diode laser for application to spectroscopy and laser cooling and trapping of rubidium*. Master's thesis, Stellenbosch University, December 2008.
- [27] Griffin, P.F., Weatherill, K.J. and Adams, C.S.: Fast switching of alkali atom dispensers using laser-induced heating. *Review of Science Instruments*, vol. 76, no. 9, p. 093102, September 2005.
- [28] Rapol, U.D., Wasan, A. and Natarajan, V.: Loading of a rb magneto-optic trap from a getter source. *PHYSICAL REVIEW A*, vol. 64, no. 2, p. 023402, June 2001.
- [29] Stubbs, P.L. and Novikova, I.: Laser locking with doppler-free saturated absorption spectroscopy, May 2010. W and M Quantum Optics Group.

- [30] <http://ece-www.colorado.edu/~ece5606/Lectures/Lasercooling-2004-lecture.pdf>.
- [31] MacAdam, K.B., Steinbach, A. and Wieman, C.: A narrow-band tunable diode laser system with grating feedback and saturated absorption spectrometer for cs and rb. *Am. J. Phys*, vol. 60, no. 12, pp. 1098–1111, December 1992.
- [32] Hecht, E.: *Optics*. Addison Wesley, 2002.
- [33] Eisberg, R. and Resnick, R.: *Quantum physics of atoms, molecules, solids, nuclei, and particles*. 2nd edn. John Wiley and Sons, 1985.
- [34] Steck, D.A.: Rubidium 85 d line data. Tech. Rep., University of Oregon, available online at <http://steck.us/alkalidata>, .